VIDYA REPORT NO. 181
April 11, 1965

AN EVALUATION OF FREE-FLIGHT TEST DATA FOR AERODYNAMIC HEATING FROM LAMINAR, TURBULENT, AND TRANSITIONAL BOUNDARY LAYERS

PART II—THE X-17 REENTRY BODY

by
John D. Murphy
Morris W. Rubesin

prepared for
NATIONAL AERONAUTICS AND SPACE ADMINISTRATION

Contract No. NAS7-216
Vidya Project No. 9058

RESEARCH DEVELOPMENT

A DIVISION OF Itek CORPORATION

BLANK PAGE

VIDYA

The word Vidya, taken from the Vedanta philosophy of the Hindus, means knowledge. The symbol used to denote the Vidya organization is the letter "V" from Sanskrit, the ancient language of India.

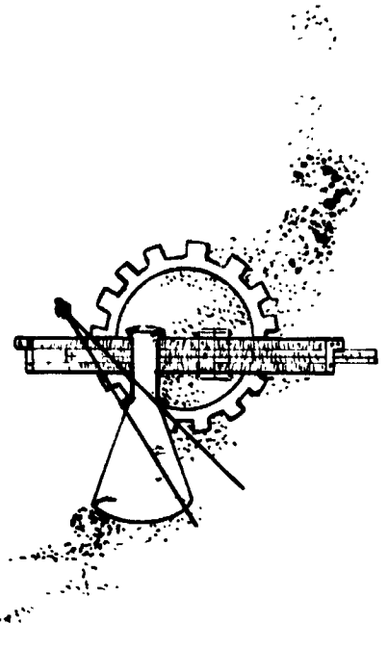

APPLIED MECHANICS
THERMODYNAMICS
NUMERICAL ANALYSIS
PHOTO-OPTICS
IMAGE ANALYSIS
PHYSICS

VIDYA COPY NO. 24

VIDYA REPORT NO. 181

April 11, 1965

AN EVALUATION OF FREE-FLIGHT TEST DATA FOR AERODYNAMIC HEATING FROM LAMINAR, TURBULENT, AND TRANSITIONAL BOUNDARY LAYERS

PART II - THE X-17 REENTRY BODY

by
John D. Murphy
Morris W. Rubesin

prepared for

NATIONAL AERONAUTICS AND SPACE ADMINISTRATION

Contract No. NAS7-216

Vidya Project No. 9058

VIDYA

A DIVISION OF Itek CORPORATION

1450 PAGE MILL ROAD • PALO ALTO, CALIFORNIA

TEL: DAVENPORT 1-2455 TWX: 415 492-9270

SUMMARY

20084

This report describes and applies several theoretical methods for predicting the aerodynamic heating of blunt reentry bodies. The results of these various prediction methods are compared with the experimental heat rates inferred from flight-test data. The data used in this report were obtained from two flights of the Air Force X-17 Reentry Test Vehicle. The results of the present study taken together with the Mark 2 results previously reported constitute the completion of the study on reentry heat transfer funded by NASA under Contract NAS7-216.

The methods employed in the smoothing and reduction of the measured temperature-time data are described in detail.

Aeetha

TABLE OF CONTENTS

LIST OF FIGURES

LIST OF SYMBOLS

A	area, ft^2
C_f	skin-friction coefficient, dimensionless
C_p	specific heat at constant pressure, Btu/lb-^oR
g	acceleration of gravity, 32.2 ft/sec^2
H	total enthalpy, $h + (u^2/2Jg)$, Btu/lb
h	enthalpy, $\int_o^T C_p \, dT$, Btu/lb
h_D	enthalpy of dissociation, Btu/lb
J	mechanical equivalent of heat, 778 ft-lb/Btu
k	thermal conductivity, Btu/ft^2-sec(^oR/ft)
Le	Lewis number, dimensionless
M	Mach number, dimensionless
P	pressure or probability, lb/ft^2
Pr	Prandtl number, dimensionless
q	instantaneous heating flux, Btu/ft^2-sec
R_B	body radius measured from axis of symmetry, ft
Re	Reynolds number, dimensionless
R_N	radius of body curvature at stagnation point, ft
r	local body radius measured from axis of symmetry, ft
s	distance from stagnation point, ft
T	temperature, ^oR
u	velocity, ft/sec
V	volume, ft^3
x	axial distance from stagnation point, ft
Z	molecular weight ratio and compressibility factor, dimensionless
β	pressure gradient parameter (see Appendix C), $(sec)^{-1}$ or dimensionless, or as defined in Equation (3)

Γ	energy thickness, ft
γ	isentropic exponent, dimensionless
ρ	density, lb/ft^3
μ	viscosity, lb/ft-sec
θ	time or momentum thickness, sec or ft

Subscripts

B	refers to base of body
e	evaluated at boundary-layer-edge conditions
r	evaluated at recovery enthalpy
st	evaluated at stagnation conditions
w	evaluated at wall conditions
lam	refers to laminar boundary layer
surf	refers to surface
turb	refers to turbulent boundary layer

Superscripts

*	evaluated at reference enthalpy
-	average value
θ	based on momentum thickness
σ	based on extent of transition region
$\overline{\theta}$	based on momentum thickness at midpoint of transition region

AN EVALUATION OF FREE-FLIGHT TEST DATA FOR AERODYNAMIC HEATING FROM LAMINAR, TURBULENT, AND TRANSITIONAL BOUNDARY LAYERS (U)

PART II - THE X-17 REENTRY BODY (U)

1. INTRODUCTION

1.1 General

This report, together with Reference 1, constitutes the completion of work funded by the NASA under Contract NAS7-216 titled, "Evaluation of Free Flight Test Data for Aerodynamic Heating from Laminar, Turbulent, and Transitional Boundary Layers."

The purposes of this study were:

(1) To assess the adequacy of data obtained from flight test vehicles for the verification of theoretical predictions.

(2) To establish confidence in existing laminar boundary-layer heat-transfer prediction methods.

(3) To determine which, if any, of the available techniques for the prediction of heat transfer from turbulent boundary layers is adequate.

(4) To develop an empirical procedure for the estimation of heat transfer from transitional boundary layers.

In Reference 1, two flights of the Air Force Mark 2 reentry vehicle were considered. In this report, two flights of the Lockheed designed Air Force X-17 reentry test vehicle are considered. The results of both investigations are compared in this report to ascertain overall behavioral patterns consistent with each test.

As was noted in Reference 1, the present authors have several advantages over the original investigators. Principal among these advantages was the passage of time and the concomitant advance of reentry technology since these data were originally considered. In the last 8 years, significant strides have been made in the prediction of heating from laminar boundary layers, the prediction of the transport properties of air at high temperatures, and the analytical determination of inviscid flow fields. The present study embodies most of these advances in an effort to fulfill the purposes noted above.

It was established in Reference 1 that the existing stagnation point and laminar boundary-layer heating theories were adequate to predict aerodynamic heating to reentry vehicles with entry velocities of the order of 14,000 ft/sec. The principal purpose of this phase of investigation

(i.e., the X-17 vehicles) was to establish the accuracy of turbulent boundary-layer heating predictions. It was believed that the character of the trajectory, powered reentry (M_∞ = 12 at 40,000 feet) would insure a fully developed turbulent boundary layer over substantial portions of the body. This belief was reinforced by References 2 and 3 which compared theoretical and measured heating-rate histories at several points on the R-2 and R-9 vehicles. The present investigation, which relies on a dimensionless data presentation to establish boundary-layer transition, indicates, however, that, although boundary-layer transition occurs over substantial portions of the vehicle, a fully developed turbulent boundary layer did not occur in the X-17 reentry bodies.

1.2 Organization of Report

The order of presentation of this report follows, in general, the chronological order of the work accomplished during this study.

In Section 2, the reentry vehicle configuration, instrumentation, and trajectories are described. In Section 3, the method used to evaluate the inviscid flow field is discussed, and the prediction methods for heat transfer from laminar, transitional, and turbulent boundary layers are described. Section 4 compares the experimental results with the predictions discussed in Section 3. Finally, in Section 5, the results of this phase of the study are summarized and general conclusions and recommendations are presented.

2. DESCRIPTION OF VEHICLES AND TRAJECTORIES

2.1 General

The X-17 entry vehicles were experimental reentry test vehicles designed and built by Lockheed Missile Systems Division under contract to the United States Air Force. The purpose of the Lockheed study was to obtain data to aid in the design and development of reentry bodies for long range ballistic missiles.

The vehicle was powered by a three-stage solid-propellant rocket. The first stage of this configuration was used to lift the vehicle from the launch site to a nominal altitude of 400,000 feet. Subsequent to first-stage burnout, the vehicles followed an essentially elliptic trajectory to atmospheric entry. The vehicle was permitted to coast down to an altitude of 90,000 to 70,000 feet at which point the second stage was

fired. The second-stage motor accelerated the vehicle from a speed of about 5000 feet per second to about 9500 feet per second. After second-stage separation, the third stage was fired, bringing the speed up to about 13,000 feet per second at an altitude of 40,000 feet. The trajectory parameters used in this study are presented in Figures 1 and 2.

2.2 R-2 and R-9 Reentry Bodies

The X-17 R-2 and R-9 reentry bodies were 9-inch-diameter copper hemispheres with a 3-1/2-inch-long cylindrical afterbody. The wall thickness was a constant 0.625 inch except at the aft end of the cylinder where there is a step to accommodate the fastening of a telemetry can. Figure 3 shows the R-2 and R-9 heat-sink configurations together with the instrumentation locations. Each of these vehicles carried 23 chromel-alumel thermocouples and 3 Ultradyne pressure gages. Thermocouple data were commutated and transmitted on a single channel of telemetry. The sampling rate for each thermocouple was about 10 samples per second.

Thermocouples of the R-2 and R-9 reentry bodies were installed at the locations noted in Figure 1. The installation technique, as described in Reference 2, was, "The thermocouple wires were encased in a copper sheath which was filled with aluminum oxide to insulate the wires. The outside diameter of the sheath was nominally 0.040 inch. One end of the sheath was dressed down, exposing the thermocouple wires. This end of the sheath was inserted into a hole drilled in a small copper plug. At the bottom of the hole, there was a small amount of high-melting-point silver solder. The plug was then heated until the silver solder melted and formed an electrical contact between the exposed ends of the thermocouple wire.

"The installation was completed by machining the plug in which the thermocouple was mounted and inserting it to a predetermined depth into a hole drilled into the nose cone. The plug was machined oversize and cooled in liquid nitrogen before insertion into the nose. The surface of the nose cone was machine finished and polished."

2.2.1 Surface finish

The R-2 vehicle surface finish was polished copper with a measured RMS roughness of the order of 2 microinches. This finish was obtained by polishing with a 1/4-micron diamond compound.

The R-9 vehicle surface finish was 0.006 nickel plate over Cuprovac E copper with the nickel plate polished to a nominal 1 microinch RMS roughness. A roughness patch of 30 microinch RMS roughness was installed over a secondary thermocouple run (thermocouples N through S).

3. PREDICTION METHODS

3.1 Inviscid Flow Fields

In general, the prediction methods employed in this study are identical with those of Reference 1, the single exception being the prediction of the inviscid flow field. Since the configurations considered in the present study are both hemispherically capped cylinders, the problem of obtaining the flow field parameters is ideally suited to attack by indirect flow field computational methods.

The technique employed in this study was the equilibrium real-gas indirect solution of Reference 5. This solution uses the Fuller method for the subsonic flow regime coupled to a method of characteristics solution in the supersonic flow regime. The equilibrium real-gas properties of Hilsenrath and Beckett are used.

Figure 4 compares the computed pressure distribution for a hemisphere-cylinder at M_∞ = 4, 8, and 12 with the matched Newtonian-Prandtl-Meyer distribution and with unpublished wind tunnel data at M_∞ = 4 and 8.08. As may be seen, it is difficult to distinguish the relative accuracy of the results in this presentation. Figure 5 presents the stagnation-point velocity gradient parameter as a function of shock density ratio. As can be noted, this form of presentation tends to amplify the disparities between the various theories. It can be seen that the two computer solutions, that is, References 1 and 5, are in excellent agreement while the Newtonian method is uniformly low. The authors have employed in this study the method of Reference 5, which has a strong theoretical base, since existing published results of measured stagnation-point velocity gradient are not sufficiently precise to permit ±10 percent discrimination.

3.2 Stagnation-Point Heating

Two theories for predicting convective heating to an axisymmetric stagnation point were considered in this study. These are the theories of Fay and Riddell, Reference 7, and of Hoshizaki, Reference 8.

The stagnation-point heating relation of Reference 7

$$q_{st} = \frac{0.76}{Pr^{0.60}} \left(\frac{\rho_w \mu_w}{\rho_{st} \mu_{st}}\right)^{0.1} \sqrt{\rho_{st} \mu_{st} \left.\frac{du_e}{ds}\right|_{st}} \left[1 + (Le^{0.52} - 1) \frac{h_D}{H_{st}}\right] (H_{st} - h_w) \qquad (1)$$

is a correlation equation derived from numerical integration of the boundary-layer equations under the assumption of chemical equilibrium.[1] The analysis leading to this equation was based on a solution of the laminar boundary-layer equations in the vicinity of the stagnation point under the assumption that (1) the viscosity is given by the Sutherland law, (2) the Prandtl and Lewis numbers are constant through the boundary layer, and (3) thermal diffusion is small. The first two of these assumptions have been examined by Anderson, Reference 9, who essentially duplicated the solution of Reference 7 using the total transport properties of Hansen, Reference 10, and permitted the variation of the Prandtl and Lewis numbers across the boundary layer. He found that Equation (1) correlated his numerical results within $\pm$15 percent if the partial transport properties of Hansen[2] were used and the Prandtl and Lewis numbers were evaluated at the average of their extreme values across the boundary layer. For correlation purposes, the partial properties were employed. In the present analysis it was assumed, therefore, that any self-consistent set of partial transport properties can be substituted in Equation (1) without modification of the form of the equation.

In Reference 8, Hoshizaki also proposes an expression for axisymmetric stagnation-point heat transfer. The analysis leading to this expression was essentially the same as for Reference 9, but extended to much higher velocities. The numerical solutions of the laminar boundary-layer equations of Hoshizaki are correlated to within $\pm$6 percent by the equation

---

[1]Frozen chemical reactions in the boundary layer but with equilibrium at the surface cause the Lewis number exponent in Equation (1) to change to 0.63.

[2]The partial specific heat is given as $C_p' = \sum_i x_i (C_i + R)$ and the partial thermal conductivity is that due to molecular collisions, see Reference 10.

$$\frac{q_{st}}{\sqrt{\rho_w \mu_w \beta_{st}}} = 1340 \left(\frac{u_\infty}{10^4}\right)^{1.69} \left(1 - \frac{h_w}{H_{st}}\right) \qquad (2)$$

over the velocity range $6000 \leq u_\infty \leq 45{,}000$ ft/sec and the range of stagnation pressures $10^{-3} \leq P_{st} \leq 10^{+2}$ atmospheres. Comparison of Equations (1) and (2) using the transport properties of Reference 10 show no significant differences up to flight velocities of 35,000 ft/sec.

In this study, the stagnation-point heating was predicted using Equation (1) and the transport properties of Reference 11. This procedure has been found to be adequate in Reference 12 for entry velocities up to 23,000 ft/sec. For these two methods, that is, Fay and Riddell and Hoshizaki, differences in peak heating rate of the order of 10 percent occur. It should be kept in mind that the differences are due solely to the use of different transport properties.

3.3 Laminar Boundary-Layer Heating Away from the Stagnation Point

Three laminar boundary-layer heat-transfer theories for regimes away from the stagnation point with air in chemical equilibrium were considered in the present study. These were the methods of Lees, Reference 13, Kemp, Rose, and Detra, Reference 14, and the method of Rubesin, Reference 15.

It is interesting to note that all three of these theories can be cast into a single form with the coefficients and exponents separately specified for each theory. Table I presents this form together with the appropriate values of the parameters. The equations presented in Table I have been normalized with respect to their own limit form as $s \rightarrow 0$. In application, however, the theory of Fay and Riddell has been used to establish the stagnation-point heating level. That is to say, only the variation in the shapes of the heating distribution curves are considered characteristic of the different theories, the level being established for all theories by the stagnation-point theory of Fay and Riddell.

In describing the laminar boundary-layer heat-transfer theories of Lees and of Kemp, Rose, and Detra, it is convenient to consider first the earlier work of Cohen and Reshotko, Reference 16. In this reference, the authors report the solution of the two-dimensional compressible boundary-layer equations including the effect of constant wall cooling ratio and constant pressure gradient. Numerical solutions were obtained for a Prandtl number of unity and a Chapman-Rubesin constant evaluated from the

Sutherland viscosity law. A modification of the Stewartson transformation was applied to reduce the equations to the case of two-dimensional incompressible flow. Tabulated values of the solutions of these incompressible equations are presented in Reference 16 for various values of the pressure gradient and heat-transfer parameters.

3.3.1 Method I (Lees, Ref. 13)

Lees noted that, for Prandtl and Lewis numbers equal to unity, $\rho\mu$ = constant, and a highly cooled wall, the boundary-layer equations for compressible flow around a blunt axisymmetric body can be reduced to the incompressible equations of Reference 16 by the introduction of the transformation

$$\tilde{s} = \int_0^s \rho_e u_e \mu_e r^2 \, ds$$

$$\eta = \frac{\rho_e u_e}{\sqrt{2\tilde{s}}} \int_0^y r \frac{\rho}{\rho_e} \, dy$$

He further makes the physical argument that, since the flow close to the wall is characterized by a much higher density than that at the boundary-layer edge, the effect of the externally imposed pressure gradient on the velocity distribution near the wall is significantly reduced. Under this argument, he applies the stagnation-point value of the pressure gradient parameter, $(2\tilde{s}/u)(du/ds)$, over the entire body. The appropriateness of this approximation can be seen directly in Figure 9 of Reference 16. The laminar boundary-layer heat-transfer correlation of Lees is then obtained by applying the inverse of the transformation noted above to the numerical results of Reference 16.

3.3.2 Method II (Kemp, Rose, and Detra, Ref. 14)

The laminar boundary-layer heating correlation of Kemp, Rose, and Detra results from an extension of the work of Cohen and Reshotko to the case of nonunity Prandtl number. This represents an extension of the stagnation-point results of Fay and Riddell to flow around the body. In Reference 14, numerical solutions are generated for constant values of

$\rho_e\mu_e/\rho_w\mu_w$ different from unity and for Prandtl number of 0.71. The transformation of Lees noted above is applied to obtain two-dimensional incompressible equations, and the effect of viscous dissipation is included. The results are correlated under the assumption of local similarity, that is, the local heat transfer is related primarily to the local pressure gradient and essentially independent of pressure gradient history.

3.3.3 Method III (Rubesin, Ref. 15)

Since the method of Rubesin is the only one of the three methods considered which has not been treated in the open literature, a somewhat more detailed treatment of this method is given here.

The integral energy equation is derived by integrating the total energy equation in divergence form with respect to y, to yield

$$rq_w + r\rho_w v_w (H_e - H_w) = \frac{d}{dx}\left[r\rho_e u_e (H_e - H_w)\Gamma\right]$$

where the energy thickness Γ is defined as

$$\Gamma = \int_0^\infty \frac{\rho u}{\rho_e u_e}\left(\frac{H_e - H}{H_e - H_w}\right) dy$$

If we now establish the flat-plate energy equation for Stanton number in terms of a Reynolds number based on Γ, and substitute this relation in the above equation, the resulting differential equation is integrable in closed form for the case of $v_w = 0$ and $dH_w/dx = 0$. The assumption implicit in this analysis is that the local heat transfer is a function of the local energy thickness only since this parameter is the characteristic dimension of the boundary layer at the point. The resulting expression is shown in Table I. The effects of compressibility are accounted for by evaluating the boundary-layer properties at the reference enthalpy and local pressure. In Reference 16, the reference enthalpy is given for a laminar boundary layer as

$$h^* = 0.23\ h_e + 0.19\ h_r + 0.58\ h_w$$

and in Reference 17 as

$$h^* = 0.28\, h_e + 0.22\, h_r + 0.5\, h_w$$

The latter form was used in this analysis. The reason for using the Eckert form of the reference enthalpy was for the convenience of being able to use a single reference enthalpy for the laminar, turbulent, and transitional boundary layers. The most interesting point of this integral equation method is the simplicity of the analysis, in that a closed form solution is obtained, and the excellent agreement noted between the results of this method and those of the more sophisticated numerical solutions of Reference 14.

All three of these methods are derived for the flow of air in chemical equilibrium over a spacewise isothermal surface. In brief, then, one can state that all the laminar boundary-layer heat-transfer theories yield essentially the same results when normalized to their own stagnation-point values.

The methods of Bromberg, Reference 18, and Vaglio-Laurin, Reference 19, were also considered in the early phases of the program. The method of Bromberg contains two free parameters which permit matching to stagnation point and zero pressure gradient heating levels. As a result, this procedure can be forced essentially to reproduce the results previously computed. The correlation equation of Vaglio-Laurin is similar to that of Lees except that a coefficient of 0.47 instead of 0.50 is used and the properties are chosen as

$$\rho_r \mu_r = \left(\rho_e \mu_e\right)^{0.8} \left(\rho_w \mu_w\right)^{0.2}$$

This reference condition is chosen to agree with the results of Fay and Riddell at the stagnation point.

3.4 Transitional Boundary-Layer Heating

Boundary-layer transition has been the subject of analytical and experimental investigations for many years and little success with regard to a universal explanation of the phenomenon has resulted. Reference 20 presents a summary of the results obtained in these studies up to about 1957. Very recently, a revival of interest in boundary-layer transition has been indicated. The motivation behind this resurgence in interest in this phenomenon has been the realization that, for the extremely high

convective heating rates associated with atmospheric entry at super satellite velocities, the absence or presence of a transitional or turbulent boundary layer may well determine the feasibility of a given mission.

In Reference 21, Schubauer and Klebanoff determined experimentally that for incompressible flow over a flat plate, the distribution of an intermittency factor, γ, in the transition region is closely approximated by a Gaussian integral curve. The intermittency factor, γ, is defined as the fraction of the time that a point on the wall is covered by a turbulent boundary layer. In Reference 22, Reynolds, Kays, and Kline made use of this observation in the prediction of heat transfer to a flat plate in low-speed flow in a region of known transition. A modification of their procedure is outlined below.

Following Reference 22, we define

$$\beta(x) = \int_0^x P(s)\, ds \tag{3}$$

where $\beta(x)$ is the probability that transition has occurred before x, and $P(s)\, ds$ is the probability that transition occurs between s and $s + ds$. Since, ultimately the boundary layer is fully turbulent

$$\beta(\infty) = \int_0^\infty P(s)\, ds = 1$$

and the location of the average value of the transition point is

$$\bar{s} = \frac{\int_0^\infty sP(s)\, ds}{\int_0^\infty P(s)\, ds} = \int_0^\infty sP(s)\, ds \tag{4}$$

If we define $q(x,s)$ as the turbulent heat transfer to a point x, the distance from the leading edge, from a boundary layer which has undergone instantaneous transition at a point s, we can sum the contributions of all such instantaneous transitions as the product of the probability that the boundary layer is turbulent and the turbulent boundary-layer heating rate, both evaluated at the point in question. Or, symbolically

$$\text{Intermittent turbulent contribution} = \int_0^x q_{turb}(x,s)P(s)\,ds \qquad (5)$$

Similarly, the laminar contribution can be written as $(1 - \beta)q_{lam}$. The total heating to the point is then

$$q(x) = (1 - \beta)q_{lam} + \int_0^x q_{turb}(x,s)P(s)\,ds$$

or, in dimensionless form

$$St(x)Z_m = (1 - \beta)St_{lam}(x)Z_{lam} + \int_0^x St_{turb}(x,s)Z_{turb}\Gamma(s)\,ds \qquad (6)$$

where

$$Z = \frac{h_e + r\frac{u_e^2}{2} - h_w}{H_e - h_w}$$

From the theory of Rubesin, Reference 15, we can evaluate the ratio of heat transfer from a turbulent boundary layer with instantaneous transition at s to the heat transfer from a boundary layer turbulent from the stagnation point, obtaining

$$\frac{St(x,s)}{St(x,o)} = \frac{1}{1 - \frac{Re_s}{Re_x}\left(1 - \frac{33.9\,\phi}{Re_s^{0.375}}\right)^{0.2}} \qquad (7)$$

where

$$\phi = \left(\frac{\mu'/\mu_e}{\rho'/\rho_e}\right)^{0.375}$$

for the Eckert form of the reference enthalpy. We note that the numerical value of the right-hand side of Equation (7) is greater than 1 due to the fact that the boundary layer is thinner if the finite laminar run is appropriately accounted for. This fact offers a phenomenological

In order to account for this circumferential conduction, a three-dimensional conduction program was generated and was used in the R-9 data reduction. A comparison of the results of this program with the experimental heat rates of Reference 4, indicates that near peak heating the latter results are high by about 30 percent in the region of no roughness patch and low by 10 to 20 percent in the vicinity of the roughness patch. Detailed equations and a description of the input and output of this program are treated in Appendix C.

4.3 Stagnation-Point Heating

Figure 12 compares experimental and predicted stagnation-point heating-rate history for the R-2. The prediction uses the theory of Fay and Riddell, Reference 7, with the transport properties of Peng and Pindroh, Reference 11. Values obtained from both one-dimensional and axisymmetric data-reduction programs are shown. One point of interest in this figure is the seeming anomaly associated with the fact that although the stream-wise temperature gradient is consistently away from the stagnation point, see Figure 9, the one-dimensional data reduction indicates consistently higher heating rates than does the axisymmetric data reduction. This occurs because the one-dimensional data-reduction program assumes the configuration to be a slab whereas the actual configuration is, because of the wall thickness, a pie-shaped element and has less heat capacity per unit surface area than in the slab. Figure 13 presents the one-dimensional and axisymmetric heating rates for the same flight in which the body curvature effects are appropriately accounted for. It can be seen from these figures that for the X-17 vehicle errors of the order of 8 to 10 percent can be introduced by failure to account for body curvature, but that the axial conduction is not very significant at the stagnation point.

As can be seen from Figure 12, the prediction of experimental heating rates by the theory of Fay and Riddell is very good, in both level and time relationships, at times when heating rates are relatively large. The peak heating point is missed, however, because it occurs exactly half way between consecutive input points in the data-reduction program, and only linear interpolation is employed in applying the input boundary conditions.

Figure 14 presents similar results for Flight R-9. In this case, however, the experimental heating rates have been obtained from the three-dimensional data-reduction program. Again, correlation is good between predicted and measured heating-rate histories for times $314 \leq \theta \leq 317.5$.

explanation of the overshoot noted in many experimental studies of transition, for example, Reference 23.

In theory, one can now substitute Equation (7) into Equation (6) and carry out the integration, taking $P(s)$ as the normal probability distribution. In practice, however, an examination of the qualitative variation of the two functions of the integrand (see sketch)

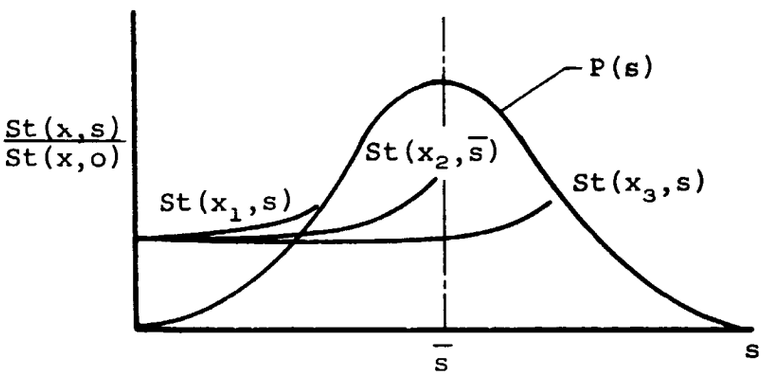

indicates that the Theorem of the Mean can be applied with accuracy. The integral may be evaluated approximately by choosing for the mean value of $St_{turb}(x,s)$ in Equation (6) the following:

$$x = x_3 > \bar{s}, \quad St(x,\bar{s})$$

$$x = x_2 = \bar{s}, \quad St(x,\bar{s})$$

$$x = x_1 < \bar{s}, \quad St(x,s)$$

Thus, the Stanton number at the largest value of $P(s)$ in the interval of integration is chosen as the appropriate mean value. Application of this procedure to the data of Reference 22 indicates essential agreement with the method employed there without introducing the fictitious temperature jump of Reference 22. This temperature jump is required to obtain an equivalence of energy content of the fictitious turbulent boundary layer from the virtual origin to the transition point with the real laminar boundary layer from the actual origin to the transition point. The difference in energy content for a continuity of energy thickness

arises from a difference in Prandtl number dependence for the laminar and turbulent boundary-layer heat-transfer relationships chosen there. If we let both the laminar and turbulent heat transfer depend on $Pr^{-2/3}$, the need for the fictitious temperature jump of Reference 22 is eliminated.

3.5 Turbulent Boundary-Layer Heat Transfer

Three theories for the prediction of turbulent boundary-layer heat transfer were considered in detail. These were the method of Rubesin, Reference 15, the method of Rose, Probstein, and Adams, Reference 24, and the so-called Bromberg I method of Reference 25. In addition, the method of Vaglio-Laurin, Reference 26, was examined. All of the methods considered in detail here are semi-empirical and employ integral solutions. The general form of the correlation equations for these methods is shown in Table II. Specific assumptions and details of the derivations are treated in the following paragraphs.

3.5.1 Method I (Rubesin)

The derivation of the turbulent boundary-layer heat-transfer theory of Rubesin follows the same procedure used in the derivation of the laminar boundary-layer theory discussed in Section 3.4. The integral energy equation alone is considered, and it is assumed that the flat-plate relation between Stanton number and energy thickness Reynolds number is a universal correlation. The local Stanton number on an axisymmetric body is taken to be equal to the Stanton number on a flat plate at a point having equal energy thickness Reynolds number. As a result of this hypothesis, no assumptions need be made with regard to velocity or temperature profiles in the boundary layer. The effects of compressibility are, as in the laminar case, accounted for by the evaluation of boundary-layer properties at the reference enthalpy and the local pressure.

3.5.2 Method II (Rose, Probstein, and Adams)

The method of Rose, Probstein, and Adams uses the integral momentum equation together with the Crocco relation between enthalpy and velocity and the Colburn extension of Reynolds analogy to obtain the relation for turbulent boundary-layer heat transfer. The boundary-layer form factor δ^*/θ is taken as zero, the Blasius skin-friction law with properties evaluated at the edge of boundary layer is employed, and 1/7-power velocity

distribution is assumed. The resulting equation is integrated around the body to yield the equation shown in Table II. Since the Crocco relation, as applied in this method, is used only to relate the momentum thickness to the total boundary-layer thickness and since the boundary-layer properties in the Blasius skin-friction law are evaluated at edge conditions, the method accounts for compressibility in some places and not in others. The arguments supporting these assumptions are given as follows: "These conclusions are based on the observations that (1) the major changes in the fluid properties occur through the laminar sublayer, which transmits the turbulent shear to the wall; (2) the shear is approximately constant through the sublayer; and (3) the boundary-layer growth is practically unaffected by the sublayer, since only a small fraction of the total momentum is included there." Although the first two of these above statements are correct, the fact that the large gradients occur in the sublayer imposes the requirement that the sublayer contributes to the skin friction which in turn controls the rate of boundary-layer growth. Thus, even though the sublayer does not contribute much to the value of the local momentum thickness, θ, it is very significant in establishing its rate of growth. Therefore, the sublayer properties should enter the problem but have been largely eliminated in the details of this method.

3.5.3 Method III (Bromberg I)

The assumptions and procedures employed in this derivation are essentially the same as those of Method II above. Results obtained from integration of the flat-plate momentum equation using a 1/7-power velocity distribution and the Blasius skin-friction law are introduced into the integral energy equation by means of Reynolds analogy. The resulting equation is integrated around the body to yield the turbulent heat-transfer correlation equation.

The method of Vaglio-Laurin is somewhat different in form in that the Stewartson transformation is used and the Karman-Schoenherr skin-friction law is applied. This results in the expression

$$q_{turb} = \frac{\mu_e}{\mu_{st}} \frac{C_f'}{2\ Pr^{2/3}} \rho_e u_e (H_{st} - h_w)$$

where C_f' is defined by the relation

$$\ell n\ C_f' + \ell n \left(\frac{2.62}{P_{st}{}^r} \int_o^s \frac{r\rho_e\mu_e}{\rho_{st}\mu_{st}} u_e\ ds \right) = \frac{0.40}{\sqrt{C_f'/2}}$$

In Reference 26, it is recommended that the substitution $\rho_e\mu_e = (\rho_e\mu_e)_{st}$ be made. The fluid properties at the wall do not enter the analysis. This form of the skin-friction law is particularly inconvenient for engineering applications since the local, both in time and space, skin-friction coefficient must be solved for by successive trials. Since the values of the skin-friction coefficient predicted by the two theories in question, that is Blasius and Karman-Schoenherr, are very nearly equal for the Reynolds numbers considered here $Re = 0(10^7)$. The additional labor involved in computation with Vaglio-Laurin method is not justified.

Results of the three major methods discussed above, that is, Rose, et al., Rubesin, and Bromberg, are compared in Reference 1. It was found that significant differences in heating level are predicted by the various theories. Since flight test experimental data for fully developed turbulent boundary layers are lacking, no conclusions can be drawn as to the relative merit of the several theories.

4. COMPARISON OF EXPERIMENTAL AND PREDICTED RESULTS

4.1 General

In discussing the experimental results, a clear distinction must be made between the results of Flight R-2 and Flight R-9. Although the results of the two flights yield the same qualitative conclusions, the date from Flight R-2 are far superior to those of Flight R-9. The primary cause of the poor data quality of the R-9 data is believed to be noisy telemetry. The argument underlying this assertion is based on a comparison of plots of Stanton number versus energy thickness Reynolds number at constant body station and the same parameters at constant time. These plots for constant body station exhibit a scatter of the order of ± 100 percent while the plots for constant time, in the range $315 \leq \theta \leq 319$ seconds, yield comparisons of quality comparable to the R-2 results. This is attributed by the present authors to a low signal-to-noise ratio at $\theta < 315$ seconds and the onset of noise prior to telmetry failure at $> = 319.5$ seconds. Figure 6 presents a typical plot of the raw commutated telemetry output for thermocouple data. This particular set of data is

for the stagnation point of Flight R-9. It can be seen from this figure that the data scatter is of the order of $\pm 40^{\circ}$ F. The rather high initial temperature is the residual of the effect of exit heating. For a description of the data-smoothing technique, see Appendix A.

Figure 7 presents the streamwise temperature distribution at selected times for the R-2. The large difference in the shape of this distribution for $\theta = 357$ as compared to the earlier times reflects the increased heating for $S/R > 0.5$ due to boundary-layer transition.

Figure 8 presents the smoothed temperature histories for the body position $S/R = 60^{\circ}$ on opposite body meridians of Flight R-9, thermocouples G and R. It can be noted immediately that the heating rate and total heating at thermocouple R is substantially larger than that at thermocouple G. This asymmetric heating pattern gave rise to the need for developing a three-dimensional conduction program for analyzing the data, see Section 4.2.

The comparisons presented in this report are restricted to heat-transfer data alone, since insufficient pressure data of Flights R-2 and R-9 were obtained. The heat-transfer results are presented in dimensionless form, that is, St versus Re_{Γ} for all body locations except the stagnation point. Stagnation-point heat-transfer results are presented as heating-rate histories.

In comparing flight-test heat-transfer data with theoretical predictions in Reference 1, some conceptual difficulty was encountered in presenting Stanton number, a measured quantity, against Re_{θ}, a wholly predicted quantity. In the present report, this difficulty was circumvented, at least in part, by correlating the measured Stanton number against the measured energy thickness Reynolds number.

The procedure used to obtain the measured energy thickness Reynolds number was as follows:

The integral energy equation for no blowing and $dH_w/dx \approx 0$ can be written as

$$\frac{q_w}{\rho_e u_e (H_e - H_w)} = \frac{d\Gamma}{dx} + \frac{\Gamma}{r\rho_e u_e} \frac{d}{dx} (r\rho_e u_e)$$

where

$$\Gamma = \int_0^S \frac{\rho u}{\rho_e u_e} \left(\frac{H_e - H}{H_e - H_w} \right) dy$$

Then,

$$r\rho_e u_e \, St = \frac{1}{Z} \frac{d}{dx} (r\rho_e u_e \Gamma)$$

where

$$Z = \frac{H_{rec} - H_w}{H_e - H_w}$$

Integrating both sides with respect to x and noting that, for $x = 0$, $r = \Gamma = 0$,

$$\frac{1}{r\mu_e} \int_0^x \frac{rq}{H_{rec} - H_w} dx = \frac{\rho_e u_e \Gamma}{Z\mu_e} = \frac{Re_\Gamma}{Z}$$

or

$$\frac{2\pi}{r\mu_e} \int_0^x \frac{rq}{H_{rec} - H_w} = 2\pi \frac{Re_\Gamma}{Z}$$

We note that the integral on the left-hand side is simply the heat-transfer coefficient integrated over the body up to the point in question, that is,

$$Re_\Gamma = \frac{Z}{2\pi r\mu_e} \int_0^x C_H \, dA$$

As a result, the inference of C_H from the thermocouple data, see Section 4.2, provides a direct experimental measure of the energy thickness Reynolds number. Figure 9 presents the results of this procedure for data from X-17 Flight R-2, compared with the theory of Rubesin. The flight conditions for this figure are $M_\infty = 10$ at an altitude of 31,000 feet. The predictions shown in this figure were obtained, using the real-gas inv inviscid flow field of Lomax and Inouye, Reference 5, to obtain boundary-layer-edge conditions. The three predicted lines represent the distribution of Re_Γ for a completely laminar boundary layer, a completely turbulent boundary layer, and a boundary layer with instantaneous transition from laminar to fully developed turbulent flow at $Re_\Gamma = 450$. As is

indicated by the comparison, an essentially transitional boundary layer covers most of the forebody. This conclusions is substantiated by Figure 10 which shows a comparison of measured and predicted streamwise distribution of heat transfer for the same point of time. It can be seen from this figure that the body locations $S > 0$ the heat transfer lies between the laminar and turbulent boundary-layer predictions. Similar results are presented in Figure 11 for the R-9. The most interesting point to be made from this figure is that, while the data identified K-1 are obviously completely laminar, the data identified K-3 which are on the opposite body meridian and contain the roughness patch show strong effects of boundary-layer transition.

4.2 Determination of Experimental Heating Rates

The experimental heating rates discussed in this report have been inferred from telemetered temperature histories measured at various points on the body, see Section 2.2. In order to convert these experimental temperature histories into heating rates, the raw data must be smoothed and then input to the data reduction program. The data-smoothing procedure employed for this study is described in Appendix A.

The data-reduction program employed for X-17 Flight R-2 was the axisymmetric transient temperature program where the Fourier heat-conduction equation is solved numerically as is described in Reference 1. This program employs an explicit finite difference scheme. Temperature-dependent thermophysical properties, such as thermal conductivity, specific heat, etc., are accounted for in the analysis. Surface heating rates are computed from an energy balance which accounts both for conduction normal to and along the body surface. Circumferential conduction is neglected. The detailed equations together with a description of the input and output of this program are treated in Appendix B.

In Reference 4, Tellep and Hoshizaki presented the experimental heat rates for X-17 Flight R-9, obtained from one- and two-dimensional data reduction. It was noted from their presentation that heating rates in the areas covered by the roughness patch were as much as a factor of two larger than those of the circumferentially adjacent thermocouples. It was believed that, due to the relatively small size of the body, that is, 9-inch diameter, and the 5/8-inch-thick wall, failure to account for circumferential conduction could introduce significant errors in the inferred experimental heating rates.

The latter half of the experimental heating pulse seems to lead the prediction by about 1/2 second. This may be due to faulty data smoothing, but is believed to be attributable to biased telemetry of which more will be said in Section 4.4.

4.4 Heat-Transfer Correlations

4.4.1 General

Since the primary objective of this study is to examine the correlation between theoretical predictions and experimental data in the transitional and turbulent flow regimes, it has been found useful to cast the results into dimensionless form. Although this form of presentation seems to have fallen into disrepute in recent years, it does permit the immediate identification of fully turbulent boundary layers, whereas the presentation of heating-rate histories can result in erroneous inferences as to the nature of the flow. A case in point is Reference 3, in which experimental heating-rate histories are compared with the laminar boundary-layer heat-transfer theory of Lees, Reference 13, and the turbulent boundary-layer heat-transfer theory of Denison, Appendix C of Reference 3. In those figures, in Reference 3, where the theoretical and experimental turbulent boundary-layer heating rates are compared the conclusion that the boundary layer is fully turbulent over the latter portion of the heating pulse is obvious. And, in fact, this conclusions was drawn. When, however, during the present study, these results were cast into dimensionless form, St versus Re_T, see Figures 15(a) through 15(h), the inescapable conclusion is that the flow is transitional in nature and never reaches fully developed turbulence as would be indicated by a -0.25 slope of the data. This conflict of conclusions results primarily from the uncertainties in the prediction of turbulent boundary-layer heating. It was found in Reference 1 that differences in predicted heating levels of a factor of 2 can result from the choice of one or another of the available theories, and that the choice of one of the lower turbulent theories when compared to data in a q versus time plot will allow transition data to appear fully turbulent.

4.4.2 R-2 results

The present results for Flight R-2, Figures 15(a) through 15(h), are in substantial agreement with the results presented in Reference 1, in

that within the limitations of data quality, the laminar boundary-layer heating is well correlated by the theory of Fay and Riddell and of Kemp, et al. In the subsonic flow regime, $S/R \leq 40^{o}$, boundary-layer transition is initiated in the range $400 \leq Re_{\Gamma} \leq 600$ and in the supersonic region $S/R \geq 50^{o}$ boundary-layer transition occurs at Re_{Γ} of approximately 800.

Figures 15(a) through 15(h) present Stanton number normalized with ℓ against energy thickness Reynolds number for constant body station. This form is more convenient than constant time presentations since in considering boundary-layer transition the local properties of the boundary layer are well defined. The parameter ℓ is obtained by casting the laminar boundary-layer heating theory of Kemp, et al., into Re_{Γ} form. This procedure yields

$$St = \frac{1}{Pr}\left(\frac{g_{\eta_{w_s}}}{1 - g_{w_s}}\right)^2 \frac{\rho_w \mu_w}{\rho_e \mu_e}\left[1 + (Le^{\alpha} - 1)\frac{h_D}{H_s}\right] Re_{\Gamma}^{-1}$$

or letting

$$\ell = \frac{\rho_w \mu_w}{\rho_e \mu_e}\left[1 + (Le^{\alpha} - 1)\frac{h_D}{H_s}\right]$$

$$\frac{St}{\ell} = \frac{1}{Pr}\left(\frac{g_{\eta_{w_s}}}{1 - g_{w_s}}\right)^2 Re_{\Gamma}^{-1}$$

where $g_{\eta_{w_s}}/1 - g_{w_s}$ is evaluated from Equation (31) of Reference 14.

Figure 15(a) shows the dimensionless heating parameter evaluated for the results obtained from thermocouple B. The scatter in this figure is of the order of ± 15 percent with early time data, $Re_{\Gamma} < 150$, showing rather more scatter. A word of caution is in order here since, due to the manner in which Re_{Γ} was obtained, see Section 4.1, a low data point would tend to shift down and to the left, while a high data point would shift up and to the right. This behavior will tend to amplify the inherent data scatter rather than damp it. This disadvantage, however, is believed by the authors to be outweighed by the facility and directness with which the boundary-layer flow character can be determined.

Figure 15(b) presents similar results for the 20° location for thermocouple C and thermocouple O on the opposite body meridian. These results are again characterized by 15 to 20 percent scatter with similar increased scatter at low values of Re_Γ. Some indication of the onset of boundary-layer transition is apparent at an Re_Γ of 350 to 400.

Figure 15(c) presents the results for the 30° position for thermocouple D and thermocouple P on the opposite body meridian. The bulk of the data indicates ±20 percent scatter except for early time. Boundary-layer transition initiates at $Re_\Gamma = 500$.

Figure 15(d) presents the results for the 40° location for thermocouple E and thermocouple Q on the opposite body meridian. Rather severe scatter or more probably bias in the results is indicated at low Re_Γ. It should be remembered that the lowest value of Re_Γ shown on each plot represents results early in time, and that these early time results are consistently overpredicted. Strong boundary-layer transition is indicated at $Re_\Gamma = 700$ and the boundary layer remains transitional.

Figure 15(e) presents the results for the 50° position for thermocouple F and thermocouple R. These results are similar to those of 15(d) except that the transition value of Re_Γ was increased to about 800.

Figures 15(f) through 15(h) present the results for the 60°, 70°, and 80° locations and indicate essentially the same behavior insofar as transitional values of $Re_\Gamma = 800$. This behavior is consistent with the observed increasing stability of supersonic flow with increasing Mach number. It is interesting to note, however, that while boundary-layer transition occurs for $S/R \leq 40°$ at increasing values of Re_Γ with run length, these values occur at virtually the same point in time while in the supersonic regime the aftmost stations appear to undergo transition first. Thus, the transition point creeps forward until the sonic point is reached at which point the remainder of the boundary layer goes into transitional flow.

4.4.3 R-9 results

As was noted in Section 4.1, the scatter in the inferred experimental heating rates of X-17 Flight R-9 appeared to be substantially greater than that of Flight R-2. It was found on closer examination that this data scatter was introduced by the consideration of early time data, $\theta < 315$ seconds, and data acquired during the onset of reentry blackout just prior

to telemetry failure at θ = 319.5. By presenting only those data in the time range $315 \leq \theta \leq 318.5$ it was found that the results were comparable in quality with the results of Flight R-2. The principle disadvantage to this loss of data is the loss of information on boundary-layer transition since, during the time for which reliable data are available, the boundary layer on the R-9 body was predominantly laminar. Some indication of boundary-layer transition on thermocouple Ray K-3 is apparent from the 30° body station aft to the 70° body station. Thermocouple Ray K-4 also indicates boundary-layer transition at the 50°, 60°, and 70° locations Since the roughness patch is located over thermocouple Ray K-3 it is felt that the roughness is a major contributor to the early transition Re_T of approximately 450. The transition on K-4 is believed to be due to lateral contamination coupled with vehicle roll. This latter cause must be included since Ray K-2 indicated no comparable transition.

Figure 16(a) shows the dimensionless heating parameters evaluated for the 10° body station of Flight R-9. The results indicate a ±15 to 20 percent agreement with laminar boundary-layer theory. These results are in substantial agreement with the R-2 results and with the data of Reference 1.

Figure 16(b) shows the inferred Stanton numbers for the 20° body station for all four thermocouple rays. There is a rather large scatter in these results, up to ±30 percent, but the theoretical curve splits the data fairly well. This is to say, the scatter shown is representative of limitations in instrumentation and not in prediction accuracy.

Figure 16(c) presents essentially the same information for the 30° location, except that some indication of boundary-layer transition occurs at Re_T of about 300.

Figure 16(d) presents the dimensionless heating results for the 40° body location for thermocouples E, M, and P. Again the data show a ±30 percent scatter with the initiation of boundary-layer transition at Re_T of 300 to 350 in the vicinity of the roughness patch, thermocouple P.

Figures 16(e) and 16(f) show the same results for the 50° and 60° body locations. Three thermocouples are treated for each plot. The initiation of boundary-layer transition is indicated at an Re_T of 400 to 500.

Figures 16(g) and 16(h) present the dimensionless heating rates at the 70° and 80° locations for the principle thermocouple ray. There is no roughness patch in this area so that the boundary layer appears to be laminar.

The principle conclusion to be drawn from the data of Flight R-9 is that even a fairly small degree of wall roughness, that is 30 μ-in.-rms, can significantly affect the time and Reynolds number of the onset of boundary-layer transition.

4.4.4 Boundary-layer transition

In Section 3.4, a method was presented for the correlation of heat transfer from a transitional boundary layer. The basic method described there was expressed in terms of a Reynolds number based on a length of run along a flat plate. In Reference 1 and in the present study, it is necessary to account for the effects of pressure gradient and for the fact that the present configurations are axisymmetric. Consistent with the hypothesis of Reference 15, it was assumed that a local boundary-layer thickness should be used as the characteristic dimension in the transitional correlation. In Reference 1, the argument was made that, since the original Gaussian distribution of intermittency was determined as a function of x in Reference 21, and since a unique relation between x and θ exists only for a laminar boundary layer, the predicted laminar values of Re_θ should be used in the correlation. Since, however, the dimensionless heating results in this study were correlated against Re_Γ inferred from measurements, an attempt was made to correlate the transitional heating with this parameter. This procedure was met with a noteworthy lack of success since the one-to-one correspondence between Γ and x was lost in using the transitional Re_Γ. As a result, the procedures followed in Reference 1 were again employed here.

Equation (6) of Section 3.4 can be recast in terms of Re_θ as

$$St = (1 - \beta)St_{lam} + \beta\, St_{turb} \tag{8}$$

where

$$\beta = \frac{1}{2} + \frac{1}{2}\,\mathrm{erf}\,\frac{Re_\theta^{\,2} - \overline{Re_\theta}^{\,2}}{Re_{\theta_\sigma}} \tag{9}$$

The correlation of transitional boundary-layer heating resulting from this technique is shown in Figure 17 for the R-2 vehicle. As may be noted, the results of this procedure are in substantial agreement with the data. No R-9 results are shown since due to telemetry failure most of the R-9 transition data were lost.

The transitional correlation curves were obtained by least square fitting Equations (8) and (9) to the experimental data. This fitting process was carried out, as in Reference 1, by adjusting the two free parameters $Re_{\overline{\theta}}$ and Re_{θ_0}. The values of $Re_{\overline{\theta}}$ and Re_{θ_0} found in Figure 17 are plotted in Figure 18. Again, as in Reference 1, it was found that Re_{θ_0} can be represented as a linear function of $Re_{\overline{\theta}}$ and in fact the same linear function as was employed in Reference 1, that is,

$$Re_{\theta_0} = 0.649\ Re_{\overline{\theta}} + 27$$

Figure 19 presents a comparison of the present results, for the relation between $Re_{\overline{\theta}}$ and h_w/H_{st}, with the results of Reference 1. The results of this study are consistent with those of Reference 1; however, the implication of Figure 19 are somewhat difficult to assess. A conclusion one might draw, as in Reference 1, is that for $h_w/H_s \leq 0.1$, further cooling will result in virtually infinite boundary-layer stability. It should be noted, however, that all four of these vehicles had very well controlled surface finishes. Alternatively, and more rationally, one could conclude that there are more parameters to the problem than are represented in Figure 19, a partial list of which may be found in Reference 20. One conclusion which can be drawn is that for the present data and those of Reference 1, there is no indication of the transition reversal noted in References 27 through 29.

5. CONCLUSIONS AND RECOMMENDATIONS

5.1 Conclusions

The conclusions to be drawn from the present study are, in the main, the same as those drawn in Reference 1, that is

(1) Stagnation-point heating, for entry velocities considered here, are adequately predicted from the theory of Fay and Riddell using the transport properties of Peng and Pindroh.

(2) The distribution of laminar boundary-layer heating is adequately predicted by the theory of Kemp, Rose, and Detra.

(3) The proposed transitional heating correlation has been substantiated experimentally.

In addition to these conclusions, the present study has increased the empirical base of the transitional boundary-layer heating correlation

developed in Reference 1, and, possibly most important, pointed up the danger of assuming that any nonlaminar boundary layer is a turbulent boundary layer. This last conclusion, it is hoped, will focus attention on the fact that transitional boundary layers can exist over extensive regions of a reentry body for significant fractions of the heating pulse.

The question of which of the available theories for turbulent boundary-layer heat transfer is best remains unresolved.

5.2 Recommendations

Taking the last item first, it is most important that some consideration be given to the turbulent boundary-layer problem. Since the present results indicate some of the problems associated with determining the existence of turbulent boundary layers in the reentry environment, it would seem fruitful to consider data obtained from high performance aircraft such as the X-15 and the XB-70. Not only do such vehicles have large characteristic lengths, but they have capability of carrying onboard recorders which yield much "cleaner" data.

The last recommendation to be made is with regard to the transitional boundary-layer heating correlation. While the present study has supported both qualitatively and quantitatively the results of Reference 1, the establishment of this correlation as a design tool will require a substantial amount of empirical verification. In particular, the effects of surface roughness should be considered since, in the present study, telemetry failure on Flight R-9 effectively lost all the transitional and turbulent boundary-layer data expected from that flight.

REFERENCES

1. Murphy, J. D. and Rubesin, M. W.: An Evaluation of Free-Flight Test Data for Aerodynamic Heating from Laminar, Turbulent, and Transitional Boundary Layers. Part I - The AF Mark 2 Reentry Body. Vidya Rep. No. 135, June 1964. CONFIDENTIAL

2. Tellep, D. M. and Hoshizaki, H.: Summary Analysis of the X-17 RTV Program. Lockheed Rep. LMSD 2161, July 2, 1957.

3. Denison, M. R. and Tellep, D. M.: X-17 Reentry Test Vehicle R-2 Final Flight Report. Part II - Analysis of Transition and Aerodynamic Heating on Nose Cone. Lockheed Rep. LMSD 3003.

4. Tellep, D. M. and Hoshizaki, H.: X-17 R-9 Preliminary Flight Report Analysis of Transition and Aerodynamic Heating. Lockheed Rep. MSD 2016, Oct. 1956.

5. Lomax, H. and Inouye, M.: Numerical Analysis of Flow Properties About Blunt Bodies Moving at Supersonic Speeds in an Equilibrium Gas. NASA Rep. NASA TR R-204, July 1964.

6. Munson, A. G.: Constant Density Approximations for the Flow Behind Axisymmetric Shock Waves. NASA TN D-857, May 1961.

7. Fay, J. A. and Riddell, F. R.: Theory of Stagnation Point Heat Transfer in Dissociated Air. Jour. of Aero. Sci., vol. 25, no. 2, Feb. 1958, pp. 73-85 and 121.

8. Hoshizaki, H.: Heat Transfer in Planetary Atmospheres at Super Satellite Speeds. ARS Jour., vol. 32, no. 10, Oct. 1962, pp. 1544-1552.

9. Anderson, A. D.: Stagnation Point Heat Transfer in Equilibrium Dissociated Air with Variable Prandtl and Lewis Numbers. Jour. of Aero. Sci., vol. 28, no. 9, Sept. 1961.

10. Hanson, C. F.: Approximations for the Thermodynamic and Transport Properties of High Temperature Air. NASA TR R-50, 1959.

11. Peng, T. C. and Pindroh, A. L.: An Improved Calculation of Gas Properties at High Temperature Air. Boeing Doc. No. D-2-11722, Feb. 1962.

12. Fleming, W. J., Murphy, J. D., and Hanson, C. W.: Evaluation of Reentry Heat Transfer Data Obtained in Flight Testing the Air Force Mark 2 Reentry Vehicle, Part I. Vidya Rep. No. 56, Dec. 1962. CONFIDENTIAL

13. Lees, L.: Laminar Heat Transfer over Blunt-Nosed Bodies at Hypersonic Flight Speeds. Jet Propulsion, Apr. 1956.

14. Kemp, N. H., Rose, P. H., and Detra, R. W.: Laminar Heat Transfer Around Blunt Bodies in Dissociated Air. Jour. of Aero. Sci., vol. 26, no. 7, July 1959.

15. Burnell, J. A., Goodwin, F. K., Nielsen, J. N., Rubesin, M. W., and Sacks, A. H.: Effects of Supersonic and Hypersonic Aircraft Speeds Upon Aerial Photography. Vidya Rep. No. 28, Oct. 1960.

16. Cohen, C. B. and Reshotko, E.: Similar Solutions for the Compressible Laminar Boundary Layer with Heat Transfer and Pressure Gradient. NACA Rep. 1293, 1956.

17. Eckert, E. R. G.: Survey of Boundary Layer Heat Transfer at High Velocities and High Temperatures. WADC TR 59-624, Apr. 1960.

18. Bromberg, R.: An Approximate Solution of the Boundary Layer Equations for Laminar Flow on a Blunt-Nosed Body of Revolution. The Ramo-Wooldridge Corp., Apr. 1955.

19. Vaglio-Laurin, R.: Laminar Heat Transfer on Three-Dimensional Blunt-Nosed Bodies in Hypersonic Flow. ARS Jour., vol. 24, no. 2, Feb. 1959.

20. Dryden, H. L.: Transition from Laminar to Turbulent Flow, Section A of Turbulent Flows and Heat Transfer, High Speed Aerodynamics and Jet Propulsion. Vol. V, Ed. C. C. Lin, Princeton Univ. Press, 1959.

21. Schubauer, G. B. and Klebanoff, P. S.: Contributions on the Mechanics of Boundary Layer Transition. NACA Rep. 1289, 1956.

22. Reynolds, W. C., Kays, W. M., and Kline, S. J.: Heat Transfer in the Turbulent Incompressible Boundary Layer. IV - Effect of Location of Transition and Prediction of Heat Transfer in a Known Transition Region. NASA M emo 12-4-58W, Dec. 1959.

23. Zakkay, V. and Callahan, C. J.: Laminar, Transitional, and Turbulent Heat Transfer to a Cone-Cylinder-Flare Body at Mach 8.0. Jour. of Aero. Sci., vol. 29, no. 12, Dec. 1962.

24. Rose, P. H., Probstein, R. F., and Adams, M. C.: Turbulent Heat Transfer on Highly Cooled Blunt-Nosed Bodies of Revolution in Dissociated Air. Avco/AMP 17.

25. Phillips, R. L.: A Summary of Several Techniques Used in the Analysis of High Enthalpy Level, High Cooling Ratio, Turbulent Boundary Layers on Blunt Bodies of Revolution. The Ramo-Wooldridge Corp., GMTM 194, Sept. 1957.

26. Vaglio-Laurin, R.: Turbulent Heat Transfer on Blunt Bodies in Two-Dimensional and General Three-Dimensional Hypersonic Flow. WADC TN 58-301, Sept. 1958.

27. Diaconis, M. S., Jack, J. R., Wisniewski, R. J.: Boundary Layer Transition at Mach 3.12 as Affected by Cooling and Nose Blunting. NACA TN 3928, Jan. 1957.

28. Jack, J. R., Wisniewski, R. J., and Diaconis, N. S.: Effects of Extreme Surface Cooling on Boundary Layer Transition. NACA TN 4094, Oct. 1957.

29. Diaconis, N. W., Wisniewski, R. J., and Jack, J. R.: Heat Transfer and Boundary Layer Transition on Two Blunt Bodies at Mach Number 3.12. NACA TN 4099, Oct. 1957.

TABLE I

HEAT-TRANSFER DISTRIBUTIONS FOR FULLY DEVELOPED LAMINAR BOUNDARY LAYERS

$$\frac{\dot{q}}{\dot{q}_{st}} = \frac{1}{\sqrt{2(a+k)}} \frac{\left(1 - \frac{0.1515\,\frac{u_e^2}{2Jg}}{H_{st} - H_w}\right)^b \left(\frac{r}{R_N}\right)^k \frac{\rho_r}{\rho_{st}} \frac{\mu_r}{\mu_{st}} \left(\frac{u_e}{u_\infty}\right)^a F(\beta)}{\left(\frac{R_N}{u_\infty} \left.\frac{du_e}{dS}\right|_{s=o}\right)^{1/2} \left\{ \frac{\rho_{r_{st}} \mu_{r_{st}}}{\rho_{st}\mu_{st}} \int_o^{s/R_N} \left(\frac{r}{R_N}\right)^{2k} \left[1 - \frac{0.1515\,\frac{u_e^2}{2Jg}}{(H_{st} - H_w)}\right]^b \frac{\rho_r \mu_r}{\rho_{st}\mu_{st}} \left(\frac{u_e}{u_\infty}\right)^{2a-1} d\,\frac{s}{R_N} \right\}^{1/2}}$$

Theory	Reference	a	b	r	F(β)
Lees	13	1	0	Boundary layer edge	1
Kemp, Rose, and Detra	14	1	0	wall	$\frac{1 + 0.096\sqrt{\beta}}{1.068}$
Rubesin	15	1	2	Reference enthalpy[1]	1

[1] $h^* = 0.22H_{st} + 0.28h_e + 0.5H_w$

k = 0 two dimensional

k = 1 axisymmetric

TABLE II

HEAT-TRANSFER DISTRIBUTIONS FOR FULLY DEVELOPED TURBULENT BOUNDARY LAYERS

$$\frac{q_T}{H_{st} - H_w} = \frac{A}{Pr_r{}^a} \frac{Z^b \mu_r{}^c \rho_r{}^d u_e{}^e r^{1/4}}{\left(\int_o^s Z^b \mu_r{}^c \rho_r{}^d u_e{}^g r^{5/4} \, dS \right)^{1/5}} \left(1 + B \frac{h_D}{H_{st}} \right)$$

Parameter \ Author (Ref.)	Rose, Probstein, and Ada (24)	Bromberg I [illegible]	Rubesin (15)
A	0.0301	0.0288	0.0296
B	.40	0	0
a	2/3	0	2/3
b	0	0	5/4
c	1/4	1/4	1/4
d	1	1	1
e	5/4	1	1
g	9/4	1	1
Z	1	1	$\frac{h_{rec} - h_w}{H_{st} - H_w}$
Reference condition r	Boundary-layer edge	Boundary-layer edge	Reference enthalpy[1]

[1] $h^* = 0.22 H_{st} + 0.28 h_e + 0.5 H_w$

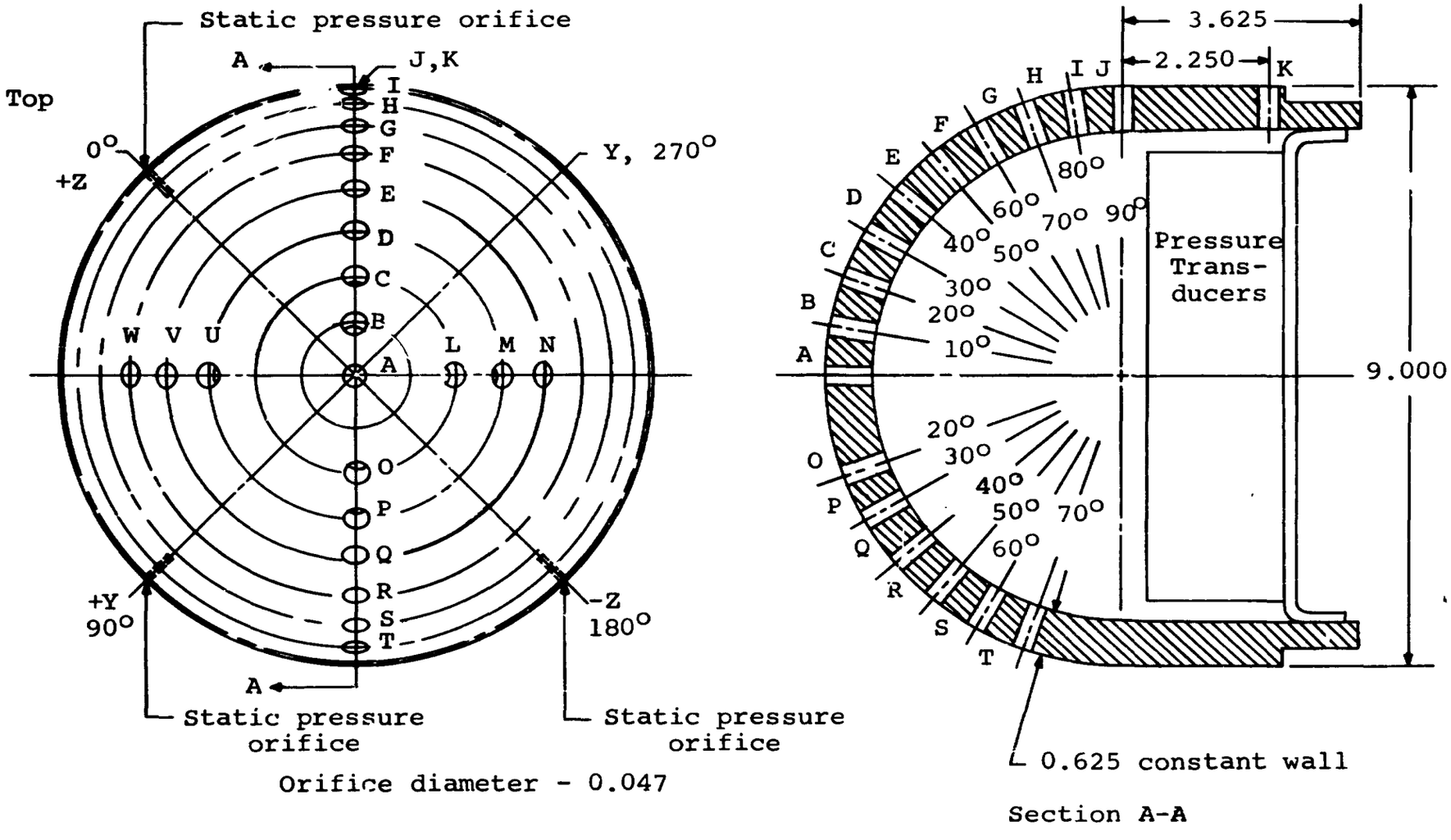

Figure 1.- X-17 R-2 nose, thermocouple and pressure orifice locations.

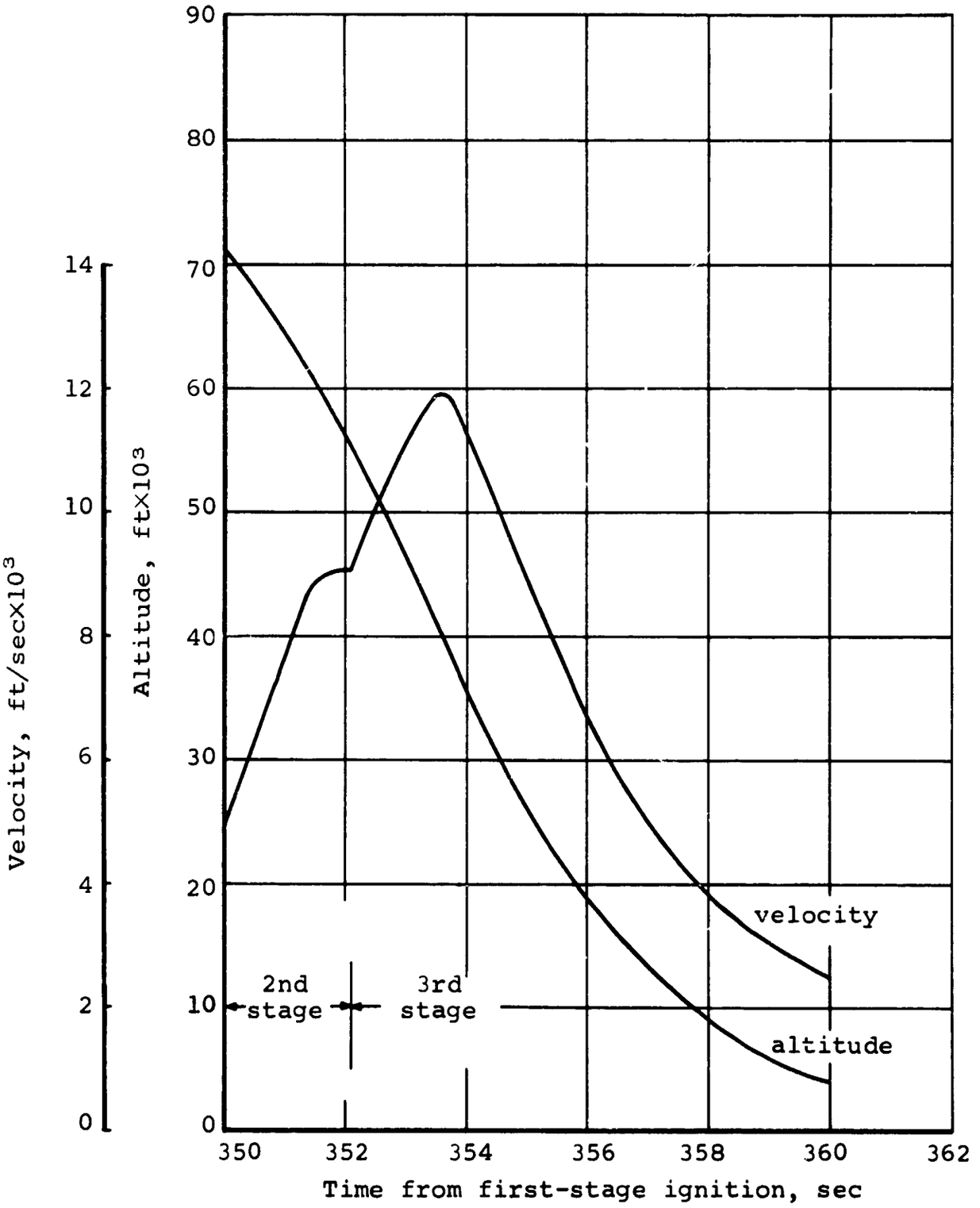

Figure 2.- Trajectory parameters X-17 Flight R-2.

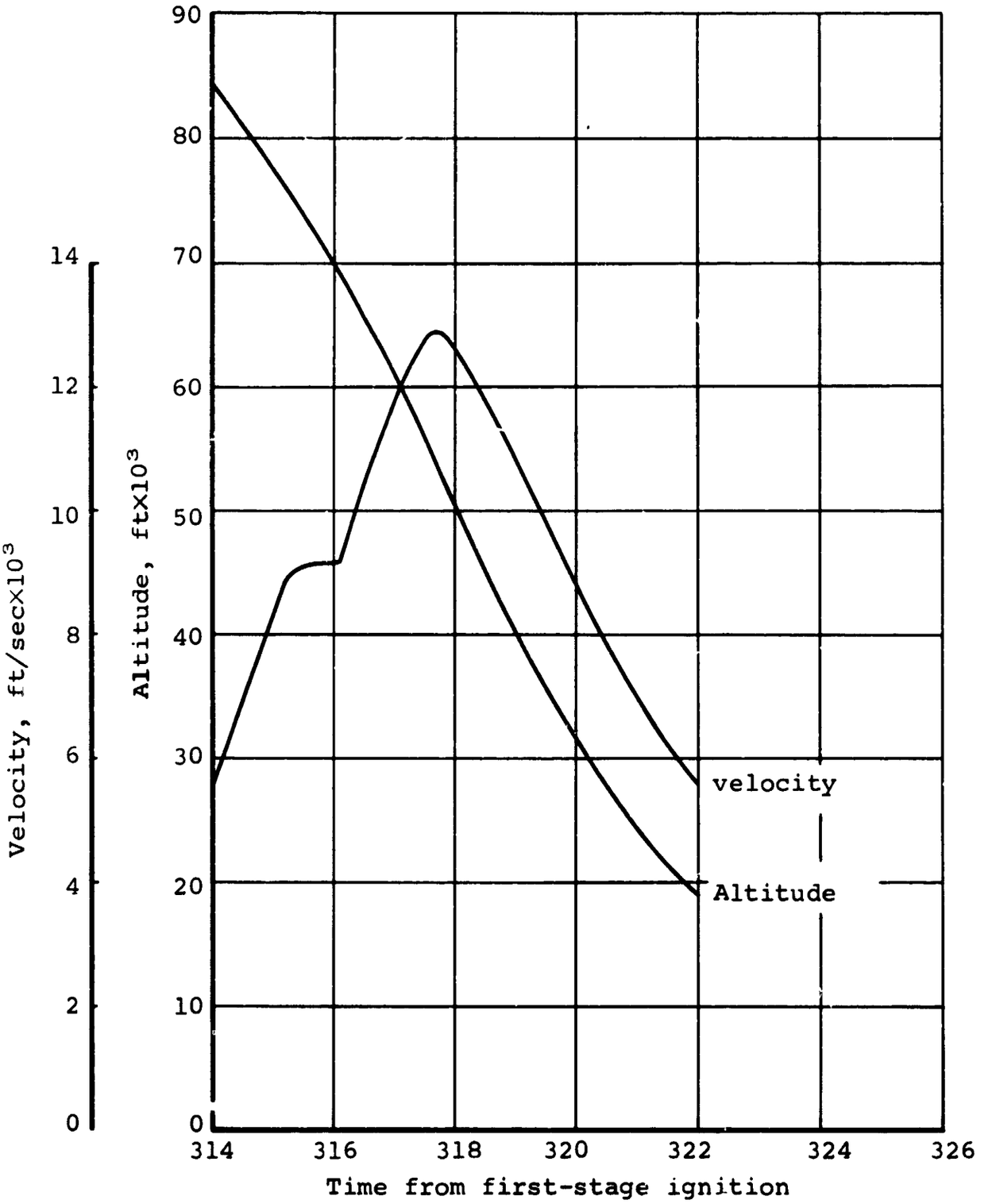

Figure 3.- Trajectory parameters X-17 Flight R-9.

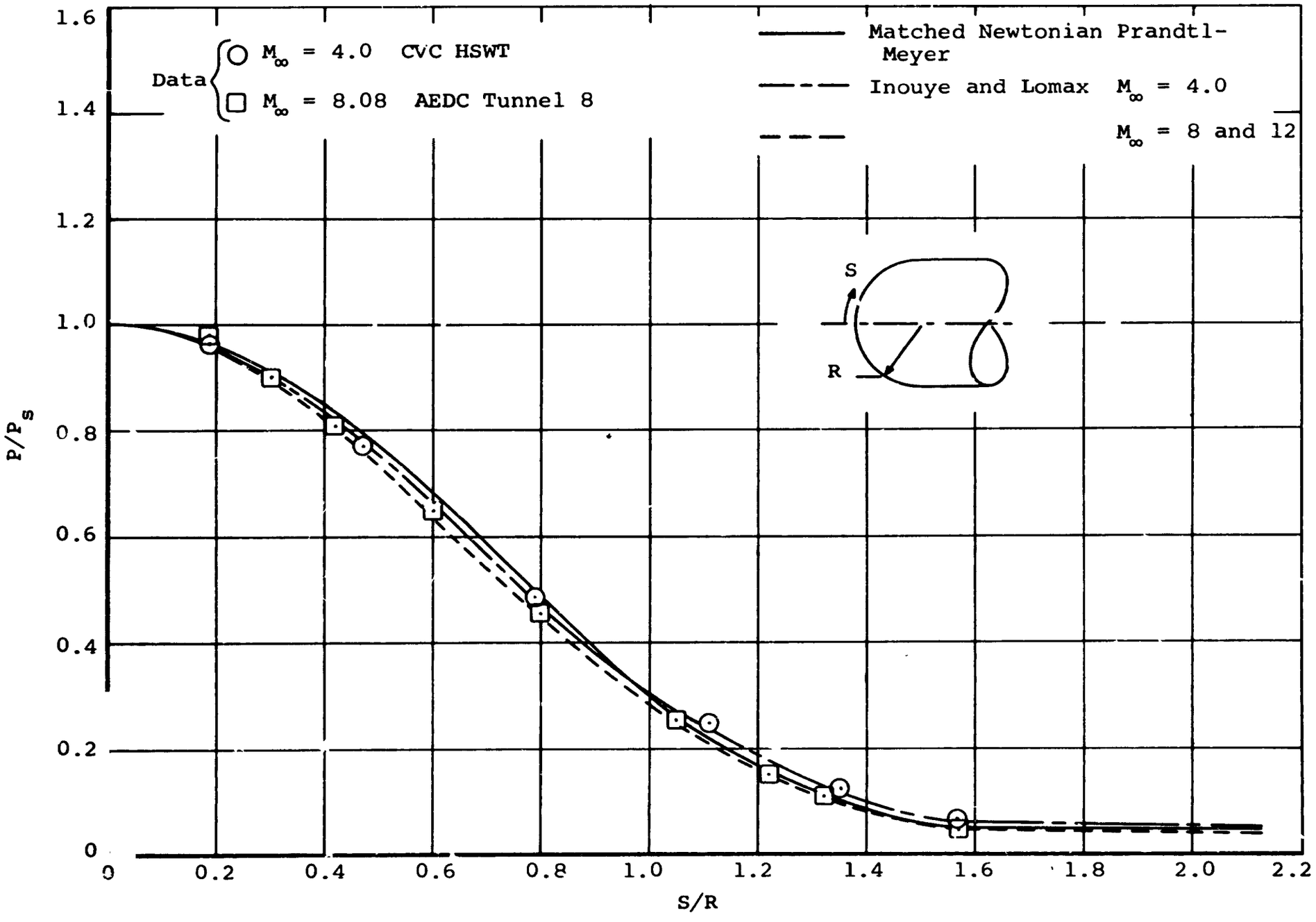

Figure 4.- Pressure distribution on a hemispherically capped cylinder, real gas.

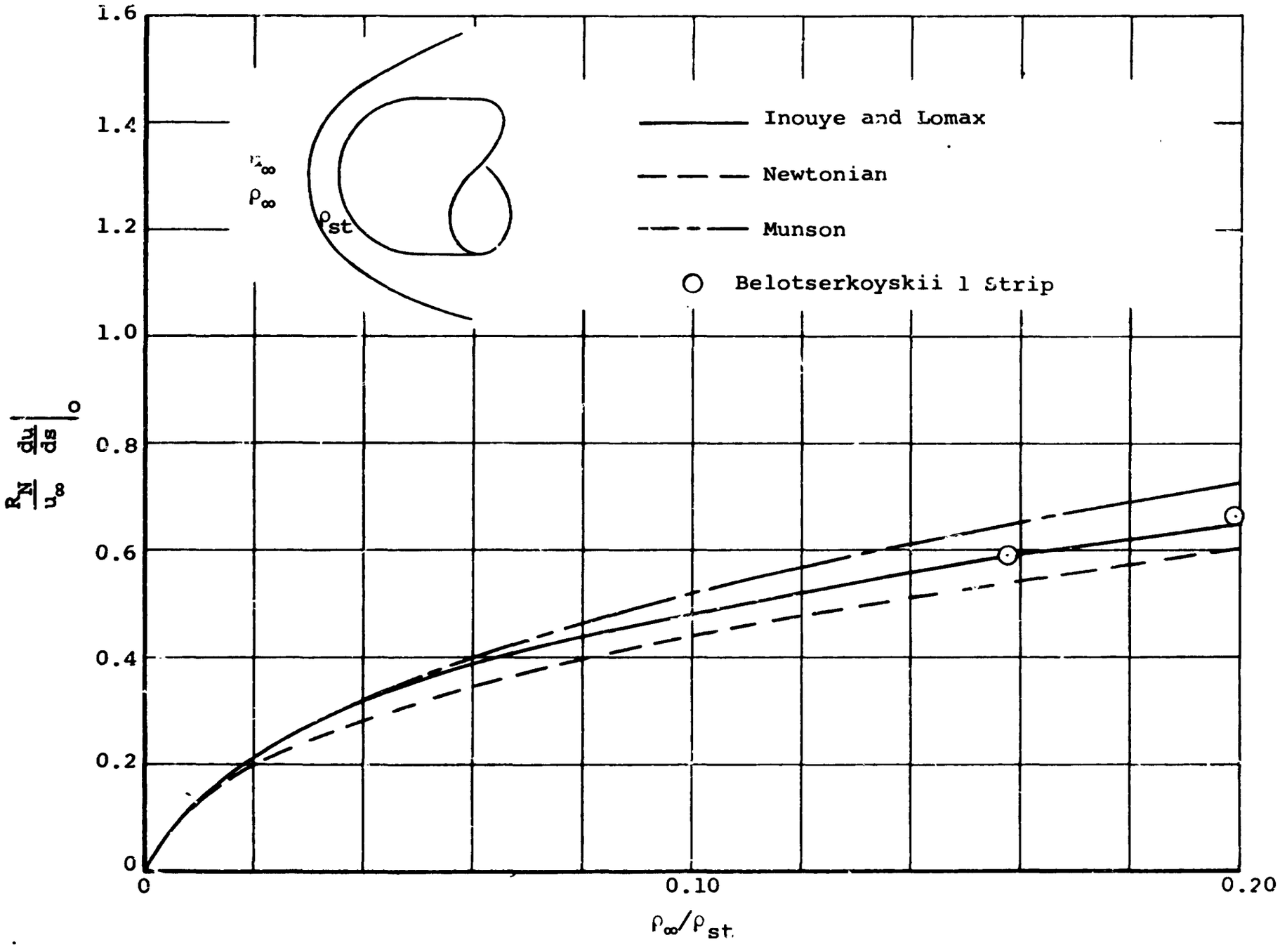

Figure 5.- Stagnation-point velocity gradient parameter for a spherically capped nose.

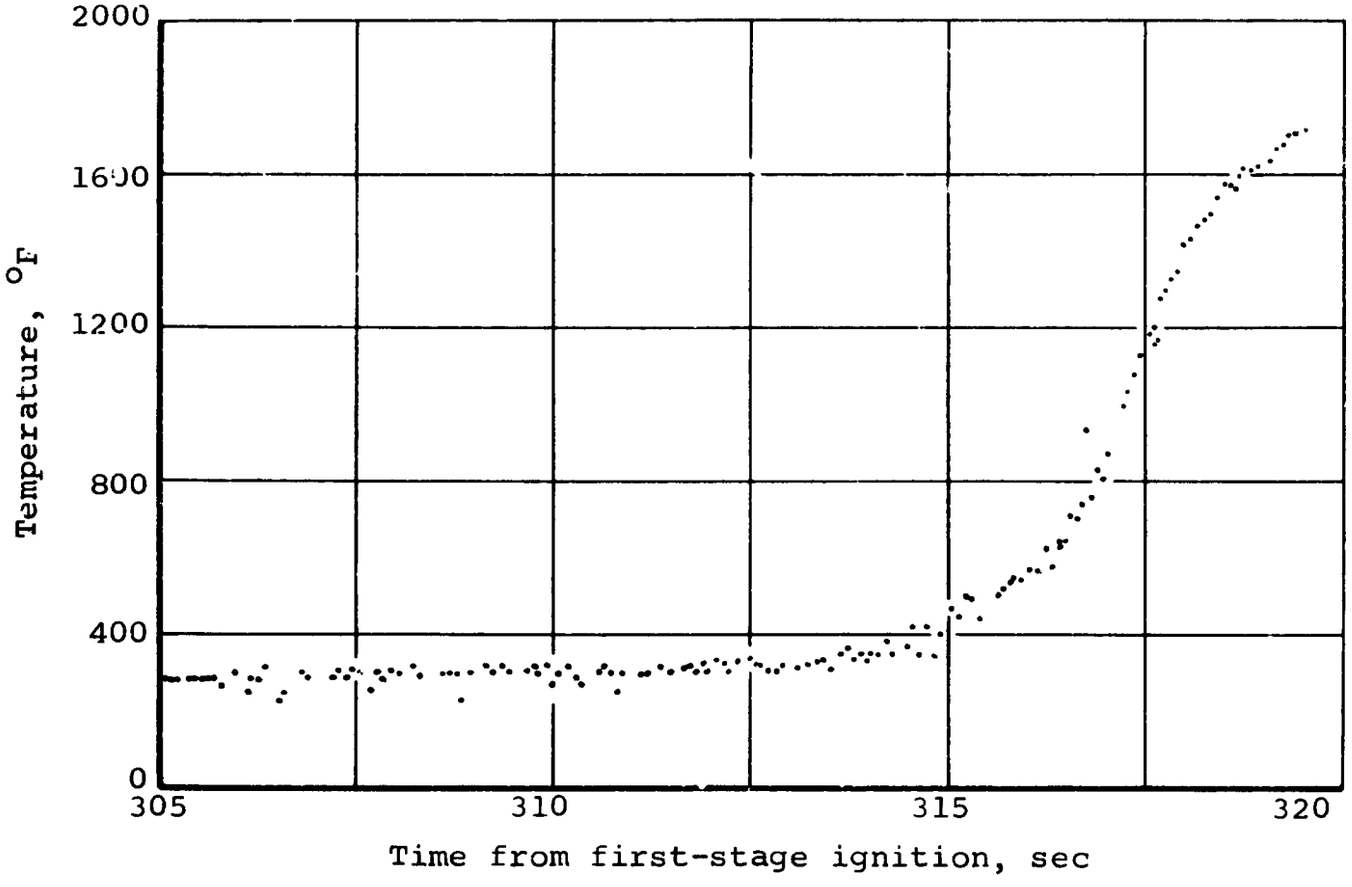

Figure 6.- Typical raw thermocouple data, TC A, R-9.

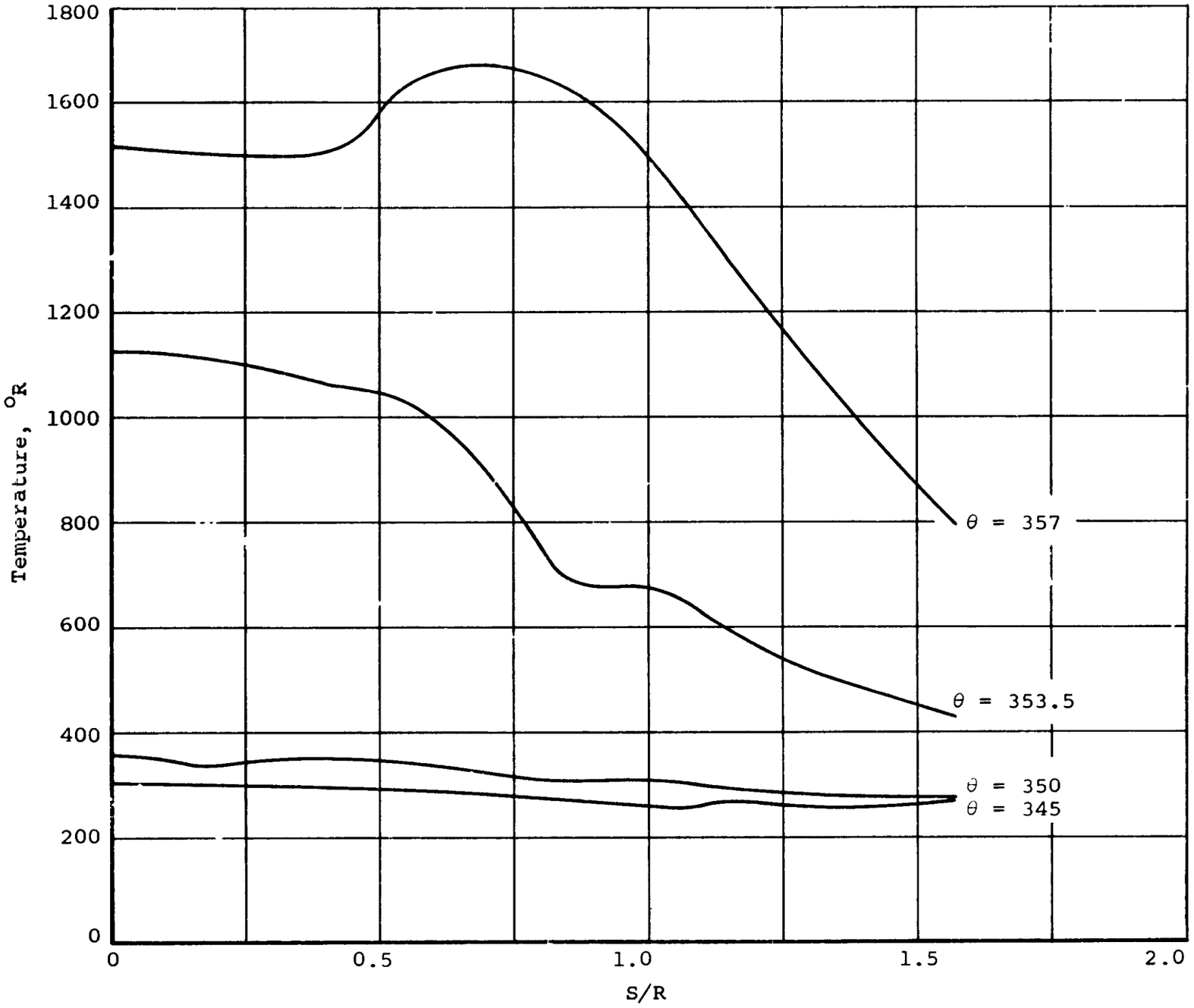

Figure 7.- Streamwise temperature distributions at selected times
X-17 vehicle, R-2.

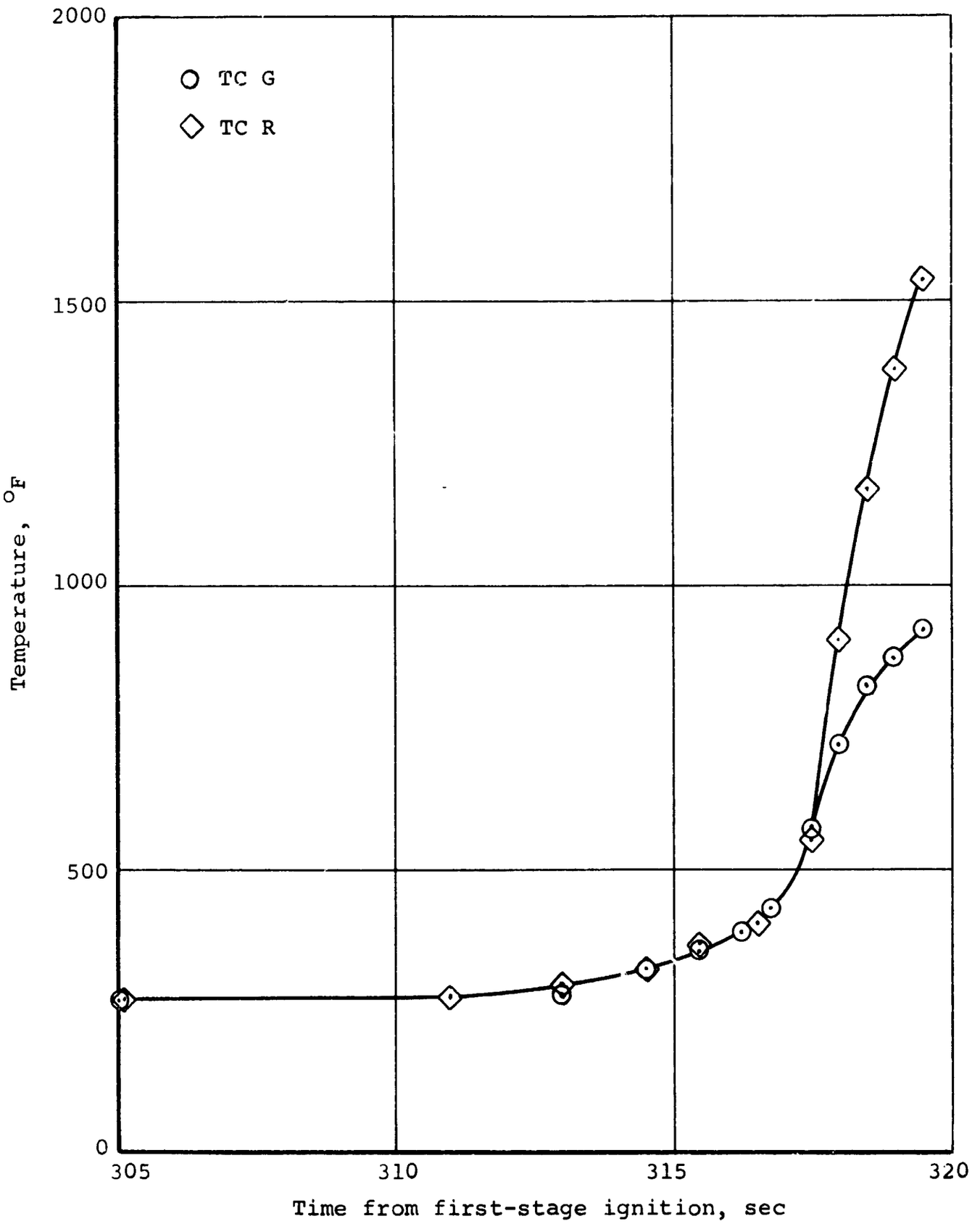

Figure 8.- Smoothed temperature histories on opposite body meridians, X-17 R-9.

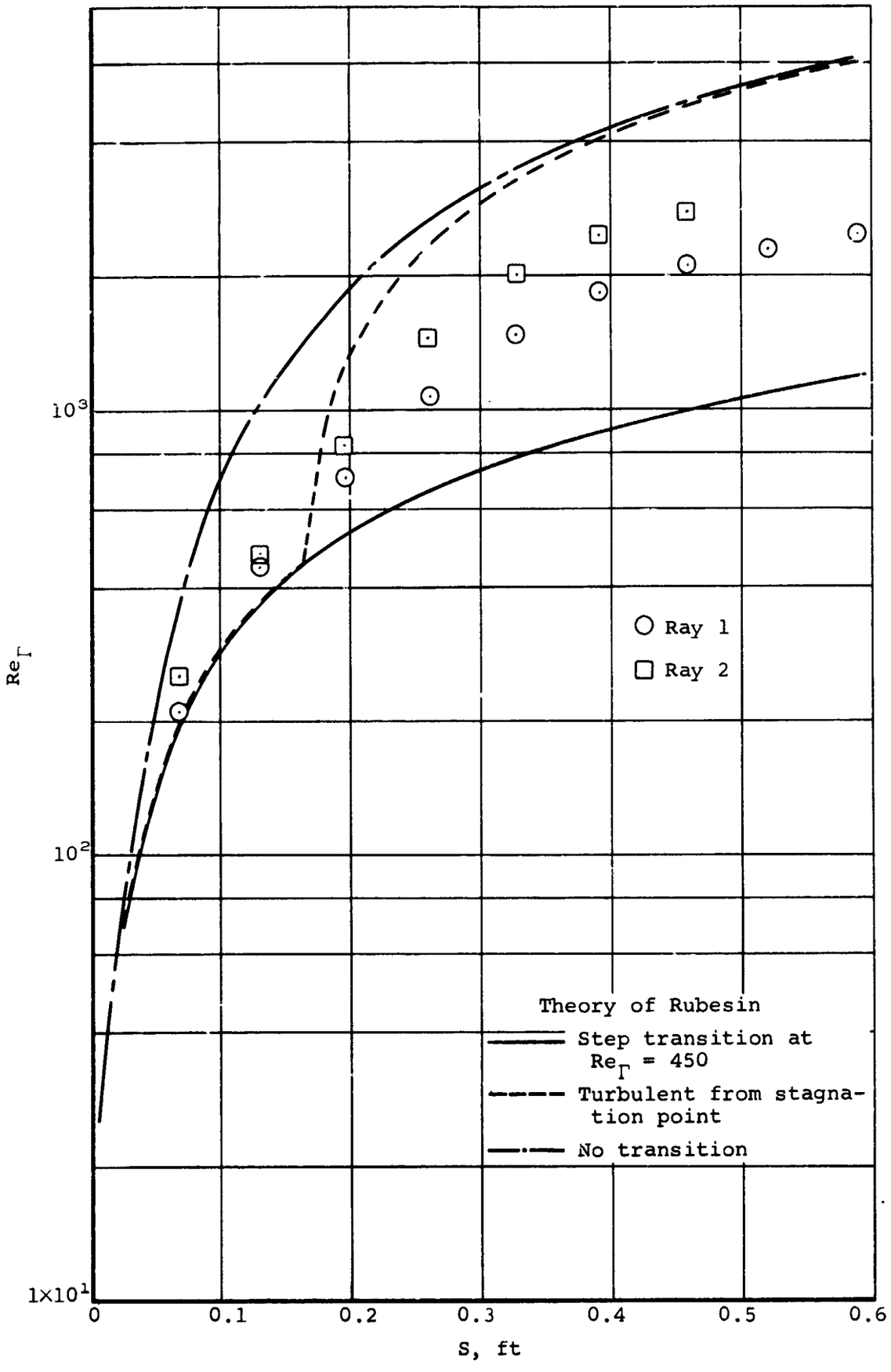

Figure 9.- Comparison of measured and predicted Re_Γ for flight R-2, M_∞ = 10, Z = 31,000 ft.

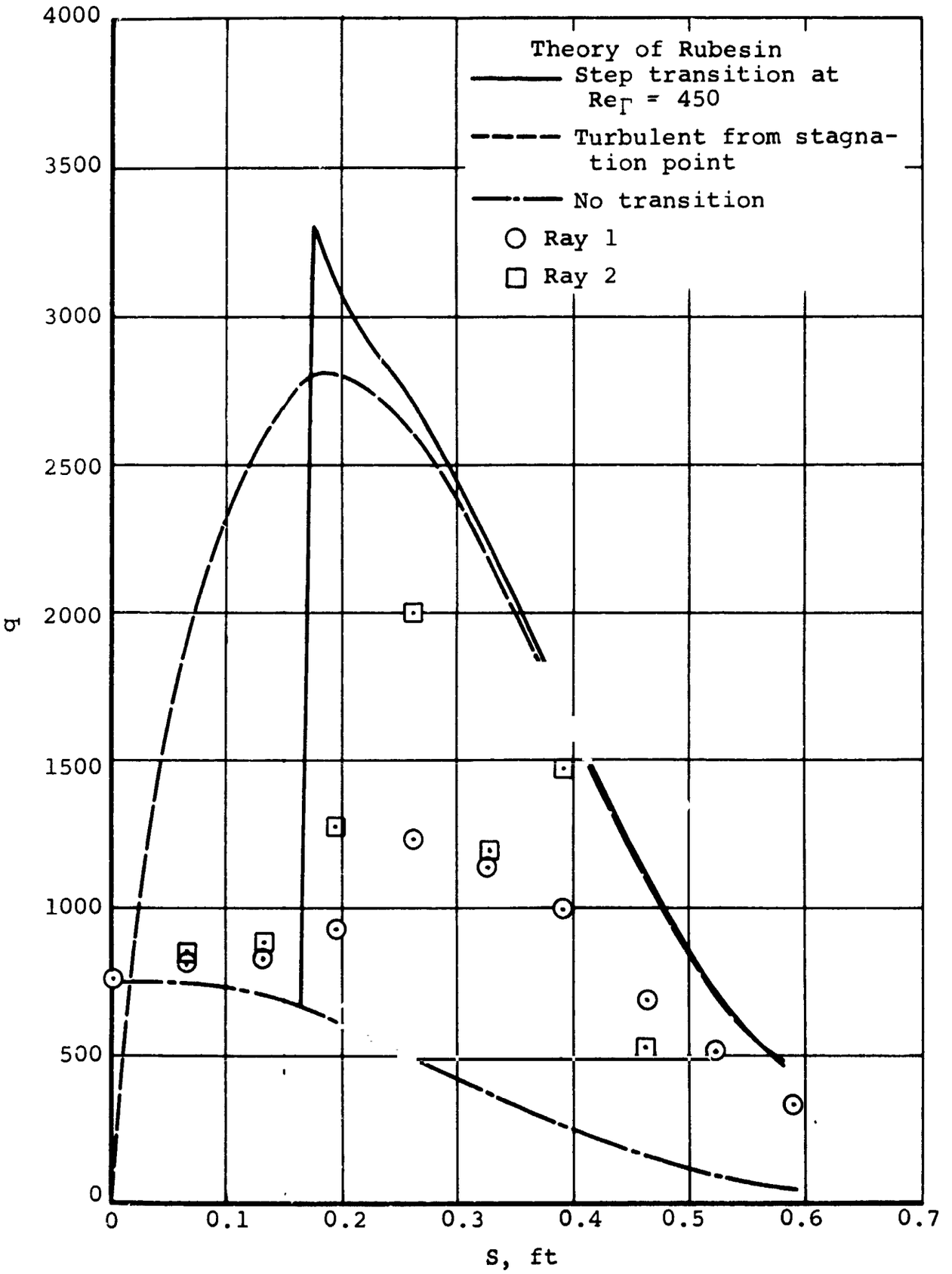

Figure 10.- Axial distribution of heat flux over the X-17 R-2, M_∞ = 10, Z = 31,000 ft.

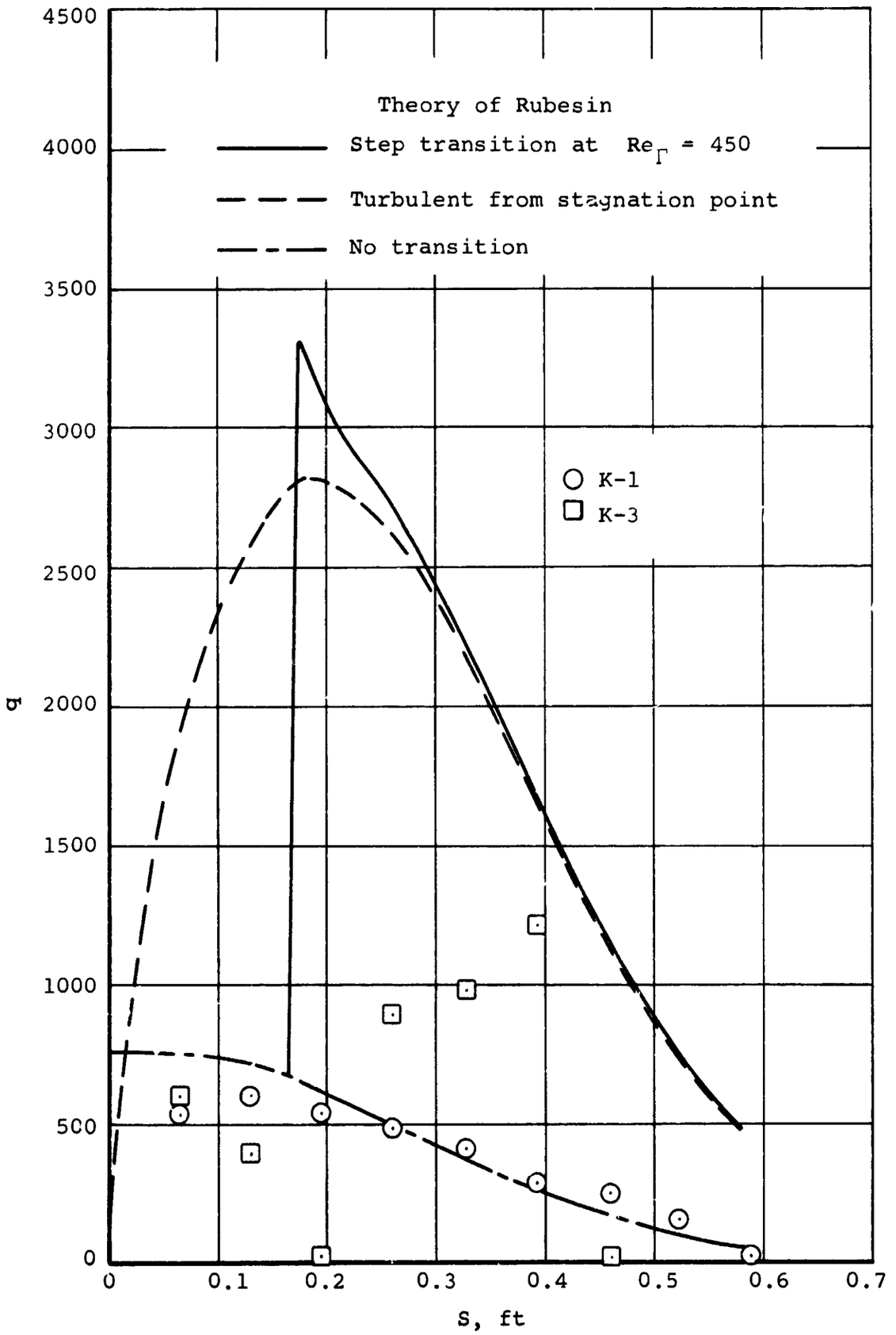

Figure 11.- Axial distribution of heat flux over the X-17 R-9, M_∞ = 10, Z = 31,000 ft.

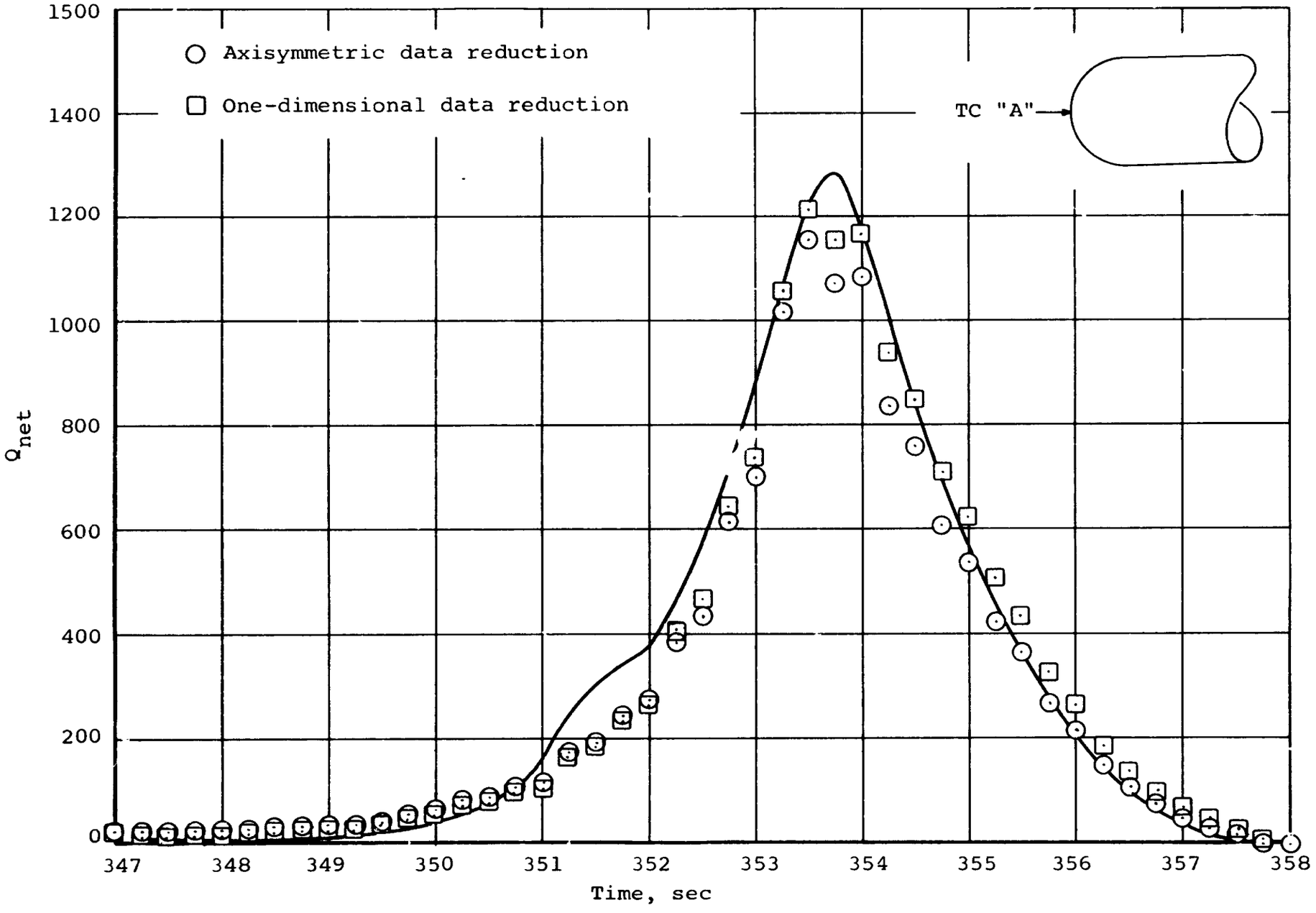

Figure 12.- Comparison of experimental and predicted heat-transfer rate, X-17 vehicle R-2, thermocouple "A", S/R = 0.

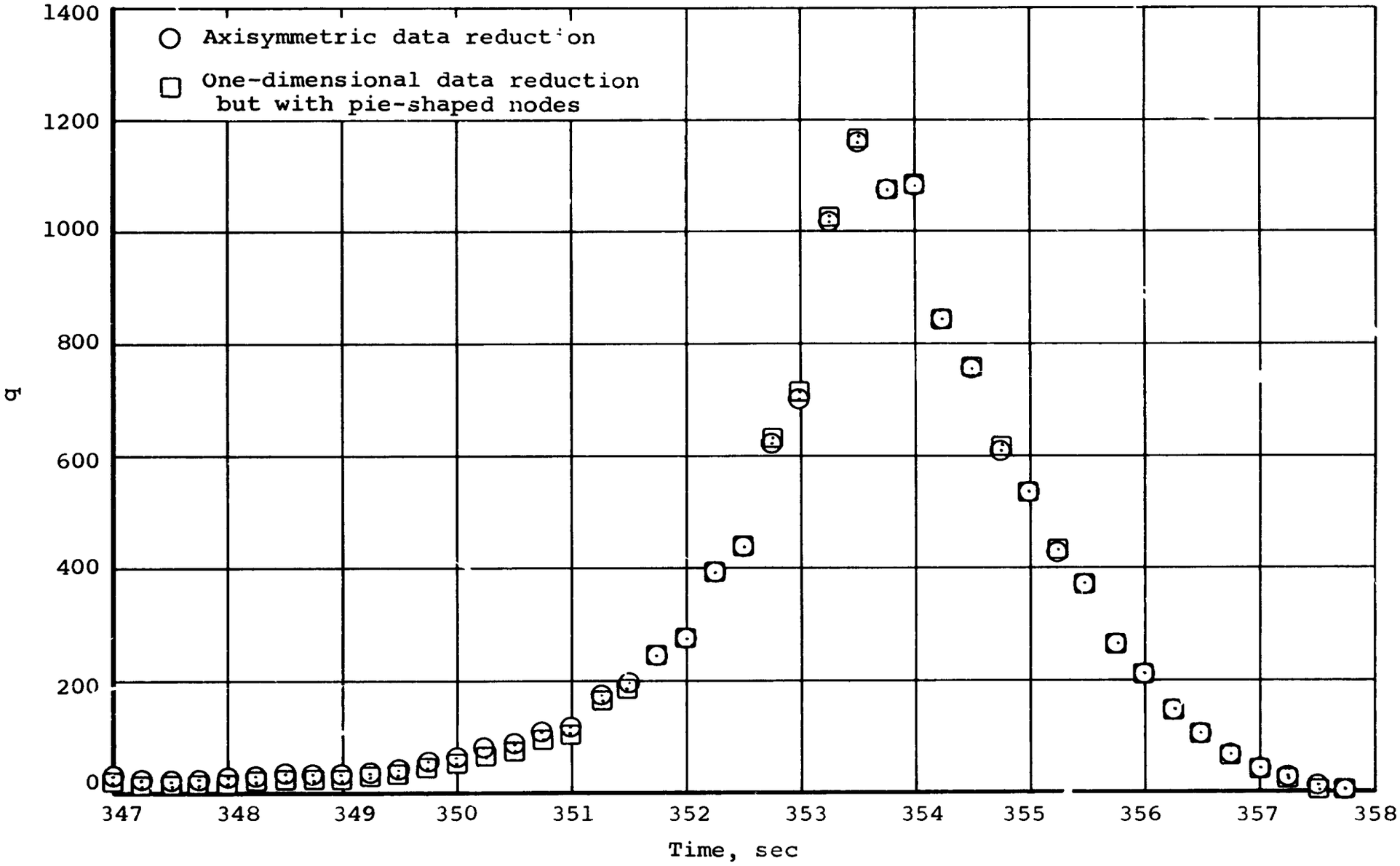

Figure 13.- Effects of body curvature on stagnation-point heating rate as inferred fron one- and two-dimensional data reduction.

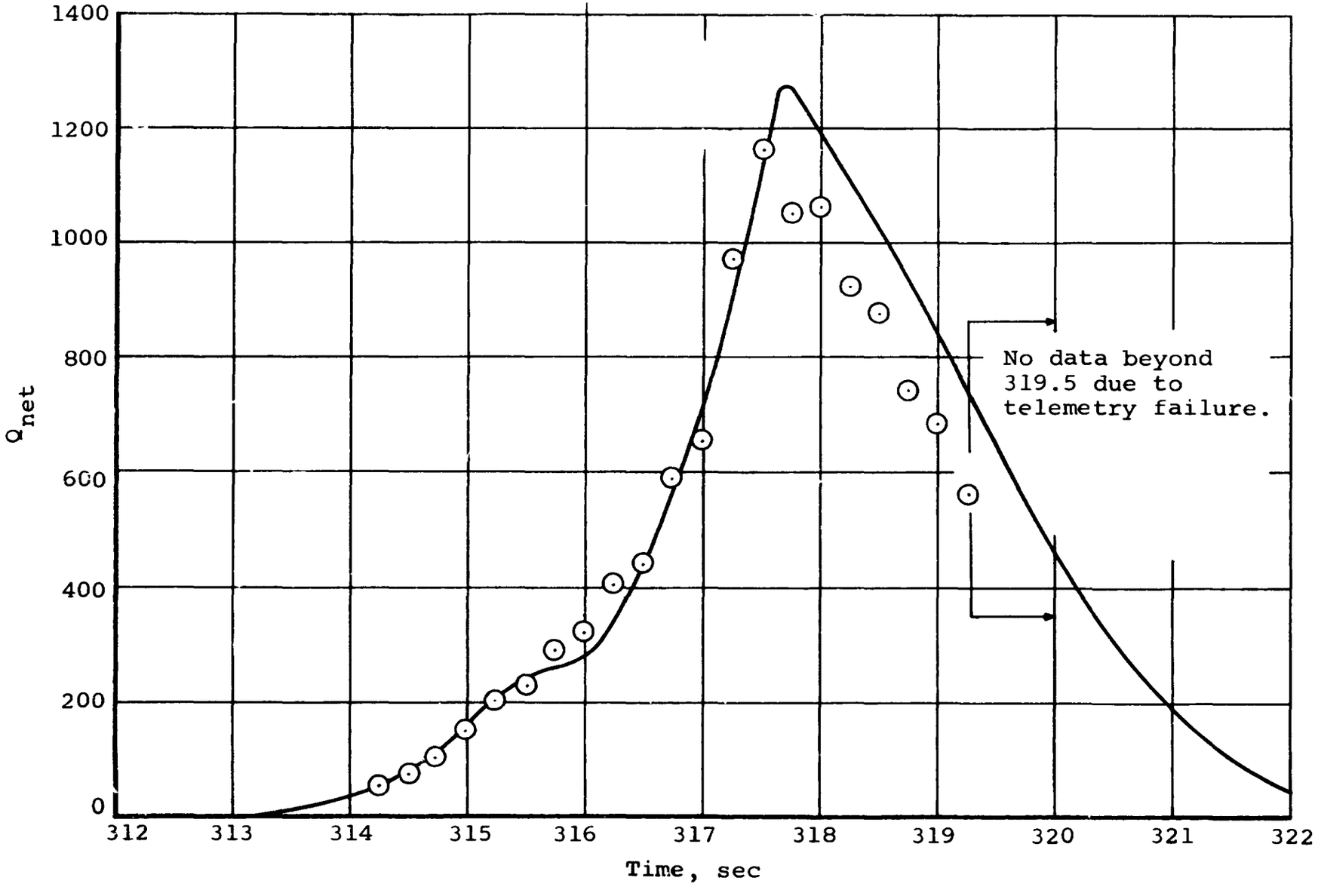

Figure 14.- Comparison of experimental and predicted heat-transfer rate, X-17 vehicle R-9, thermocouple "A", S/R = 0.

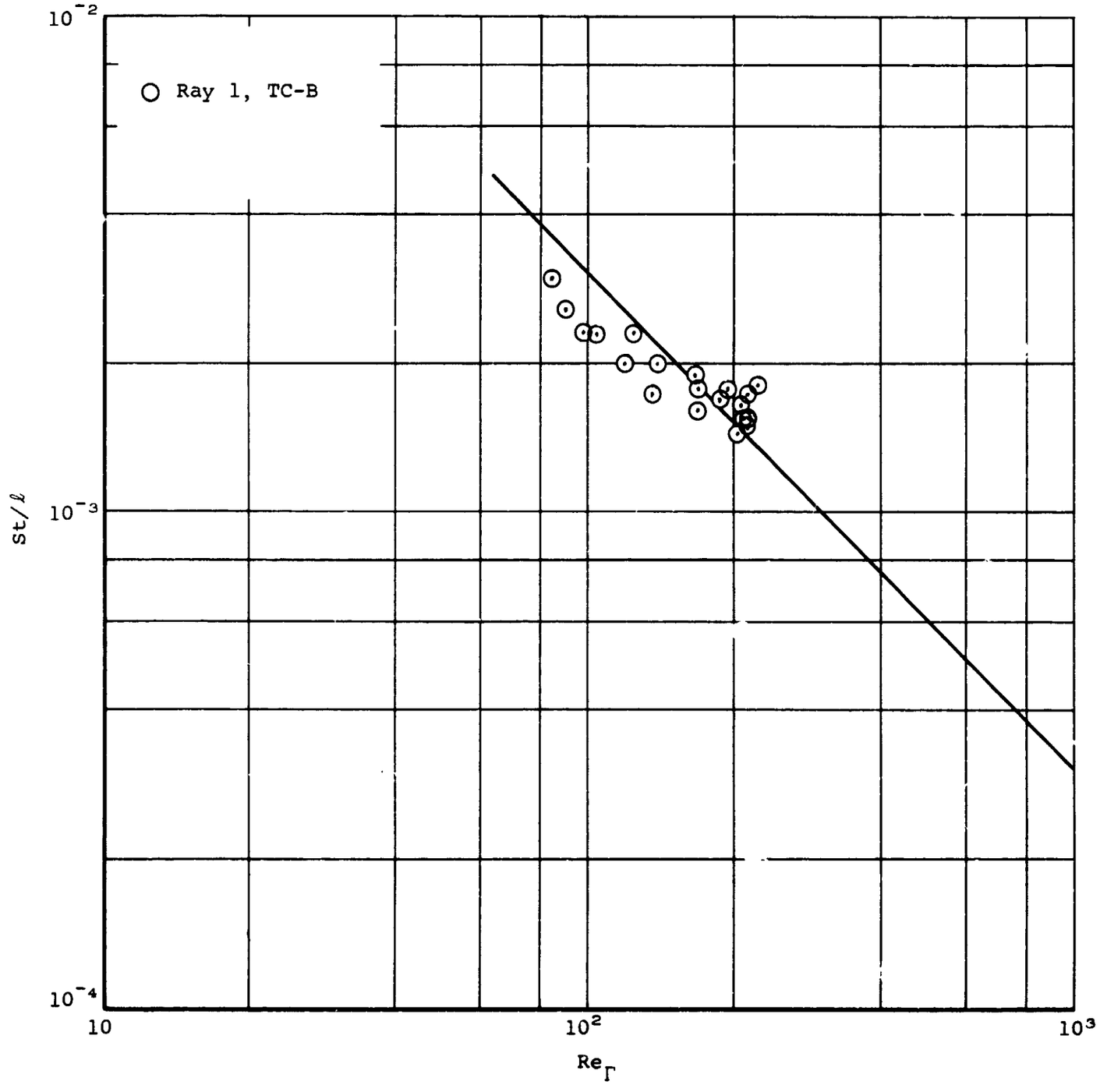

(a) $S/R = 10^{o}$.

Figure 15.- Heat-transfer correlations, X-17 R-2.

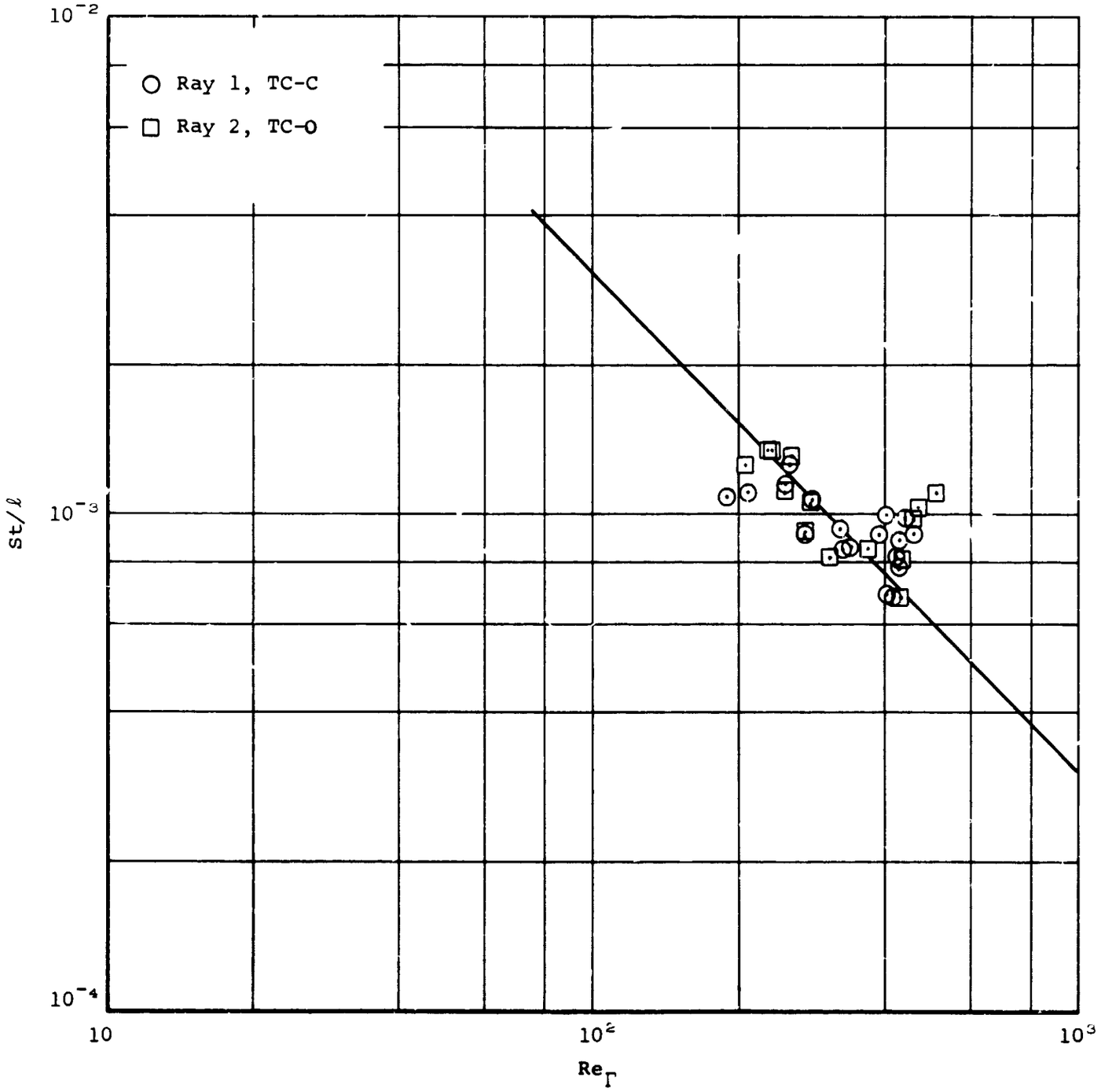

(b) S/R = 20°.

Figure 15.- Continued.

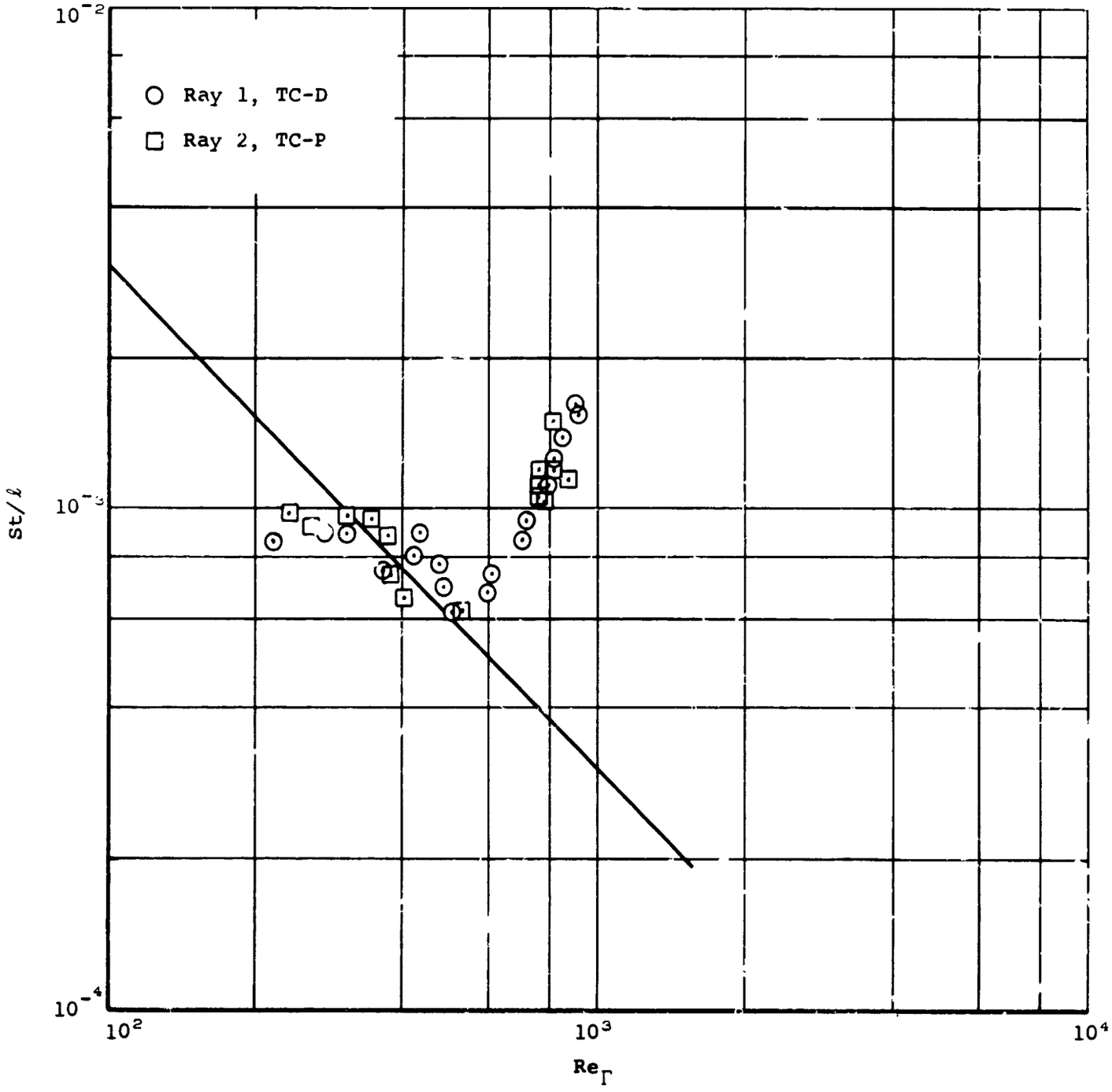

(c) S/R = 30°.

Figure 15.- Continued.

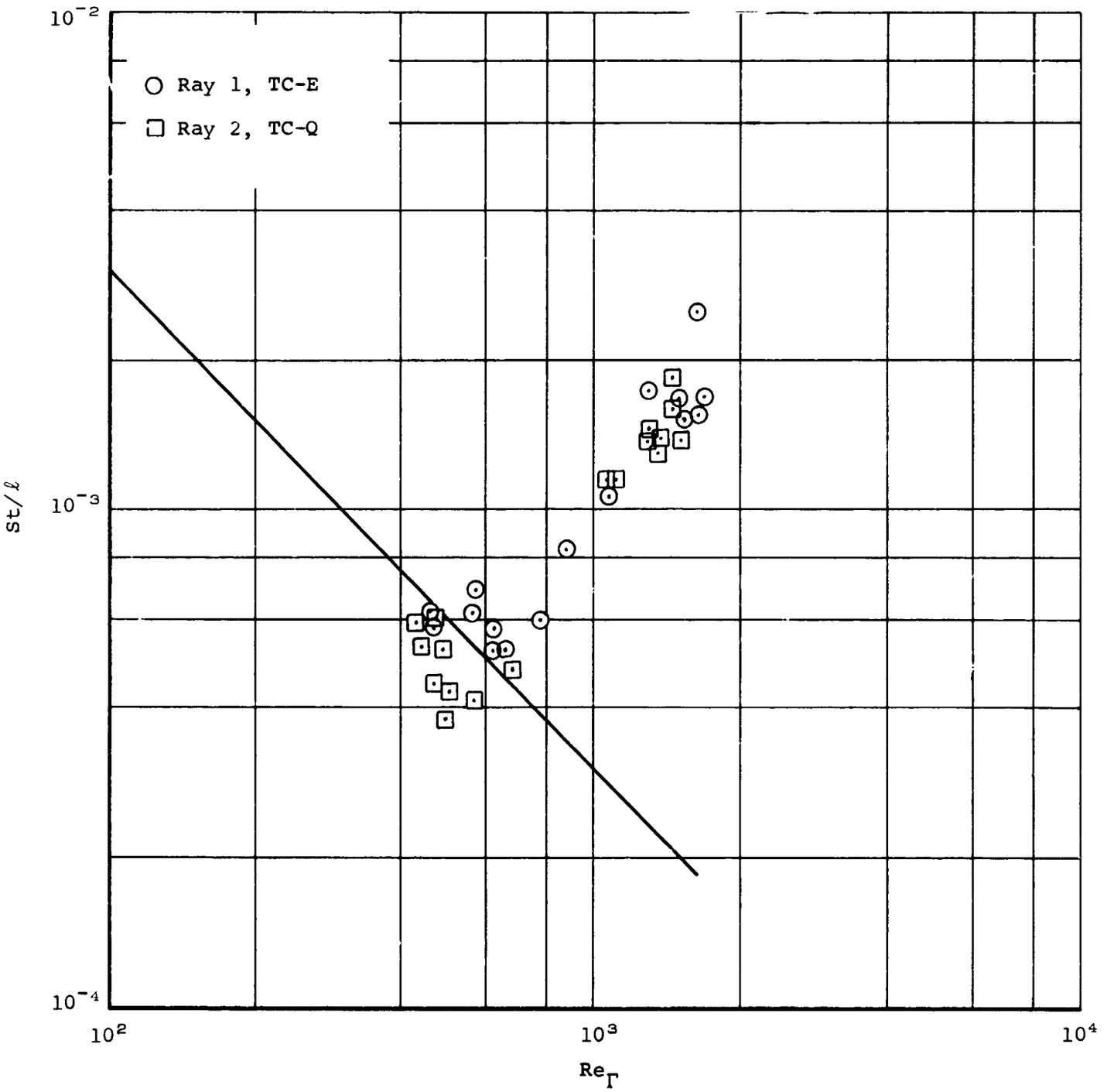

(d) S/R = 40°.

Figure 15.- Continued.

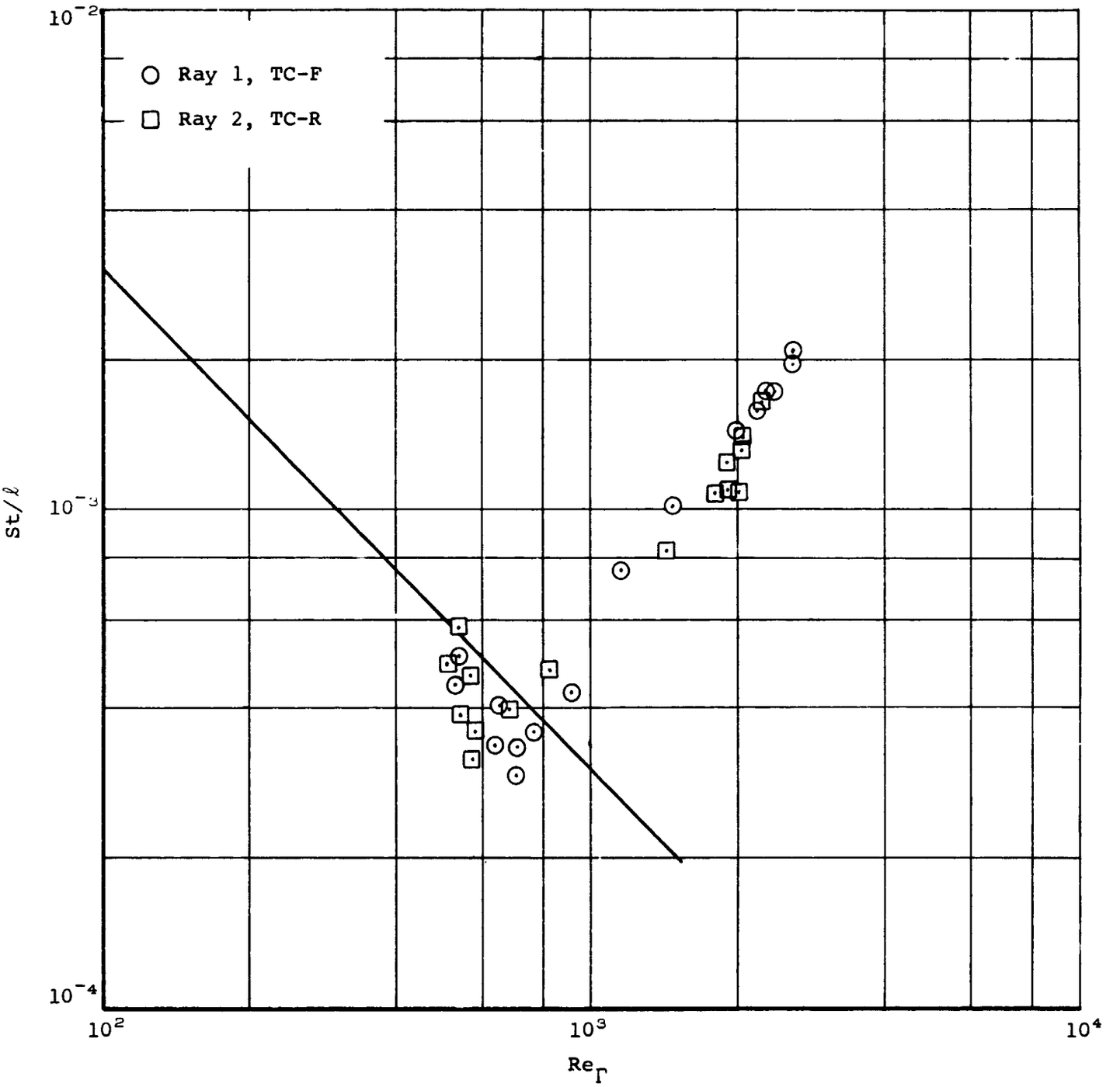

(e) S/R = 50°.

Figure 15.- Continued.

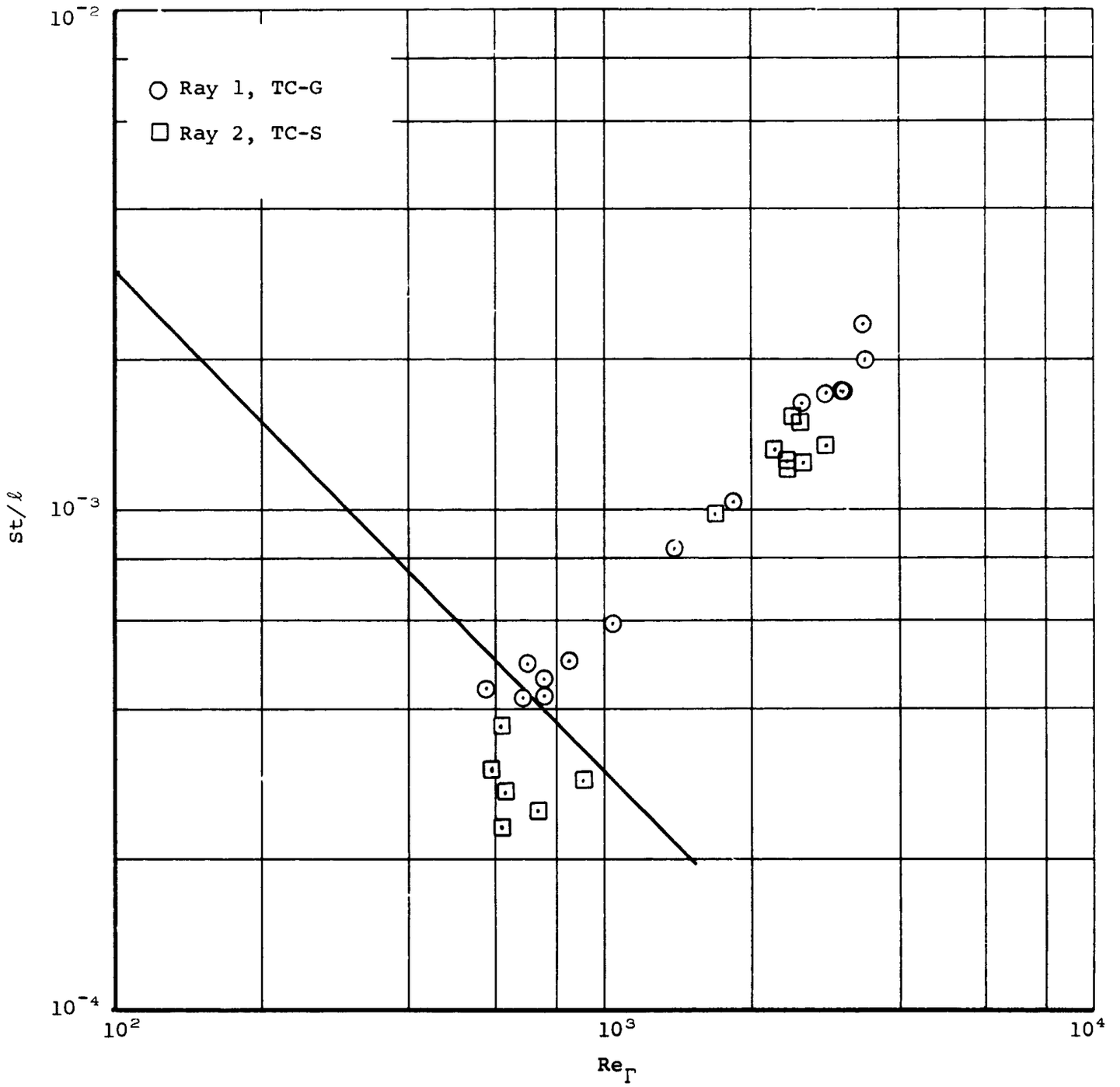

(f) S/R = 60°.

Figure 15.- Continued.

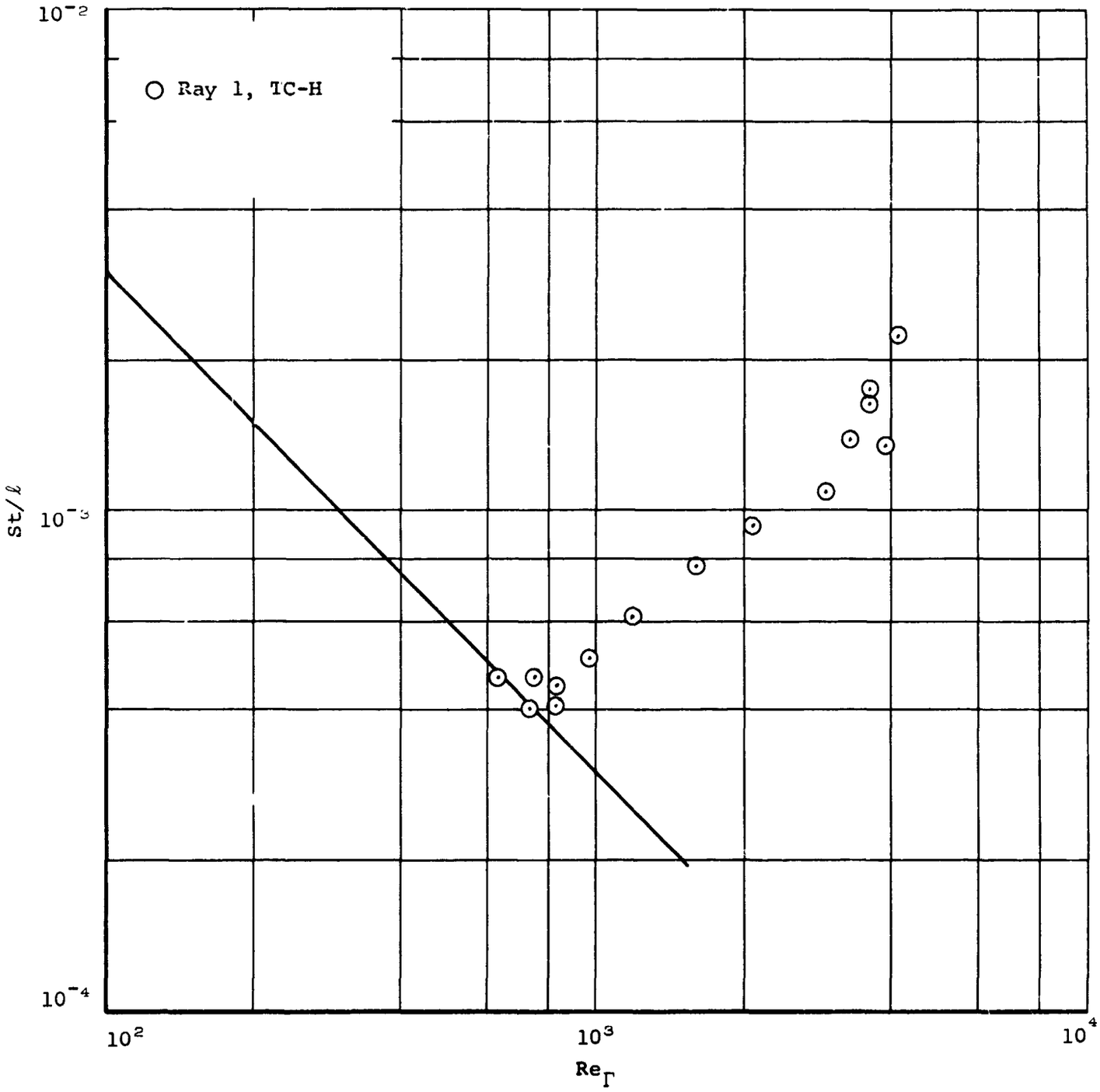

(g) S/R = 70°.

Figure 15.- Continued.

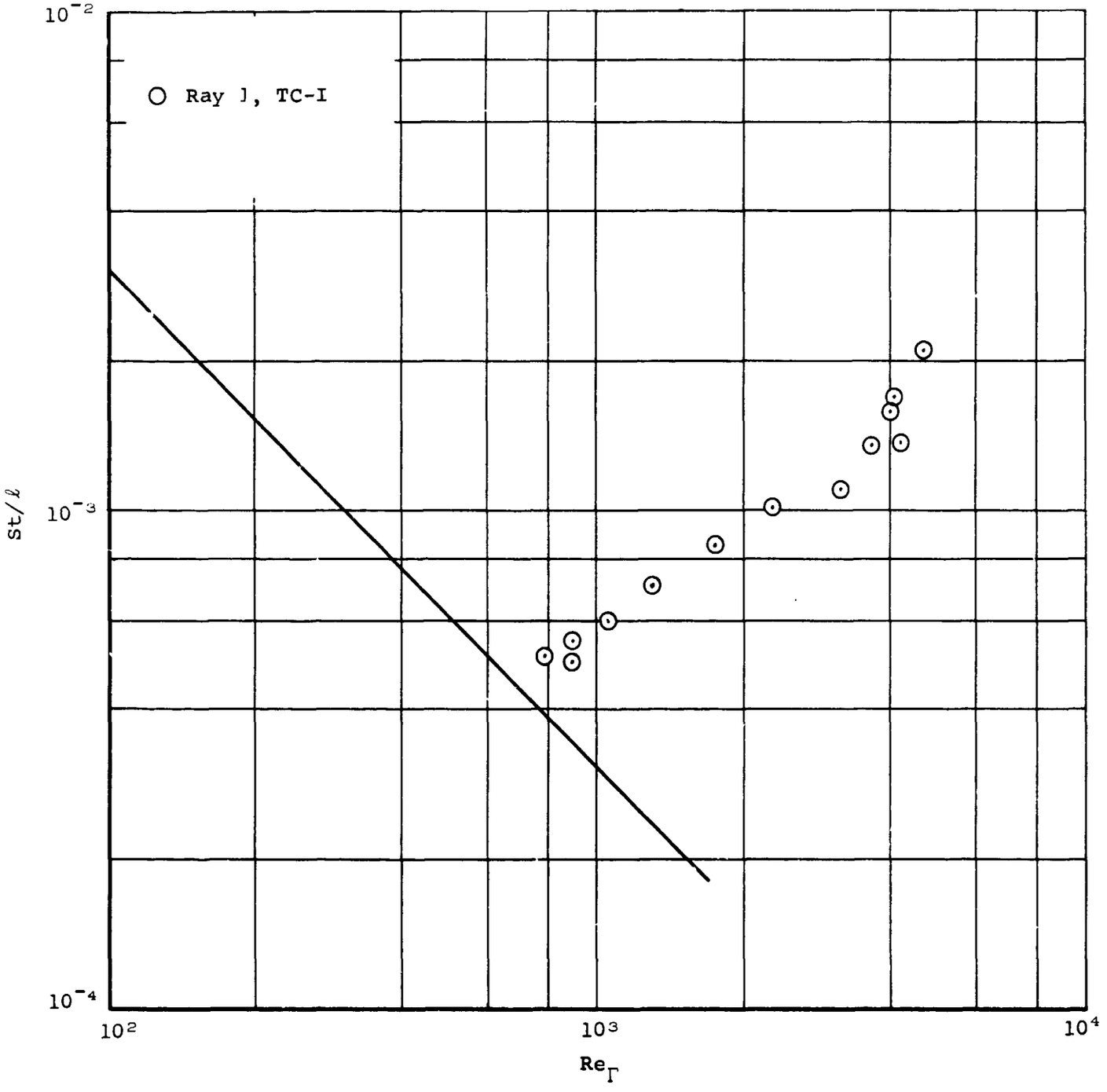

(h) S/R = 80°.

Figure 15.- Concluded.

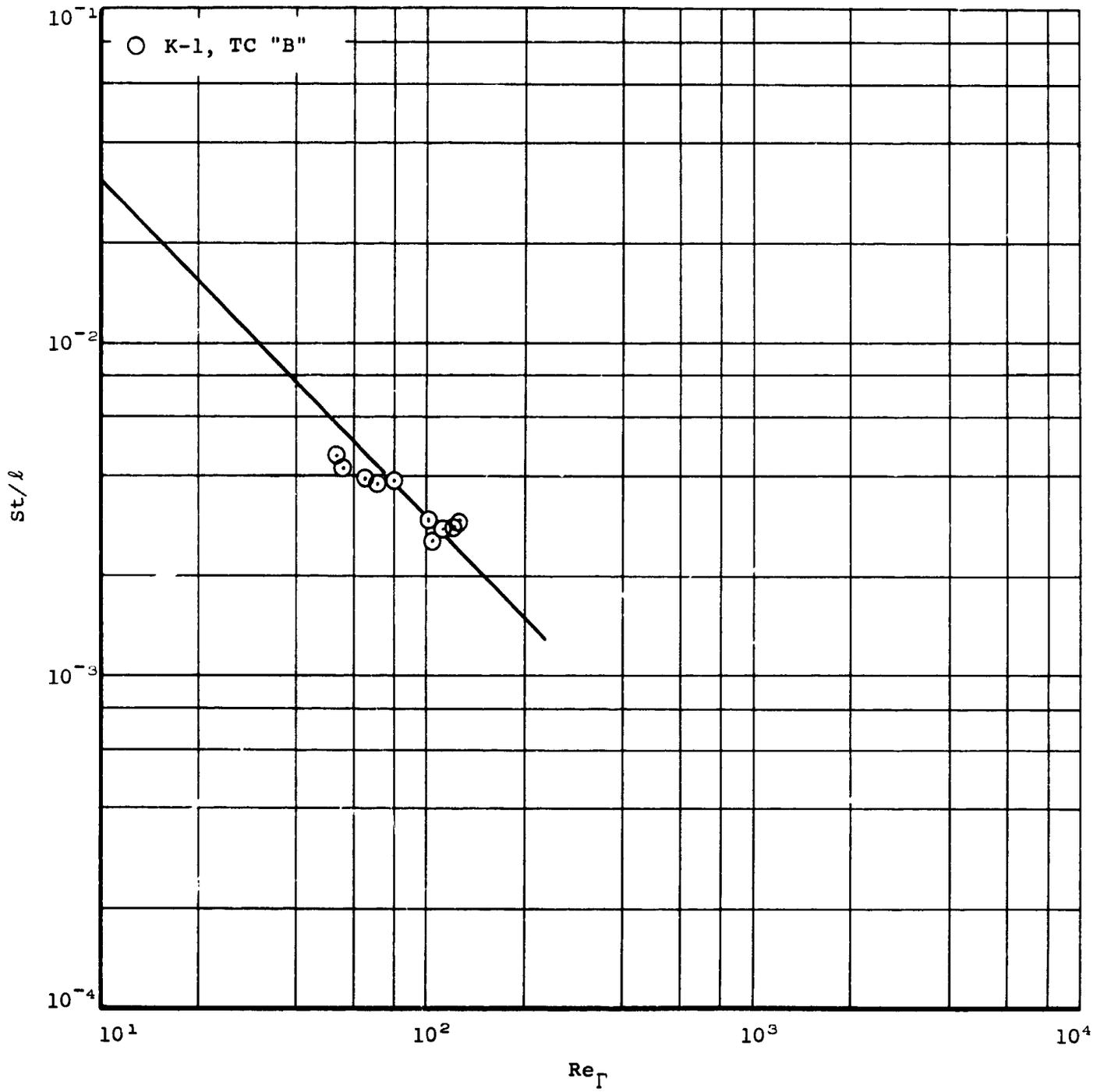

(a) $S/R = 10^{o}$.

Figure 16.- Heat-transfer correlations, X-17 R-9.

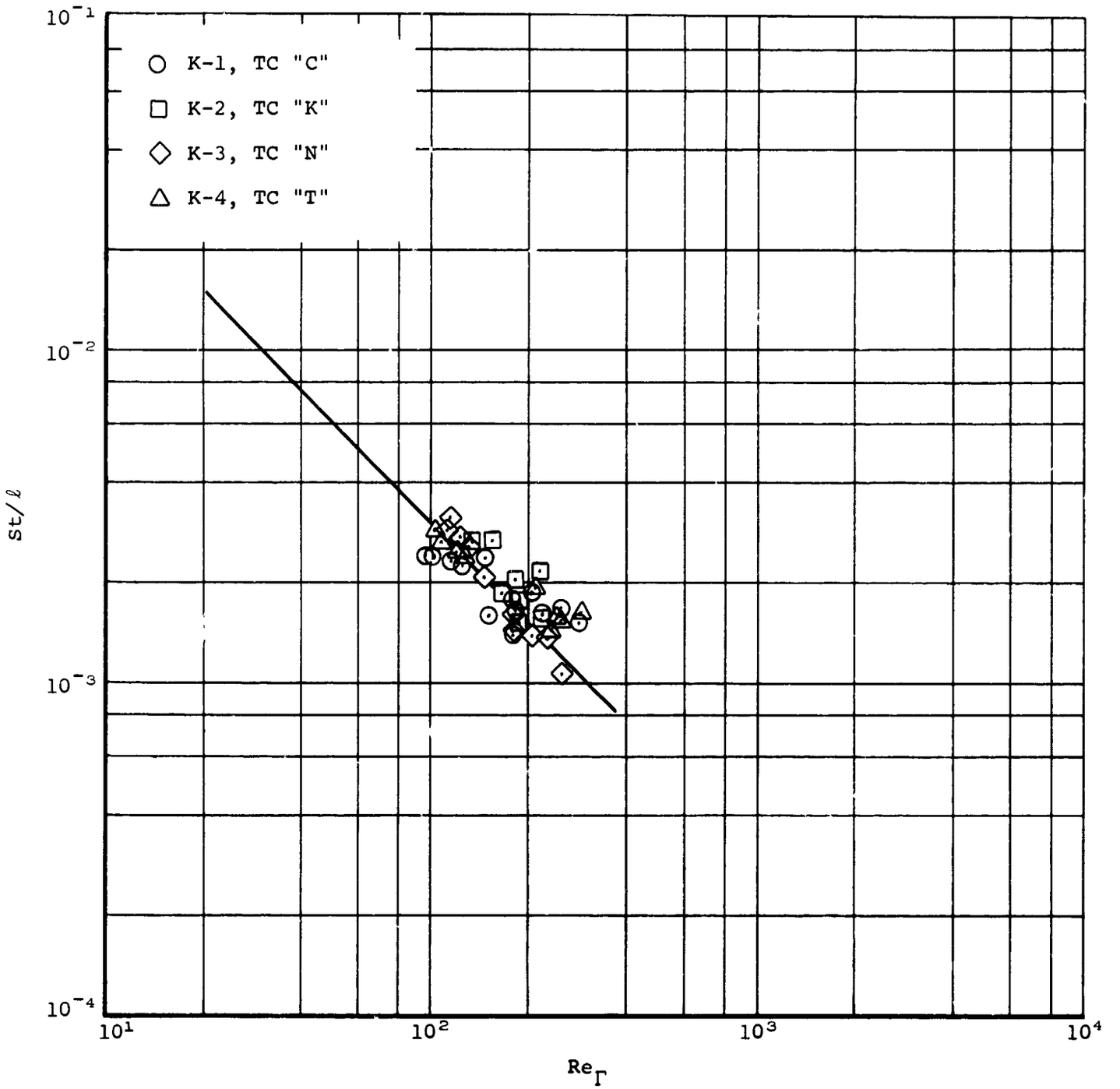

(b) S/R = 20°.

Figure 16.- Continued.

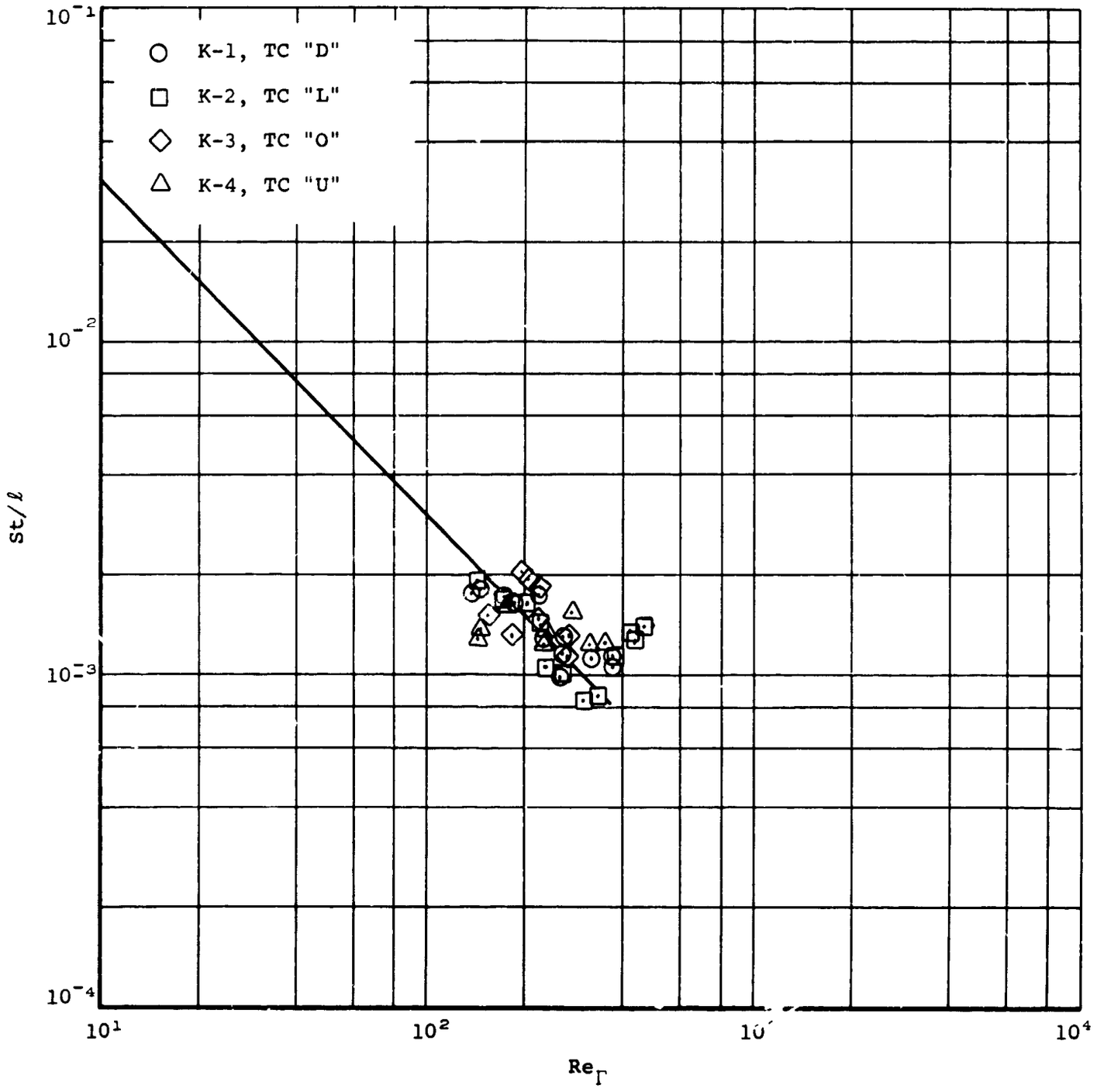

(c) S/R = 30°.

Figure 16.- Continued.

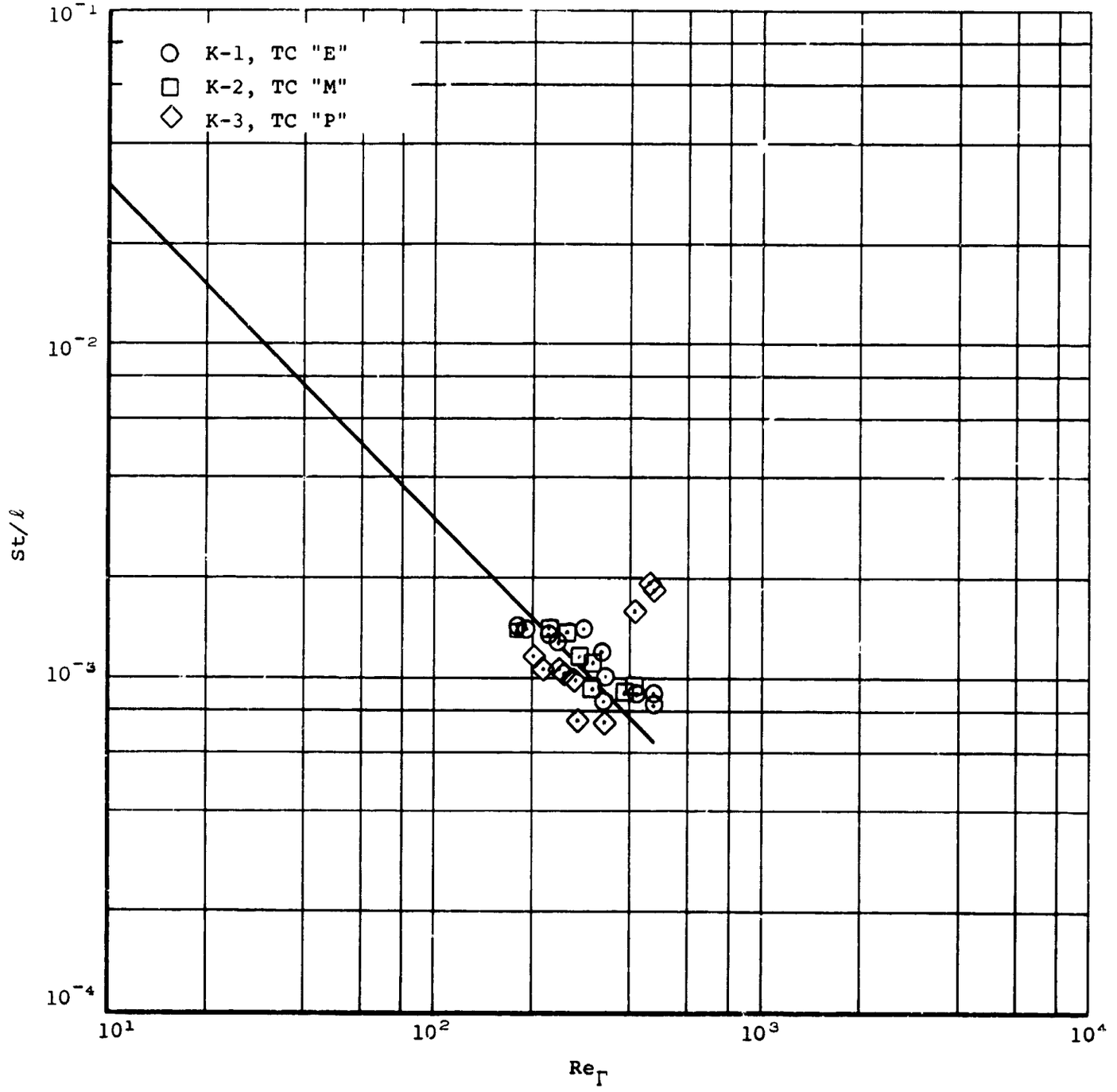

(d) $\varepsilon/R = 40^{\circ}$.

Figure 16.- Continued.

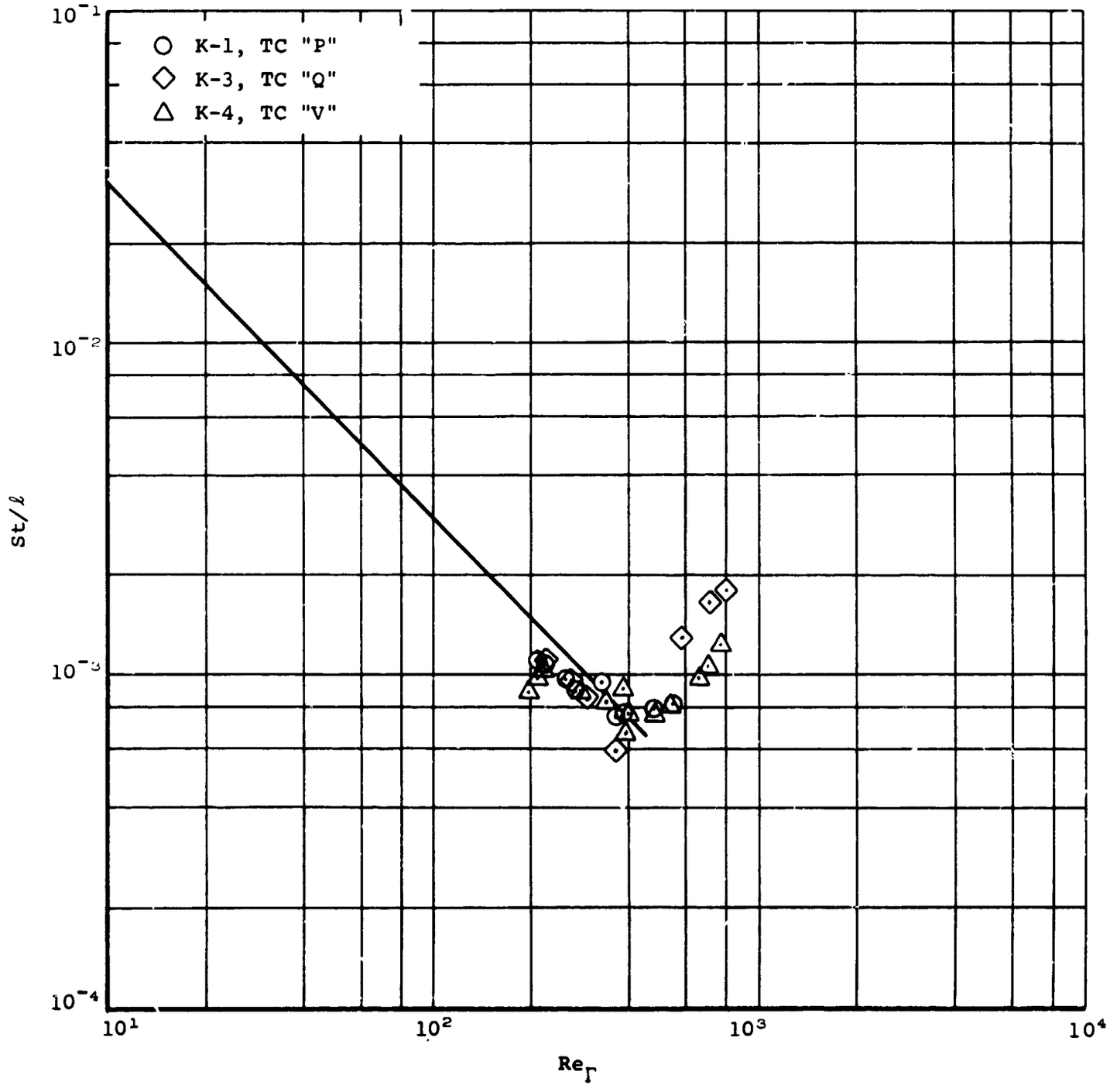

(e) S/P = 50°.

Figure 16.- Continued.

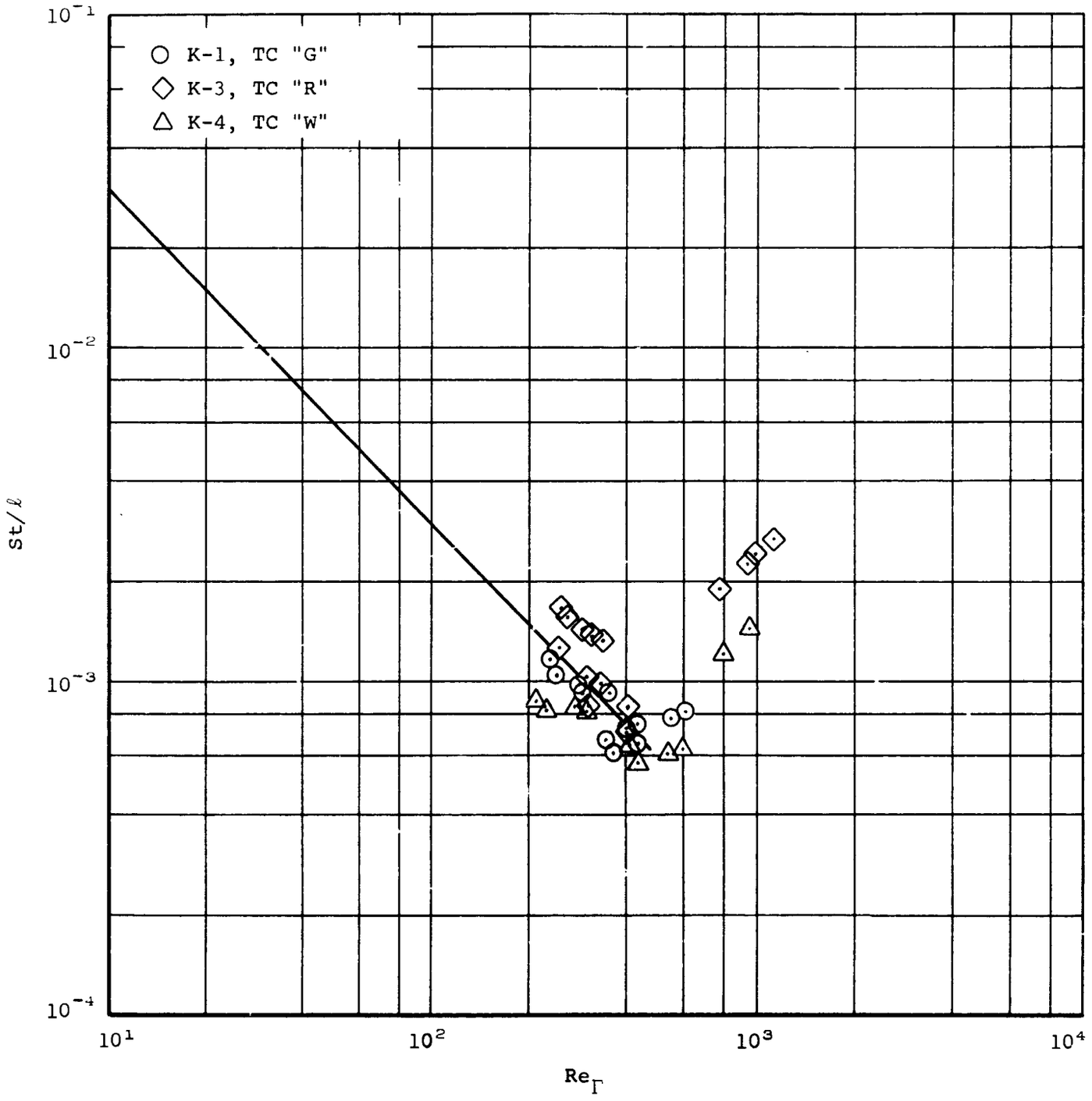

(f) S/R = 60°.

Figure 16.- Continued.

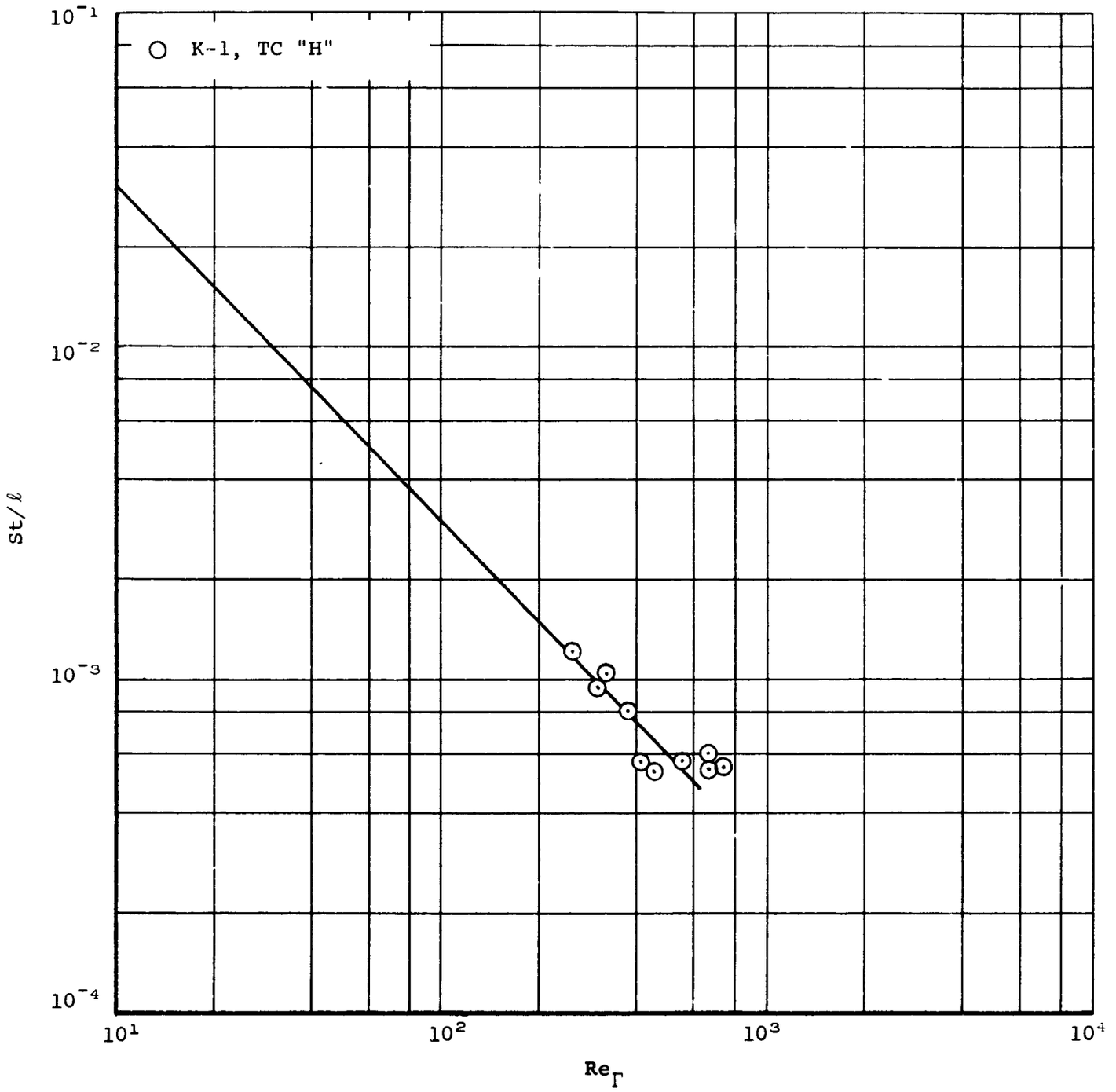

(g) S/R = 70°.

Figure 16.- Continued.

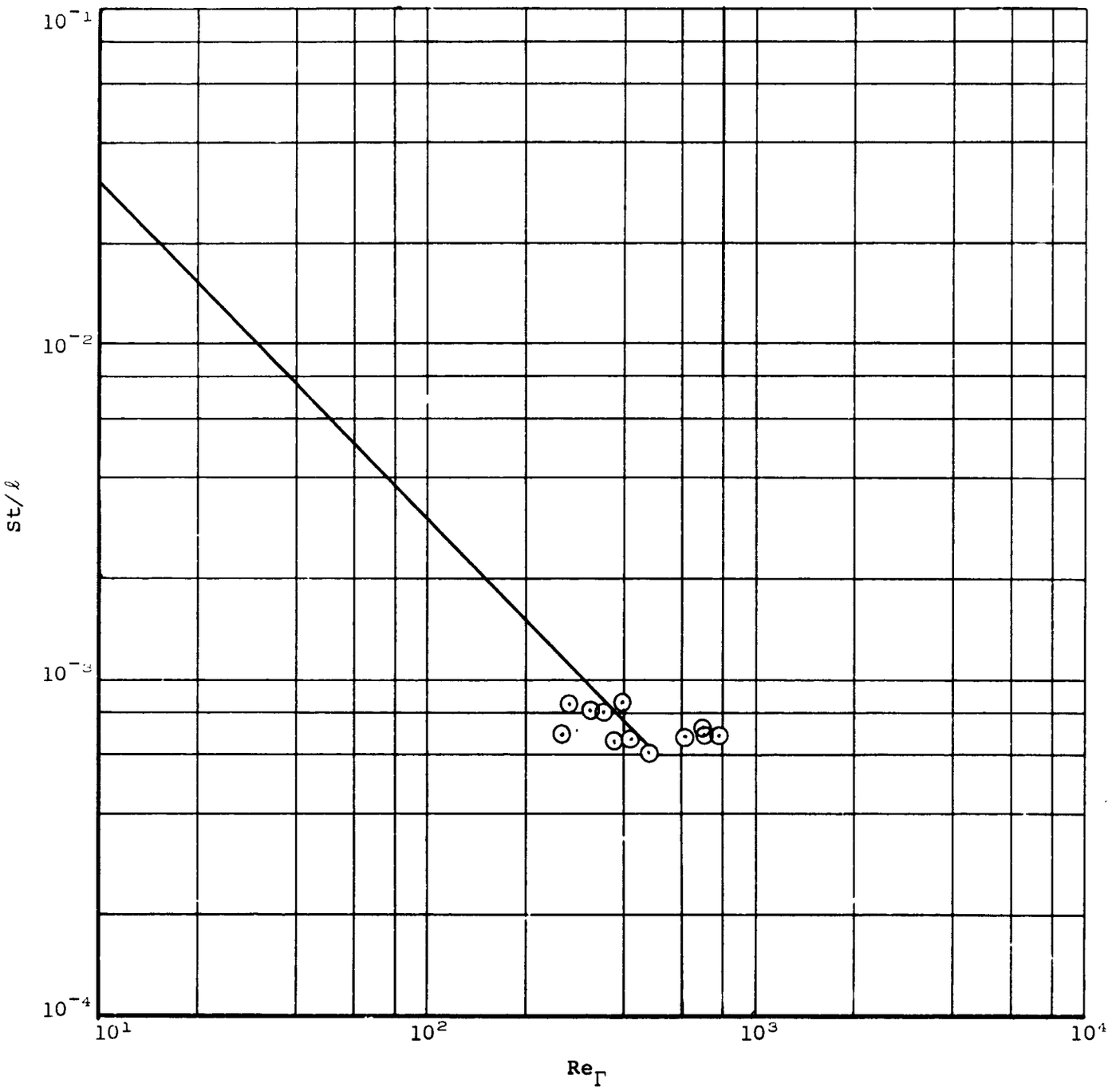

(h) S/R = 80°.

Figure 16.- Concluded.

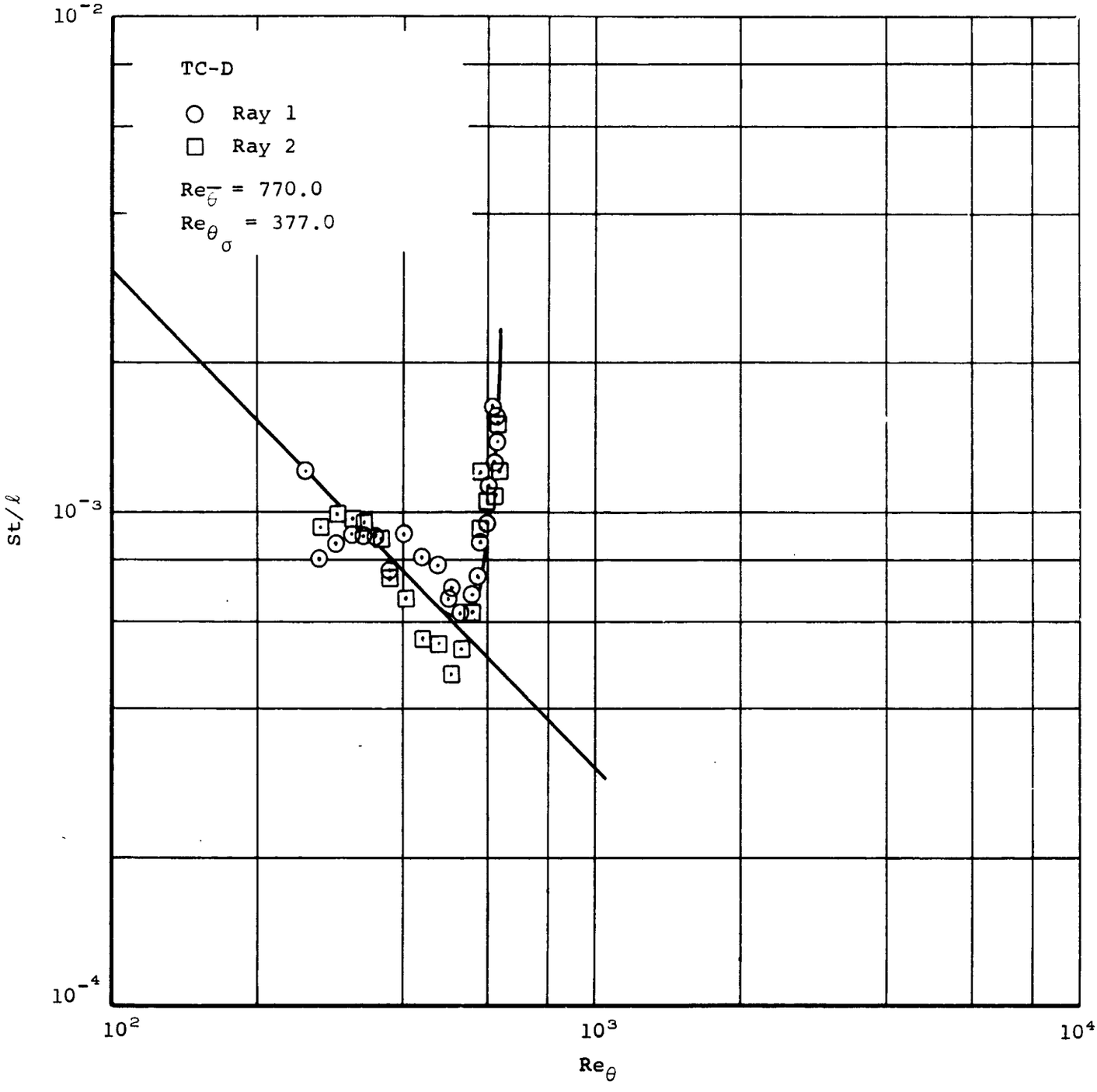

(a) S/R = 30°.

Figure 17.- Correlation of transitional boundary-layer heating, X-17 vehicle R-2.

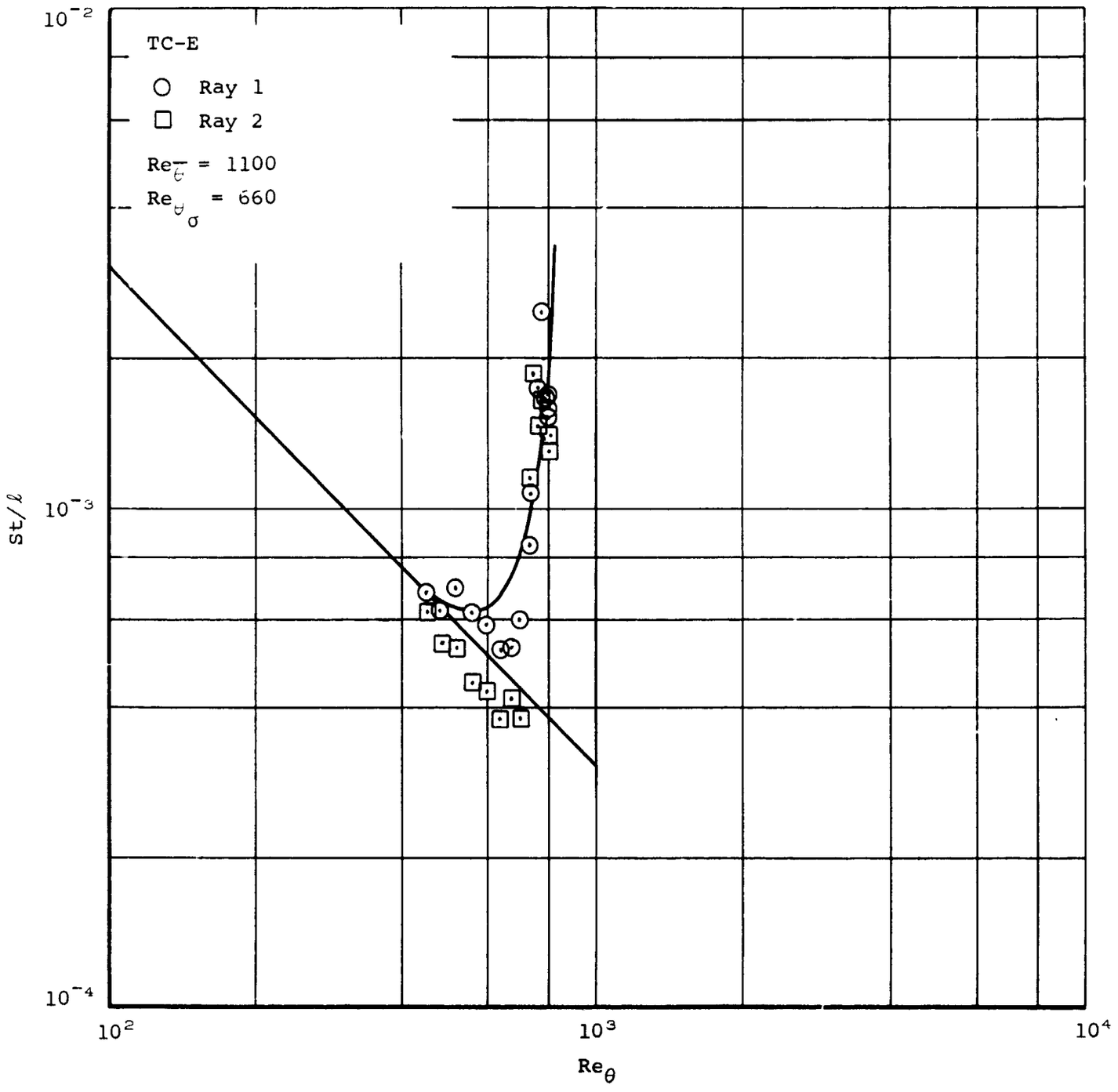

(b) S/R = 40°.

Figure 17.- Continued.

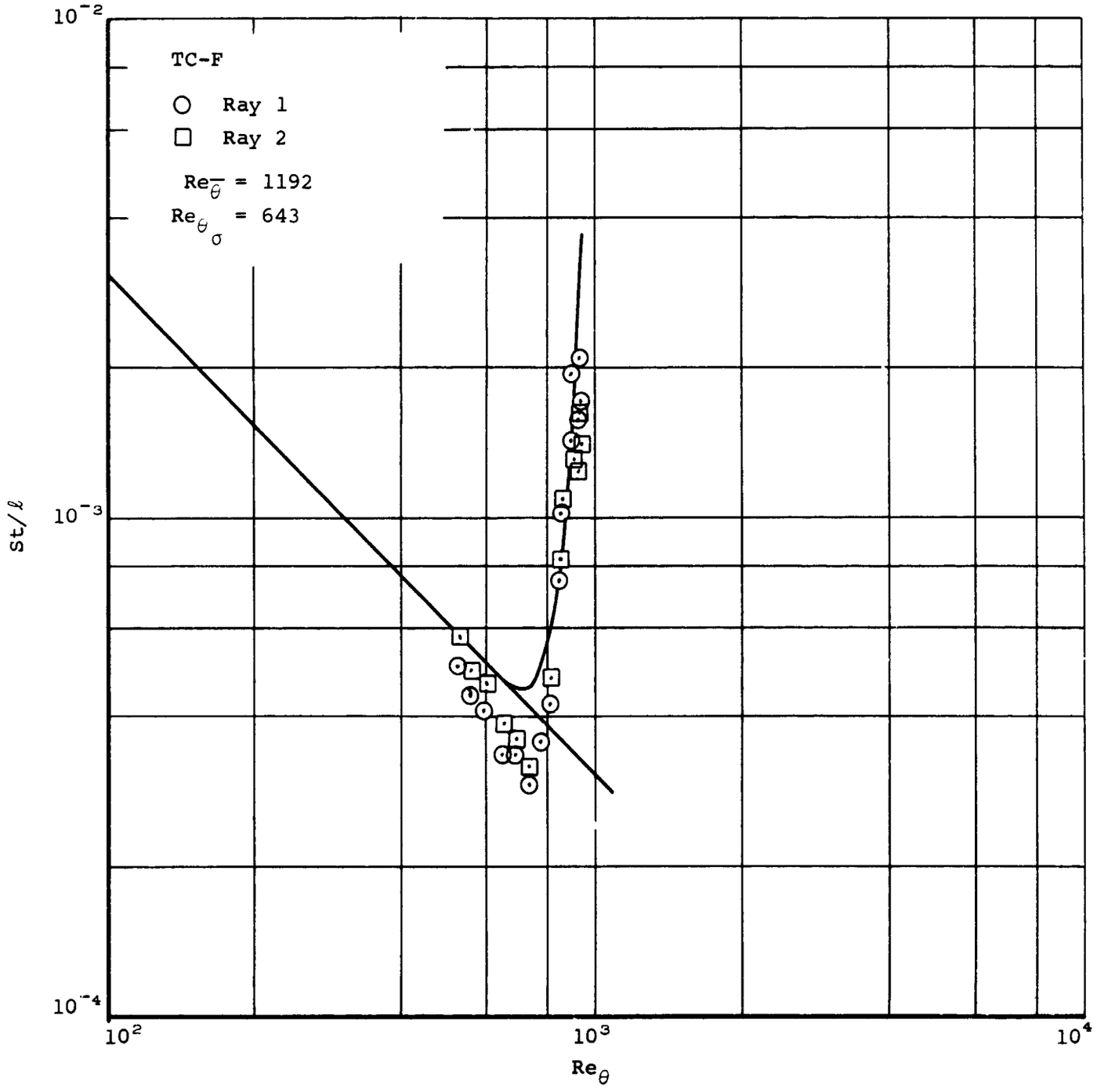

(c) S/R = 50°.

Figure 17.- Continued.

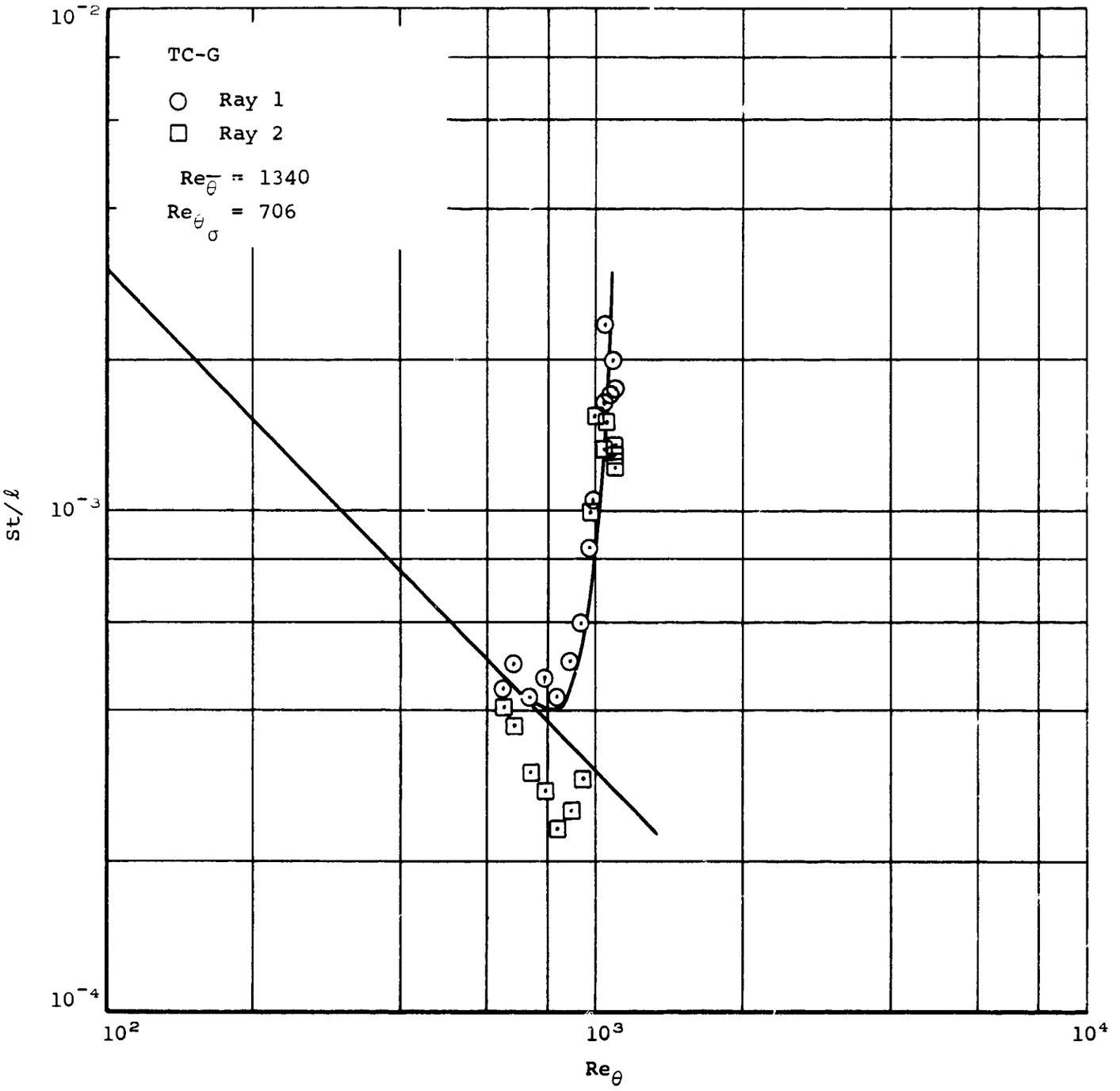

(d) S/R = 60°

Figure 17.- Continued.

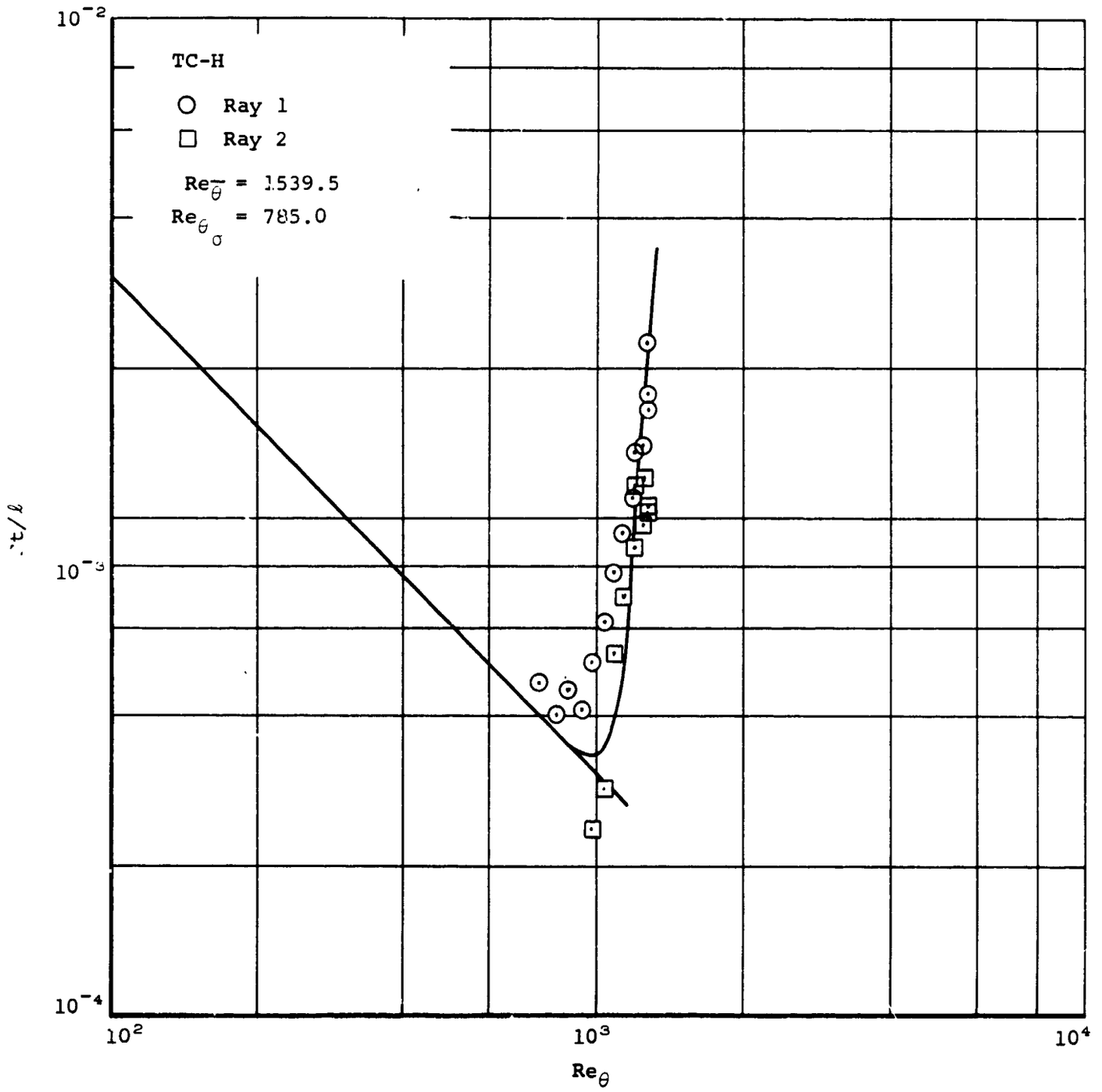

(e) S/R = 70°.

Figure 17.- Continued.

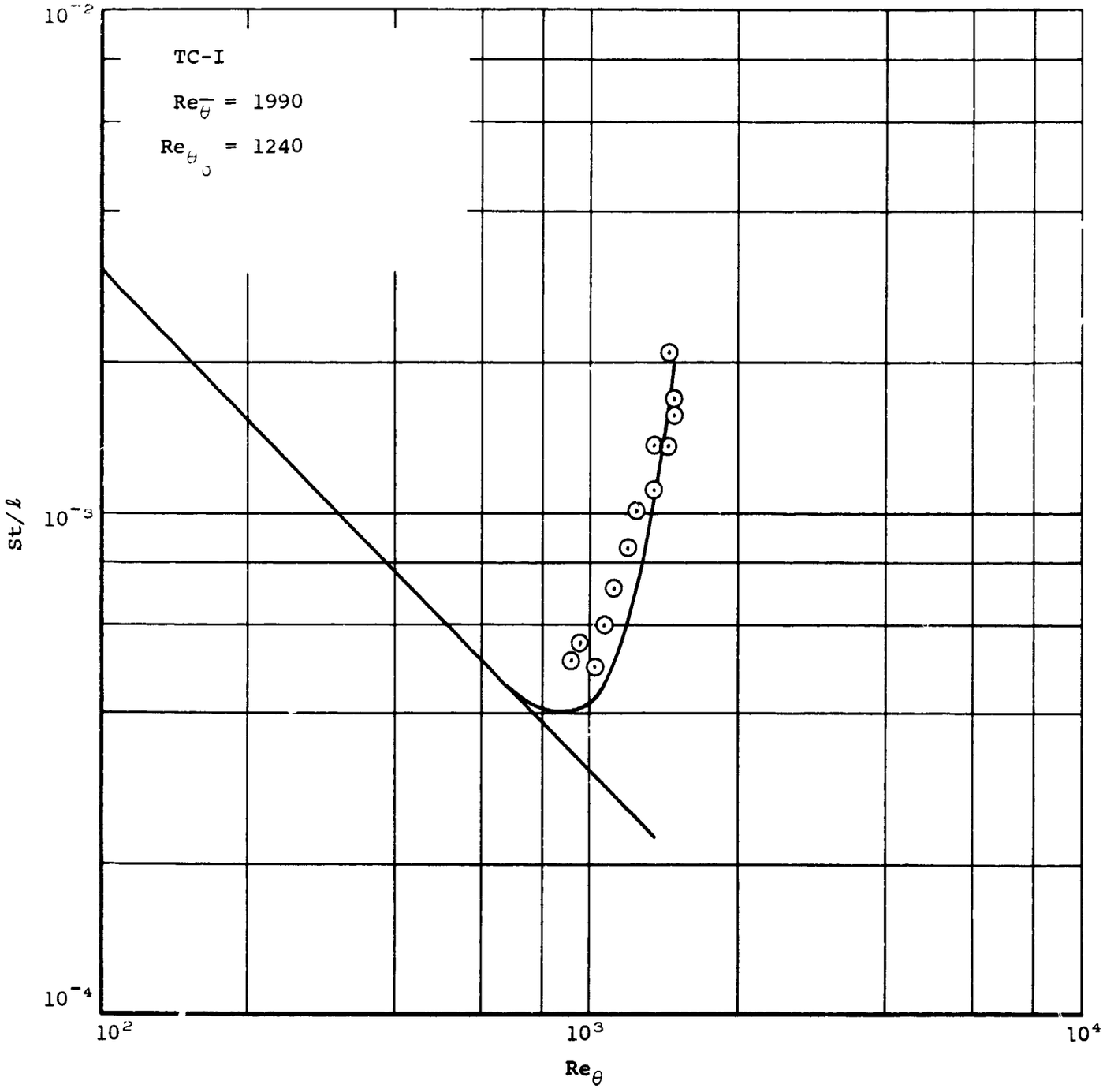

(f) S/R = 80°

Figure 17.- Concluded.

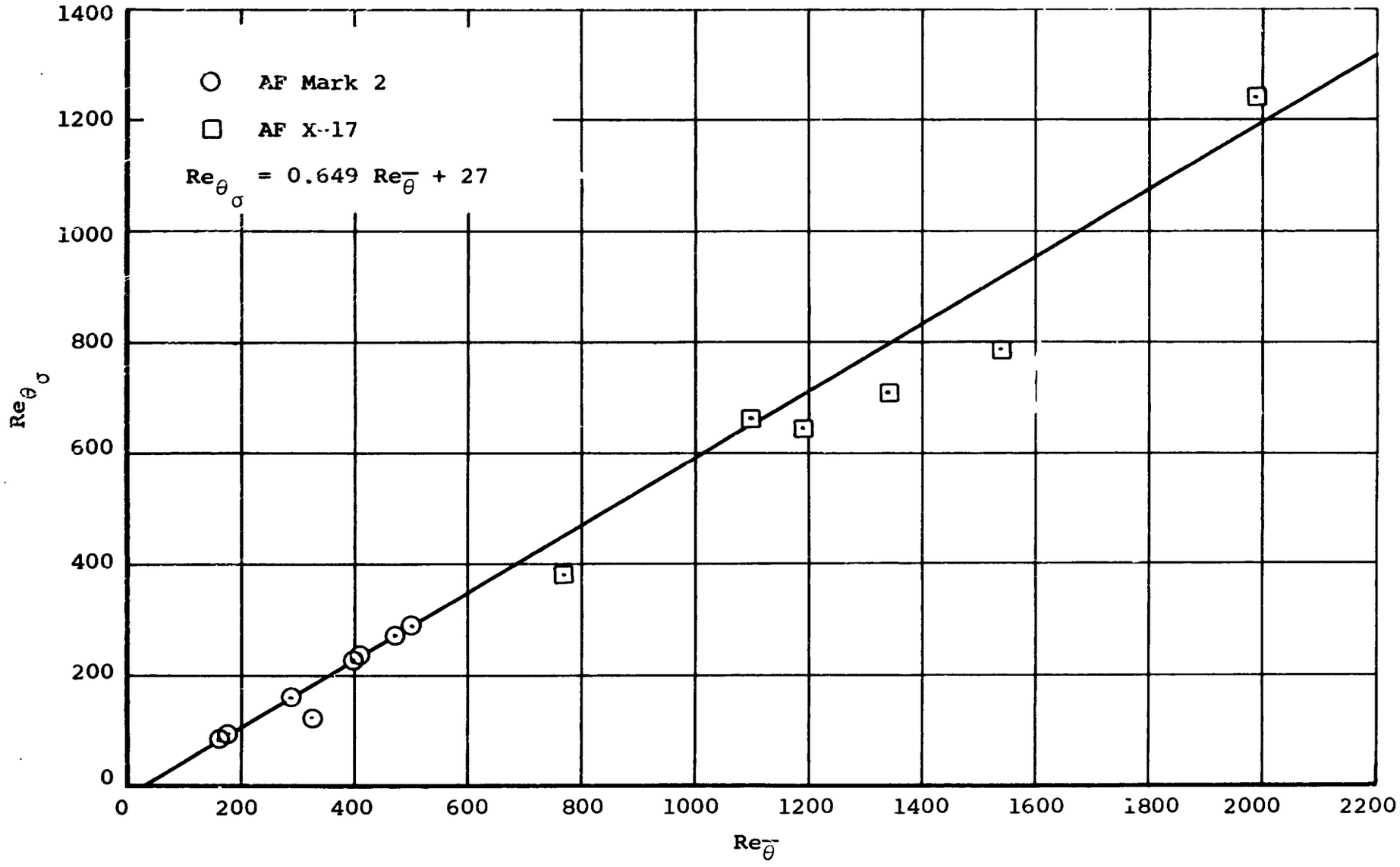

Figure 18.- Empirical relation for Re_{θ_σ} in terms of $Re_{\overline{\theta}}$.

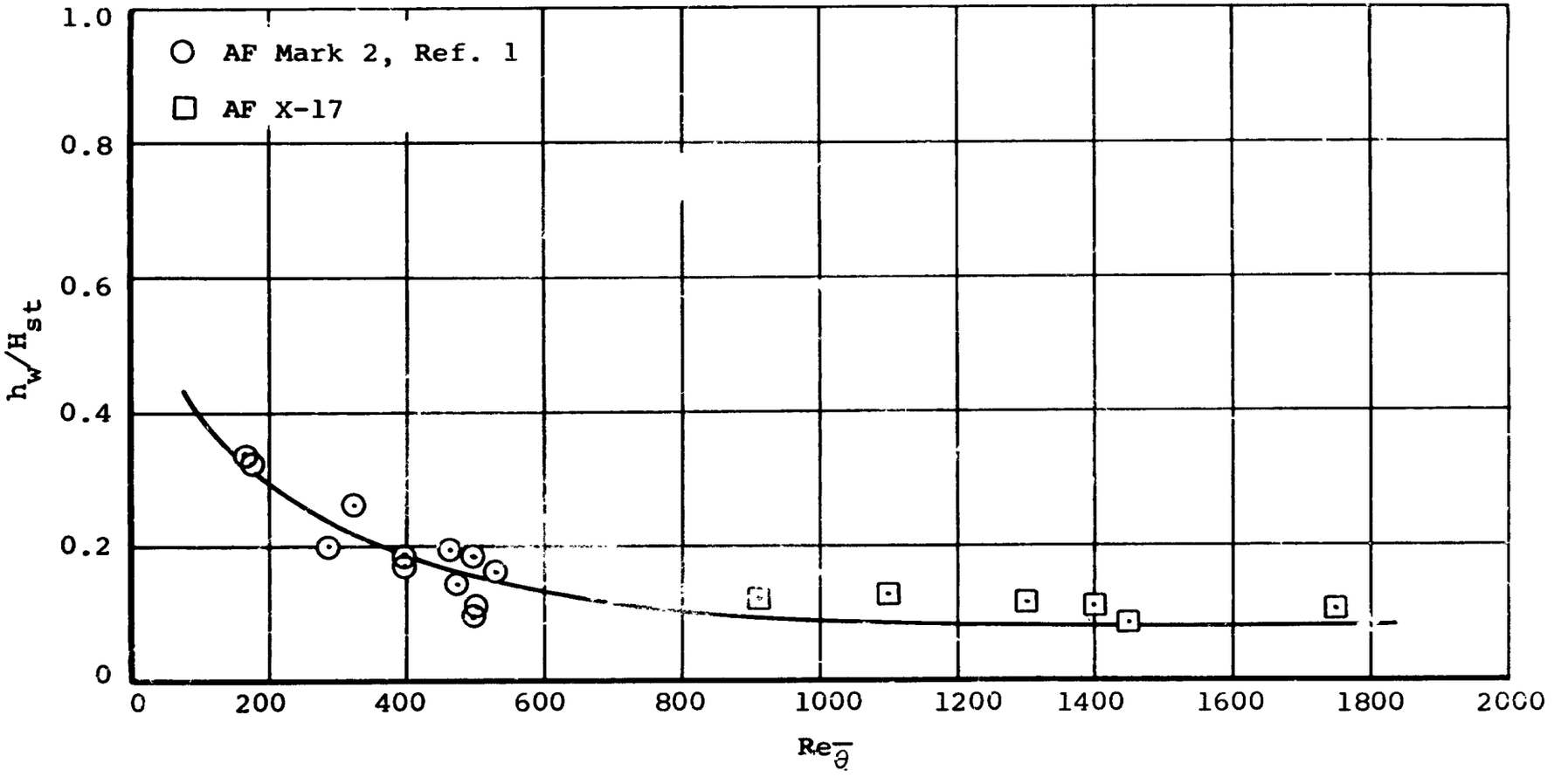

Figure 19.- Correlation of mean laminar momentum thickness Reynolds number for boundary-layer transition.

APPENDIX A

DATA SMOOTHING

A.1 INTRODUCTION

The method developed and applied here for the smoothing of raw digitized data can be described as an aid to hand fairing. This method differs from the more commonly used "walking polynomial" methods primarily in the choice of the number of data points to be considered at each step. The assumptions underlying the procedure described here are, as noted in Section 3.2:

(1) Errors in the data are random in nature, that is, there is no bias in the system.

(2) The actual temperature history is smooth and continuous in value and in first derivative.

(3) The error in any given thermocouple is bounded by a fixed percentage of the instrument range.

In developing the present method it is argued that one cannot distinguish a change in signal level between data points which differ by less than the magnitude of the scatter band appropriate to the instrument in question.

By inspection of a complete data trace one can assign a scatter band as a definite percentage of the instrument range. Assuming that this scatter band is independent of the reading level the accuracy of the data with respect to the true temperature can be no better than $\pm \eta R/T$, where η is the scatter band in percent, R the range of the instrument, and T the true temperature.

In applying this technique to flight-test data, one takes the initial data point, R_1, and considers all the succeeding points lying within the band $R_1 \pm \eta R$. The arithmetic average of these points is taken as being characteristic of the entire sample. This process is repeated sequentially until all the data points have been considered. The average points are then used in drawing a hand-faired curve representing the smoothed data. This curve is then differenced to obtain a table of first derivatives and a hand smoothing operation is again applied. This latter smoothing operation, in general, requires only small changes in the difference table to obtain the desired results, that is, the change in temperature differences required for smoothness is $\ll \eta R$. A new smooth-data curve is obtained

and compared with the original data. If no anomalies are noted this curve is used as input to the data-reduction program.

In order to check the relative accuracy of this method a fictitious temperature history was constructed. This temperature history of the form

$$T - T_o = 1.2\ \theta^2 - 0.016\ \theta^3$$

was used as a base about which "data" were scattered using a table or random numbers. An instrument range of 1500^o with a ± 8 percent scatter band was assumed, the sampling rate was taken as 1 point per second.

Three smoothing procedures were applied to these data. The first of these methods simply fit a least squares cubic to all the data, the second method used a least squares 7-point walking polynomial to generate average points which were fit by a least squares cubic, and the third method was that described here with the results fit by a least squares cubic. Figure A-1 shows the original analytic curve and the various curve fits to the data. This figure can be used only to indicate the relative accuracy of the various smoothing procedures since the results of each of these methods was required to have the same form as the original input.

It can be noted that the present method agrees, both in slope and level, with the original analytical form from time zero up to about time equals 38 seconds, or somewhat past peak heating. Subsequent to this time all three methods tend to underpredict the original curve. After this time the results become increasingly questionable. It can be seen that the method applied here is, in general, better than the other methods considered.

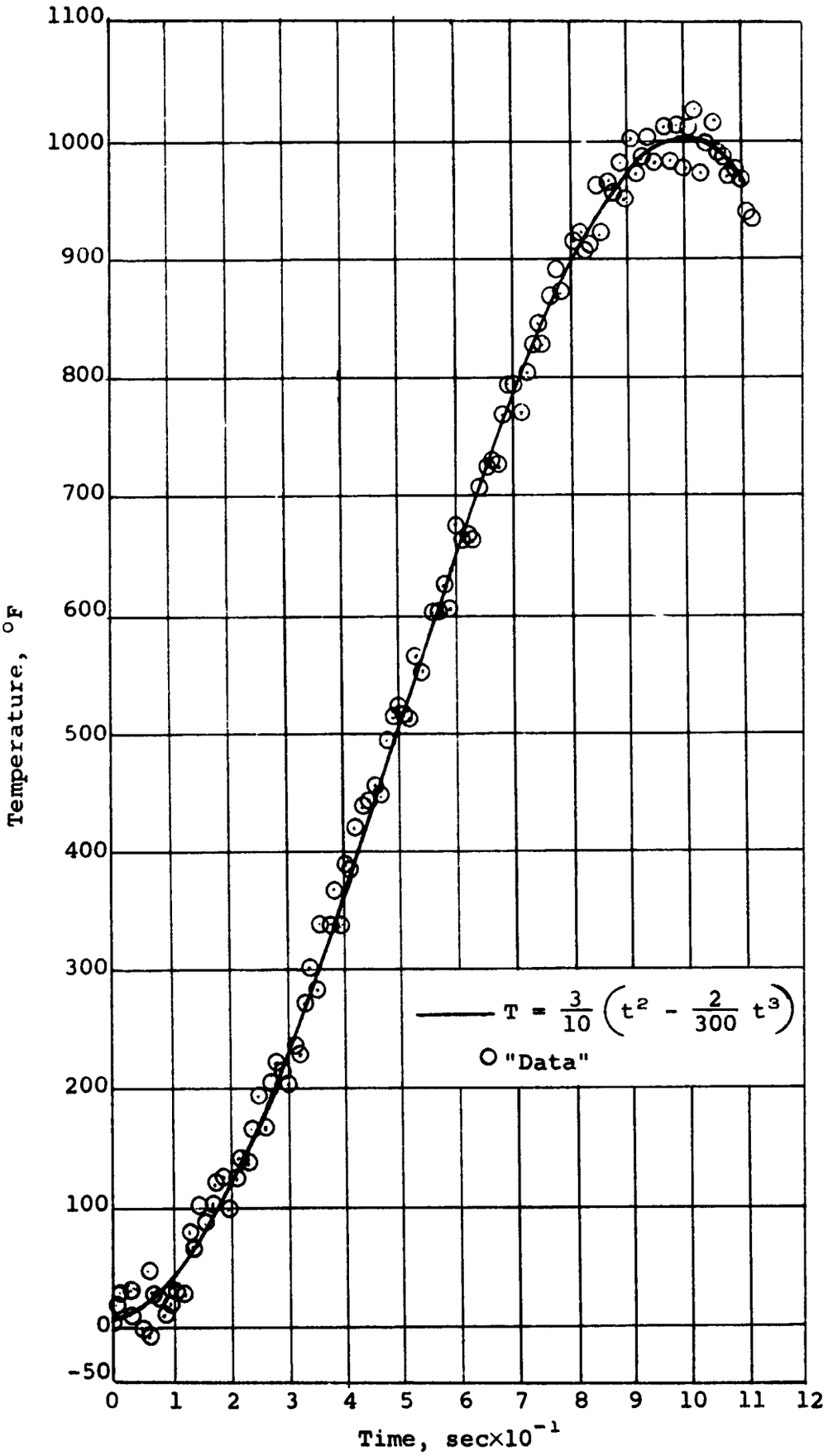

Figure A-1.- Comparison of results obtained with three smoothing methods (data sample rate of 1 per second, scatter band ± 120° F).

APPENDIX B

AXISYMMETRIC TRANSIENT-TEMPERATURE, VARIABLE THERMAL-PROPERTY CONDUCTION PROGRAM

B.1 INTRODUCTION

This appendix describes a numerical transient-temperature, variable thermal-property conduction program for two-dimensional or axisymmetric geometries and thermal boundary conditions. The numerical solution of the energy equation described here was programed for use on an IBM 7094 digital computer and was employed in all nose shield data reduction described in the body of this report. The energy equation that is solved is basically an explicit, finite difference formulation in which finite nodal volumes are considered and an energy balance is achieved at each node in the computational program. The flow of heat to or from a node by conduction during a step forward in time is calculated using distance-averaged resistances in which thermal conductivities are evaluated at the current temperatures of the node in question and the surrounding nodes that influence the node being considered. The thermal capacity of the nodal volume being considered is also evaluated at the current temperature during a forward step in time. Thus, the solution considers both the effects of time and space variations of the properties.

The program has two options: In Option One, temperatures within a structure are calculated from prescribed heating boundary conditions; in Option Two, the internal temperatures and heating boundary conditions are determined from prescribed temperature histories at points in the structure.

The procedures followed in contructing and using the program and certain limitations in the program are described in the following two sections. First, the required geometrical input is given, the internal computation of nodel volumes and conduction path lenghts described, and the thermal-property inputs indicated. Next the boundary condition forms utilized are given. Finally, the conduction equation solution is described.

B.2 CONDUCTION PROGRAM

B.2.1 Geometry and Internal Conduction Parameters

The conduction network is axisymmetric and is restricted to a quadrilateral nodal network. Elemental box corner r and z coordinates are

specified as input. Associated with nodal box is a nodal point, or node. Nodal r and z coordinates may or may not be specified. If they are not specified, the node is placed in the geometric center of the box. The nodal box corners and nodes are specified by unique m and n numbers. The m and n network does not have to be oriented in any particular fashion with respect to the r and z axes. The notation employed for the characterization of various nodal parameters is shown in Figure B.1. Geometrical parameters required for the conduction solution are computed from the input data.

The path lenghts between the nodes and the sides of the nodal box are computed as follows:

$$L_{m,n,A} = \left[\left(\frac{r_{c,m,n} + r_{c,m+1,n}}{2} - r_{N,m,n}\right)^2 + \left(\frac{z_{c,m,n} + z_{c,m+1,n}}{2} - z_{N,m,n}\right)^2\right]^{1/2} \quad \text{(B.1)}$$

$$L_{m,n,B} = \left[\left(\frac{r_{c,m+1,n} + r_{c,m+1,n+1}}{2} - r_{N,m,n}\right)^2 + \left(\frac{z_{c,m+1,n} + z_{c,m+1,n+1}}{2} - z_{N,m,n}\right)^2\right]^{1/2} \quad \text{(B.2)}$$

$$L_{m,n,C} = \left[\left(\frac{r_{c,m+1,n+1} + r_{c,m,n+1}}{2} - r_{N,m,n}\right)^2 + \left(\frac{z_{c,m+1,n+1} + z_{c,m,n+1}}{2} - z_{N,m,n}\right)^2\right]^{1/2} \quad \text{(B.3)}$$

$$L_{m,n,D} = \left[\left(\frac{r_{c,m,n+1} + r_{c,m,n}}{2} - r_{N,m,n}\right)^2 + \left(\frac{z_{c,m,n+1} + z_{c,m,n}}{2} - z_{N,m,n}\right)^2\right]^{1/2} \quad \text{(B.4)}$$

where the leading subscript N denotes thenodal coordinate, and the leading subscript c denotes the corner coordinate as indicated in Figure B.1.

where the leading subscript N denotes the nodal coordinate, and the leading subscript c denotes the corner coordinate as indicated in Figure B.1.

As shown in Figure B.1, the path lenghts between nodes are taken as the sum of the path lenghts between each node and the midpoint of the line separating the two nodes. <u>This must be kept in mind when the option to specify the location of a nodes is exercised.</u>

The areas on the sides of the nodal box are then computed.

$$A_{m,n,A} = \pi \left(r_{c,m,n} + r_{c,m+1,n}\right) \left[\left(r_{c,m+1,n} - r_{c,m,n}\right)^2 + \left(z_{c,m+1,n} - z_{c,m,n}\right)^2\right]^{1/2} \tag{B.5}$$

$$A_{m,n,B} = \pi \left(r_{c,m,n} + r_{c,m,n+1}\right) \left[\left(r_{c,m,n+1} - r_{c,m,n}\right)^2 + \left(z_{c,m,n+1} - z_{c,m,n}\right)^2\right]^{1/2} \tag{B.6}$$

The areas on the other sides of the nodal box are computed when the areas for the adjacentnodes are computed.

The volume of the elemental box is then computed.

$$\begin{aligned} V_{m,n} = \Bigg(\frac{\pi}{3} \Bigg\{ & z_{c,m,n} \left[r_{c,m,n} \left(r_{c,m,n+1} - r_{c,m+1,n}\right) + r^2_{c,m,n+1} - r^2_{c,m+1,n}\right] \\ & + z_{c,m+1,n} \left[r_{c,m+1,n} \left(r_{c,m,n} - r_{c,m+1,n+1}\right) + r^2_{c,m,n} - r^2_{c,m+1,n+1}\right] \\ & + z_{c,m+1,n+1} \left[r_{c,m+1,n+1} \left(r_{c,m+1,n} - r_{c,m,n+1}\right) + r^2_{c,m+1,n} - r^2_{c,m,n+1}\right] \\ & + z_{c,m,n+1} \left[r_{c,m,n+1} \left(r_{c,m+1,n+1} - r_{c,m,n}\right) + r^2_{c,m+1,n+1} - r^2_{c,m,n}\right] \Bigg\} \Bigg) \end{aligned} \tag{B.7}$$

The above equations for the path lengths, nodal box areas, and volumes are employed for determining thermal resistance between nodes, heated areas of nodes, and thermal capacities of nodes.

The thermal resistance between nodes and the thermal capacity of the nodes are calculated each time interval from the material properties of the node corresponding to its temperature at that time. The material properties (density ρ, specific heat c, conductivity k, and emissivity ε) are input as table look-up functions of temperature. Fifteen temperature entries are available for each of the none material property tables. Linear interpolation is employed for material property determination at temperatures intermediate to those tabulated. Constant thermal contact resistances may be specified between any two nodes. Nodal capacities and resistances are calculated as follows:

$$C_{m,n,\theta} = \rho_{m,n,\theta} c_{m,n,\theta} V_{m,n} \tag{B.8}$$

$$R_{m,n,A,\theta} = \frac{1}{A_{m,n+1,A}} \left(\frac{L_{m,n,C}}{k_{m,n,\theta}} + \frac{L_{m,n+1,A}}{k_{m,n+1,\theta}} + IR_{m,n,B} \right) \tag{B.9}$$

$$R_{m,n,B,\theta} = \frac{1}{A_{m+1,n,B}} \left(\frac{L_{m,n,B}}{k_{m,n,\theta}} + \frac{L_{m+1,n,D}}{k_{m+1,n,\theta}} + IR_{m,n,A} \right) \tag{B.10}$$

The resistances on the other two sides of the nodal box are calculated when the quantities for the adjacent nodes are calculated.

B.2.2 Boundary Conditions

The heating boundary conditions are of two types: Option One determines nodal temperatures from prescribed convection coefficients and recovery enthalpies, and Option Two determines internal temperatures and net heating rates from prescribed temperature histories.

For Option One, any of the nodes may be heated according to the relation

$$Q_{net} - Q_{conv} - Q_{rad} \tag{B.11}$$

where

$$Q = qA_Q$$

and A_Q is the area of the side of the node which is heated, that is, side 1, 2, 3, or 4 as shown in Figure B.1. Only one of the four sides of a nodel box may be heated. Dividing Equation (B.11) by A_Q yields

$$q_{net} - q_{conv} - q_{rad}$$

and expanding,

$$q_{net} = Kh \left(I_r - I_W\right) - \sigma\epsilon \left(T_W^4 - T_S^4\right) \qquad \text{(B.12)}$$

The input consists of specifying the radiation sink temperature T_S, and, for each heated node, the constant K, a table number which lists the convection heat-transfer coefficient h, and recovery enthalpy I_r as functions of time θ, a table number which gives the wall enthalpy I_W as a function of wall temperature T_W, and a material number from which the emissivity ϵ is determined as a function of the nodal temperature. The constant K is useful when the convection coefficient varies by a constant between heated nodes. The program allows up to 20 tables of h and I_r versus θ, each of which may have as many as 50 entries. There may be either 1 or 2 different variations of wall enthalpy with temperature, each table having as many as 15 entries. Linear interpolation is employed in all tables.

The input data required for Option Two is identical to that for Option One with the exception that the convection coefficient history (h versus θ) is replaced with a temperature history (T versus θ) for each heated node. Since there is a maximum of 20 such tables, Option Two is restricted to 20 heated nodes.

B.2.3 Conduction Solution

The conduction solution is an explicit finite difference formulation of the type often employed for transient heat-conduction analysis. The temperature of node m,n at time θ' ($T_{m,n,\theta'}$) is obtained by application of the finite difference energy balance and rate equations to the finite nodel volume. Solving for $T_{m,n,\theta''}$, one obtains

$$T_{m,n,\theta'} = \left[q_{net,\theta} A_Q + \frac{T_{m+1,n,\theta}}{R_{m,n,B,\theta}} + \frac{T_{m,n+1,\theta}}{R_{m,n,A,\theta}} + \frac{T_{m-1,n,\theta}}{R_{m-1,n,B,\theta}} + \frac{T_{m,n-1,\theta}}{R_{m,n-1,A,\theta}} - T_{m,n,\theta}\left(\frac{1}{R_{m,n,B,\theta}} + \frac{1}{R_{m,n,A,\theta}} + \frac{1}{R_{m-1,n,B,\theta}} + \frac{1}{R_{m,n-1,A,\theta}} \right) \right] \frac{\Delta\theta}{C_{m,n,\theta}} + T_{m,n,\theta} \quad (B.13)$$

B.2.4 Stability

There are two options available for specification of the time increment employed in the conduction solution. A constant time step can be specified for use throughout the computation. This eliminates internal calculation of the time increment required for stable computation in cases where this can be determined accurately by independent means as, for example, when constant thermal properties are employed. If this option is not employed, an internal computation is made to determine the allowable time step for stable computation for all nodes in the net or for the particular set of nodes specified in input. In other words, it may be possible to identify the nodal volumes that limit the time increment for stable computation - in particular those with small capacity and resistance - during the construction of the net and thus avoid the time increment calculation for allnodes in the net. When this is not possible, the stability calculation is made for each node and the smallest resulting allowable time step used in proceeding through the next step in the conduction solution.

The stability criterion used in the program is based simply on the requirement that the influence of the present temperature of a node on the future temperature of that node must be positive. This then gives the two-dimensional analog of the familiar Fourier modulus limit for one-dimensional conduction. For an internal node, that is, one that is not heated by convection or radiation, the expression for future temperature can be written, from Equation (B.13), as

$$T_{m,n,\theta'} = \left[1 - \left(\frac{1}{R_{m,n,B,\theta}} + \frac{1}{R_{m,n,A,\theta}} + \frac{1}{R_{m-1,n,B,\theta}} + \frac{1}{R_{m,n-1,A,\theta}}\right)\frac{\Delta\theta}{C_{m,n,\theta}}\right] T_{m,n,\theta} + \left(\frac{T_{m+1,n,\theta}}{R_{m,n,B,\theta}} + \frac{T_{m,n+1,\theta}}{R_{m,n,A,\theta}} + \frac{T_{m-1,n,\theta}}{R_{m-1,n,B,\theta}} + \frac{T_{m,n-1,\theta}}{R_{m,n-1,A,\theta}}\right)\frac{\Delta\theta}{C_{m,n,\theta}} \quad \text{(B.14)}$$

The stability requirement for internal nodes is, thus,

$$\Delta\theta \leq \frac{C_{m,n,\theta}}{\frac{1}{R_{m,n,A,\theta}} + \frac{1}{R_{m,n,B,\theta}} + \frac{1}{R_{m,n-1,A,\theta}} + \frac{1}{R_{m-1,n,B,\theta}}} \quad \text{(B.15)}$$

Upon reduction to an expression in terms of path lengths and constant thermal properties this reproduces the familiar requirement of a Fourier modulus less than one-half for stable internal computation. For heated nodes, the boundary stability requirement is obtained from the coefficient of $T_{n,n,\theta}$ given by Equation (B.13) and, in essence, requires that the term

$$A_Q\left(Kh\,\frac{I_W}{T_{m,n,\theta}} + \sigma\epsilon\,T^3_{m,n,\theta}\right)$$

be added to the denominator of Equation (B.15). Since, in general, $I_W/T_{m,n,\theta} \leq 0.5$ for most gases and nodal locations near a heated surface, this quantity is replaced by 0.5 in the determination of permissible time steps from surface heating conditions. It is recognized that this surface criterion will not, in general, insure that computation and round-off errors introduced at the surface will not grow in time, particularly if the term representing radiation from the surface is large. Consequently, an arbitrary multiplier, η, less than unity can be specified as input to reduce the permissible time step from that given by the stability criterion alone and the final general expression for the allowable computational time step is written as

$$\Delta\theta = \eta\left[\frac{C_{m,n,\theta}}{\frac{1}{R_{m,n,A,\theta}} + \frac{1}{R_{m,n,B,\theta}} + \frac{1}{R_{m-1,n,B,\theta}} + \frac{1}{R_{m,n-1,A,\theta}} + A_Q\left(0.5Kh + \sigma\epsilon T^3_{m,n,\theta}\right)}\right] \quad \text{(B.16)}$$

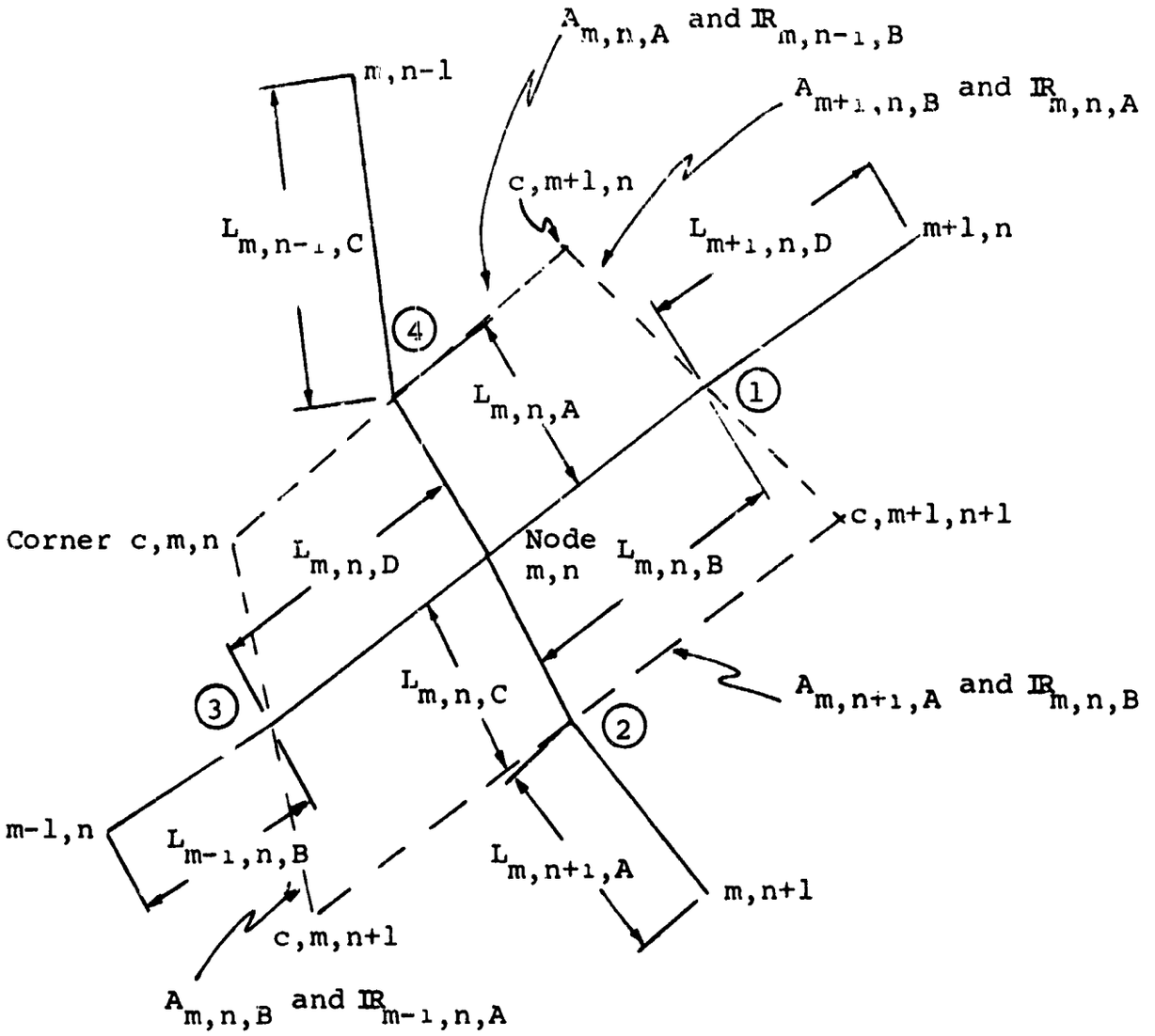

Notes: 1. R denotes thermal contact resistance locations.

2. Numbers in circles denote sides to be heated.

Figure B-1.- General nodal orientation and description of nodal parameters.

APPENDIX C

THREE-DIMENSIONAL CONDUCTION PROGRAM

The principle difference between the X-17 R-2 and R-9 configurations was the addition to the R-9 of a nominal 30 μ-in. roughness patch installed over the secondary thermocouple run. The addition of this roughness patch was sufficient to cause early boundary-layer transition on that side of the body and resulted in a strongly asymmetric circumferential distribution of heat transfer. Due to the relatively thick highly conductive wall, it became necessary to account for heat conduction in the circumferential direction as well as that normal to, and along the body surface. It was for this reason that the present program was written.

The diffusion equation, in general curvilinear coordinates, is written

$$\rho C_p \frac{\partial T}{\partial \theta} = \frac{1}{h_1 h_2 h_3} \left(\frac{\partial}{\partial x} \frac{h_2 h_3}{h_1} k \frac{\partial T}{\partial x} + \frac{\partial}{\partial y} \frac{h_2 h_3}{h_2} k \frac{\partial T}{\partial y} + \frac{\partial}{\partial \phi} \frac{h_1 h_2}{h_3} k \frac{\partial T}{\partial \phi} \right)$$

where the coordinate metrics h_1, h_2, and h_3 are defined by the relation

$$ds^2 = h_1^2 \, dx^2 + h_2^2 \, dy^2 + h_3^2 \, d\phi^2$$

In the natural coordinate system, see sketch, this becomes

$$ds^2 = \left(1 - \frac{d\alpha}{dx} y\right)^2 dx^2 + dy^2 + r^2 \, d\phi^2$$

from which

$$h_1 = 1 - \frac{d\alpha}{dx} y$$

$$h_2 = 1$$

and

$$h_3 = r$$

where x, y, and ϕ are a locally orthogonal right handed coordinate system.

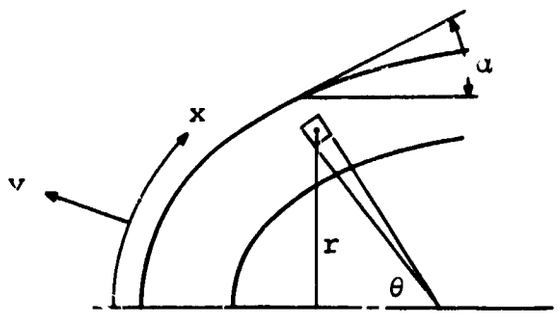

Assuming constant thermal properties and letting $\beta = d\alpha/dx$, the diffusion equation becomes

$$\rho C_p \frac{\partial T}{\partial \theta} = r(1 - \beta y)\left\{\frac{\partial k}{\partial x}\left(\frac{r}{1 - \beta y}\frac{\partial T}{\partial x}\right) + \frac{\partial k}{\partial y}\left[r(1 - \beta y)\frac{\partial T}{\partial y}\right] + \frac{\partial k}{\partial \phi}\left[\left(\frac{1 - \beta y}{r}\right)\frac{\partial T}{\partial \phi}\right]\right\}$$

with the six boundary conditions

$$\text{at} \quad x = 0 \qquad \frac{\partial T}{\partial x} = \frac{\partial T(y,\phi,\theta)}{\partial x}$$

$$x = 0 \qquad \frac{\partial T}{\partial x} = 0$$

This later condition while not generally true is applicable to R-2 and R-9 data (see Refs. 3 and 4)

$$\text{at} \quad y = 0 \qquad T = T(x,\phi,\theta)$$

$$y = -0 \qquad \frac{\partial T}{\partial y} = 0$$

$$\text{at} \quad \phi = 0, 2\pi \qquad T(x,y,\theta)\Big|_{\phi=0} = T(x,y,\theta)\Big|_{\phi=2\pi}$$

$$\frac{\partial T(x,y,\theta)}{\partial \phi}\Big|_{\phi=2\pi} = \frac{\partial T(x,y,\theta)}{\partial \phi}\Big|_{\phi=0}$$

and the initial condition

$$T = T(x,y,\phi,0)$$

Since the configuration under consideration is a hemisphere cylinder, the additional simplification

$$0 \leq x \leq \frac{\pi R}{2} \qquad \beta = \frac{1}{R}$$

$$x > \frac{\pi R}{2} \qquad \beta = 0$$

was incorporated.

These equations were cast into a modified central difference formulation, and a so-called "marching" solution carried out.

The R-9 data reduction was carried out with a 400-node network, 4 rays of 10 nodes each located at 90° increments circumferentially with 10 nodes in depth for each surface node. Temperature histories for each surface node were prescribed from thermocouple data and an initial constant temperature body was assumed.

Output from this program yields the temperatures of each of the 400 nodal points as a function of time, and external heating rates to each of the 40 surface nodes. The external heating rate is computed from the relation

$$q_i = \rho C_p V_i \left.\frac{\partial T}{\partial \theta}\right|_i - \sum_1^5 k_j A_j \frac{\partial T}{\partial x_j}$$